UC Berkeley
UC Berkeley Electronic Theses and Dissertations

Title

Engineering the electronic structure of atomically-precise graphene nanoribbons

Permalink

https://escholarship.org/uc/item/10q0v3b5

Author

Nguyen, Giang Duc

Publication Date

2016

Peer reviewed|Thesis/dissertation

Engineering the electronic structure of atomically-precise graphene nanoribbons

by

Giang Duc Nguyen

A dissertation submitted in partial satisfaction of the

requirements for the degree of

Doctor of Philosophy

in

Physics

in the

GRADUATE DIVISION

of the

UNIVERSITY OF CALIFORNIA, BERKELEY

Committee in charge:

Professor Michael F. Crommie, Chair
Professor Feng Wang
Professor Junqiao Wu

Summer 2016

Engineering the electronic structure of atomically-precise graphene nanoribbons

Abstract

Engineering the electronic structure of atomically-precise graphene nanoribbons

by

Giang Duc Nguyen

Doctor of Philosophy in Physics

University of California, Berkeley

Professor Michael F. Crommie, Chair

Graphene nanoribbons (GNRs) have recently attracted great interest because of their novel electronic and magnetic properties, as well as their significant potential for device applications. Although several top-down techniques exist for fabricating GNRs, only bottom-up synthesis of GNRs from molecular precursors yields nanoribbons with atomic-scale structural control. Furthermore, precise incorporation of dopant species into GNRs, which is possible with bottom-up synthesis, is a potentially powerful way to control the electronic structure of GNRs. However, it is not well understood how these dopants affect the electronic structure of GNRs. Are these effects dependent on the dopant site? Can the band gap be tuned by doping? This dissertation helps to answer these questions through studying the electronic structure of bottom-up grown GNRs with controlled atomic dopants. The effects of edge and interior doping with different atomic species such as sulfur, boron and ketone were investigated and showed significant site dependence. Topographic and local electronic structure characterization was performed via scanning tunneling microscopy & spectroscopy (STM & STS) and compared to first-principle calculations. The chemical structure of GNRs and GNR heterojunctions was characterized by CO-tip-functionalized non-contact atomic force microscopy (nc-AFM) as well as by a newly developed technique of bond-resolved STM (BRSTM).

In an effort to develop a new method for directly synthesizing GNRs on an insulating substrate, we also studied light-induced photo-isomerization of azobenzene molecules adsorbed on an insulating surface of CVD-grown monolayer boron nitride (BN) on Cu(111). This study provides important insights into molecular behavior on an insulating surface, how to couple light to an STM system, and how to utilize local field enhancement effects due to surface plasmon resonance.

Contents

List of Figures

List of Tables

List of Abbreviations

CMOS	Complementary Metal–Oxide–Semiconductors
SAM	Self-Assembled Monolayer
GNR	Graphene Nanoribbon
AFM	Atomic Force Microscope or Atomic Force Microscopy
FM-AFM	Frequency Modulated Atomic Force Microscopy
AGNR	Armchair Graphene Nanoribbon
DFT	Density Functional Theory
dI/dV	Differential Conductance
DOS	Electronic Density of States
E_F	Fermi energy
LDOS	Local Density of States
nc-AFM	Non-Contact Atomic Force Microscope or Non-Contact Atomic Force Microscopy
QCM	Quartz Crystal Microbalance
STM	Scanning Tunneling Microscopy or Scanning Tunneling Microscope
STS	Scanning Tunneling Spectroscopy
UHV	Ultrahigh Vacuum
IRSTM	Infrared Scanning Tunneling microscopy
BRSTM	Bond-Resolved Scanning Tunneling Microscopy
UV	Ultraviolet
BN	Boron Nitride
VB	Valence Band
CB	Conduction Band
FIB	Focused Ion Beam

Acknowledgement

First of all, I would like to thank my advisor Prof. Mike Crommie for the patience, guidance, and endless encouragement he has provided me throughout all of my graduate years. In his group, I have grown as an experimental researcher through his great balance of guidance and freedom to follow my ideas and perform my work. I remember starting in his group with no experimental skill: for example, at the beginning I had no idea what a digital multimeter (DMM) looked like. Mike has taught me so many things, from how to create a simple picture for understanding physical phenomena and presenting data to how to write an academic paper. Without his support, none of my research work would have been possible, including this dissertation. I also cherish the time I worked in his lab, the group meetings and also parties at his home. He definitely made my PhD life at Berkeley extremely interesting, valuable, and enjoyable.

I also would like to express my gratitude to Prof. Feng Wang, who always generated many great ideas and provided me incredible advice with his broad knowledge and remarkable understanding. Thanks to Prof. Felix Fischer, who has valuable chemical insights and provided us with excellent molecules. Thanks also to Prof. Steven Louie for the wonderful collaboration with my experiments. Calculations from Louie group provide us a better understanding of our experimental data. I also would like to thank Prof. Junqiao Wu for serving on my qualifying examination and dissertation committee.

Ivan Pechenezskiy is the first and longest graduate student I worked with in the Crommie group. He is a great experimentalist and an outstanding mentor who taught me about scanning tunneling microscopy (STM), experiments and even basic lab stuff. For several years, we shared all our moments of success well as failure. Together with Xiaoping Hong, we successfully performed our IRSTM experiment. Simultaneously, we spent a lot of time trying numerous experimental ideas and maintaining the STM, and those memorable experiences keep reminding me that lab work has never been a "one person" job. I still remember the time that we had to put the heavily repaired ion pump back into the STM chamber. Even with very careful preparation and a designed setup, it took us a week with three trials in order to mount it without a leak. It made me learn that even the most "reasonable" idea is not always the right one and that the most important thing is to think outside of the box and to continue try new ideas.

I am also in debt to a number of people in the lab who I have been lucky to work with. I am thankful to Dan Rizzo, a terrific co-worker who has spent a great amount of time to help me proof-read my terrible writing, Arash Omarani and Hsin-Zon Tsai, who taught me to use the "Beast" for getting beautiful GNR data. I enjoyed very much discussing interesting experimental ideas with Hsin-Zon, and extremely admire his leadership skills in managing undergrads. I would like to thank Chris Bronner and Trinity Joshi for their big help in the sulfur and boron doped GNR projects, Chen Chen and Zahra Pedramrazi for their strong support and discussion when I started working on

GNRs, Griffin Rodgers who worked with me through the last winter break for achieving amazing data on the ketone GNRs and discovering the bond-resolved STM (BRSTM) technique.

This dissertation could not be completed without great, supportive collaborators. Thanks to Ryan Cloke, Tomas Marangoni and Francesca Toma from the Fischer group for providing fantastic GNR molecules, Ting Cao and Meng Wu from Louie group for performing excellent first-principle calculations for understanding our experimental GNR data. Xiaoping Hong from Feng group, a wonderful collaborator who taught me all about optics and alignment tricks, Yuki Sakai, who performed a difficult calculation for our IRSTM experiment and is now doing simulations for our BRSTM imaging, and Marco Favaro, who helped me to interpret the Auger spectroscopic data.

There are also many more wonderful current and former members of the Crommie group to thank: Juwon Lee, Dillon Wong, Aaron Bradley, Yen-Chia Chen, Jairo Velasco, Sabastian Wickenburg, Ryan Yamachika, Danny Haberer, Kacey Meaker, Yi Chen, Salman Kahn, Brandon Giles, Hannes Bockmann, Miguel Ugeda, Dimas de Oteyza, Jiong Lu,Won-Woo Choi, Andrew Aikawa, Patrick Forrester, Yun Zhou, Jakob Jørgensen, Jongweon Cho, Xiaowei Zhang, Yang Wang, Victor Brar, Chenggang Tao, Han Sae Jung, Chad Germany, Nick Kau.

I would like to mention the excellent support from the amazing administrative staffs in the physics department. Thanks to Anne Takizawa for constantly helping me with countless problems throughout my graduate years. You are the best support staffer I have ever met. Thanks to Lisa Partida, who was always ready to help with any administrative problems. I also would like to thank Donna Sakima, Kathy Lee and Elaine Quiter for helping me along the way.

I also would like to thank all my friends for their support during my years at Berkeley. Thanks to my neighbors Chris Proud, Kieu Proud and their daughter Kali Proud, as well as Uncle Bill and Auntie Bev, who spent so much time, love, and care for me and my family here and definitely made our time at Berkeley such a pleasant and memorable experience.

I would especially like to thank my family. Thanks to my wife, Phuong, for going through all the ups and downs in my research with me, throughout all these years. Thanks to my son, An Nguyen (Sếu) for cheering me up in thousands of ways with his uncountable cherishable moments. Thanks to my mother and father, Cuu Nguyen and Tinh Tran, for their endless love and trust throughout these years. Thanks to my brother and sisters, Long Nguyen, Ha Nguyen, Hang Nguyen, and Huong Nguyen for their strong support for my studying abroad. I also want to thank my wife's parents, Truc Nguyen and Phuong Man, and all the members of my extended family for their support and their trust in me, Ngoc Le, Cong Nguyen, Huong Duong, Thong Tran, and Lan Nguyen, and thanks

Chapter 1 : Introduction

1.1 Bottom up graphene nanoribbons

The explosive growth of digital information processing systems over the past 40 years has been driven by rapid scaling of complementary metal–oxide–semiconductors (CMOS) [1–3]. The size of the transistor has shrunk to the nanometer scale; as of 2015 a transistor can be as small as 14 nm [4,5]. However, the top-down fabrication techniques used to create electronic devices are not scalable to the single nanometer level [6–8]. At this length scale the electronic properties of materials are determined by their molecular structure. Harnessing the exotic behavior that emerges at this scale requires extreme control over chemical structure as well as reliable integration between nanoscale and macroscopic device elements. Consequently, many new approaches for realizing transistors at the nanometer scale are currently being explored [9]. Some of the new material candidates include small molecules [10,11], polymeric systems [12], self-assembled monolayers (SAMs) [13,14], and carbon nanotubes (CNTs) [15]. So far, none of these have been identified as a viable broad platform for future nanotechnology due to problems such as non-reproducibility of electronic properties, poor electrical contacts, and lack of nanoscale structural control. Recently, however, an exciting new material candidate has emerged in the form of bottom-up graphene nanoribbons (GNRs) that could potentially overcome these problems [16–26].
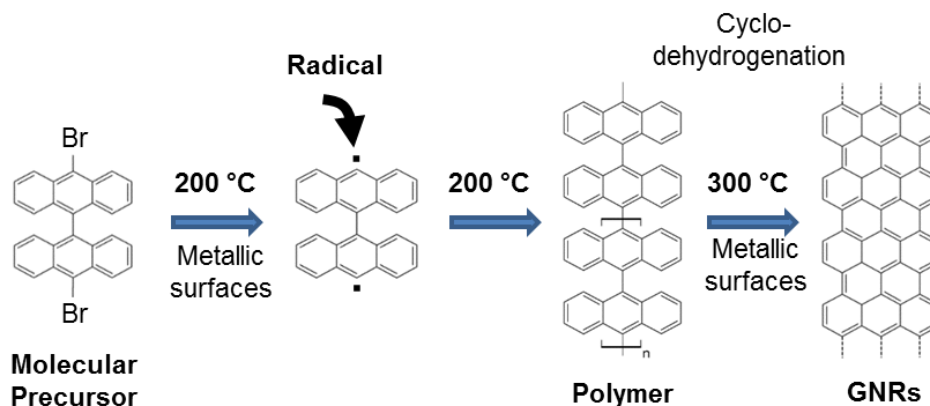
Figure 1.1: Schematic of bottom-up fabrication of N=7 armchair GNRs on metallic surface.

Discovered in 2010 [16], bottom-up GNRs share many of the extraordinary properties of graphene [27,28] and provide a flexible new way of building complex functional nanostructures from molecular precursors on surfaces (Figure 1.1). Perhaps most importantly, bottom-up GNRs provide a well-defined strategy for rationally tuning

electronic properties over a wide range while maintaining structural fidelity at the nanometer scale [16,25]. They exhibit extraordinary mobility [29], excellent optical properties [30], high strength [31], and novel magnetic properties [32], while allowing the possibility of band gap tunability [17,33–36], atomically-precise doping [19,36–41], and chemical flexibility [42]. Bottom-up GNRs are structurally and electronically homogeneous, they do not have the challenge of unwanted metallicity inherent to carbon nanotubes, and they offer unprecedented opportunities to synthesize complex heterostructures for new device applications from the bottom up [19,20]. Simulations of bottom-up GNR devices suggest that, if fabricated properly, they should outperform current CMOS technology and enable Moore's law scaling to continue well into the future [43]. Thus, bottom-up GNRs have potential to form the basis of a high-performing future nanotechnology with unmatched promise.

1.2 Doping a graphene nanoribbon
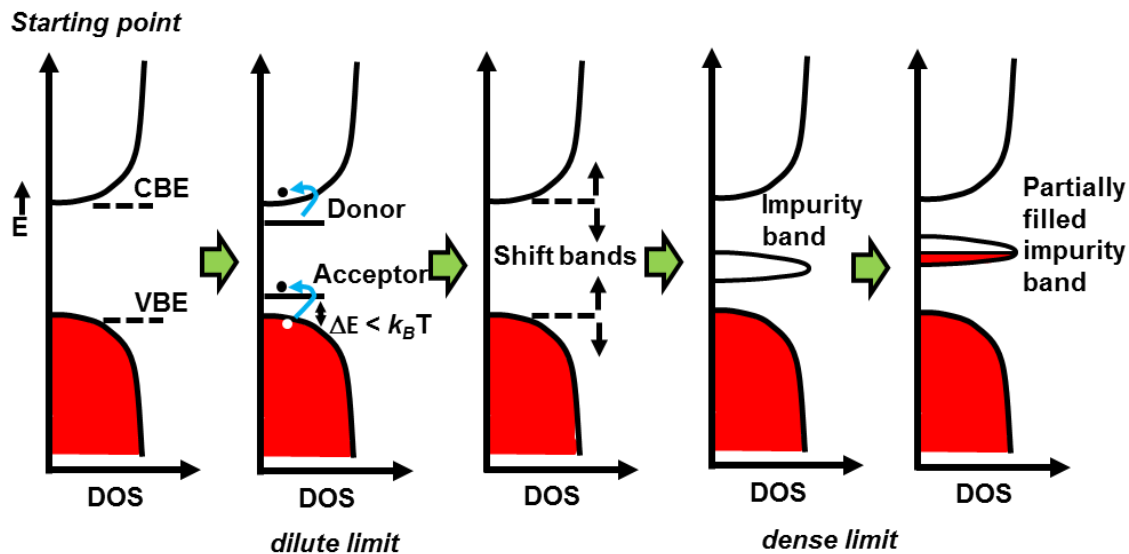
Figure 1.2: Controlling GNR electronic structure by doping.

The use of dopant atoms is a critical part of traditional semiconductor technology [44]. We believe that dopant-based functionalization will play an even more important role in future nanoscale technologies. Figure 1.2 shows the proposed ideas to control the electronic structure of GNRs using doping. In the dilute limit, the doping should induce donor and acceptor states, similar to the traditional semiconductor picture [45]. This kind of doping should help to tune the carrier density in the GNRs [45]. Atomically-precise integration of dopants at higher concentrations (dense limit) into GNRs should allow even greater changes in their electronic structure [19,36–38]. For example, in this dense limit doping should shift and modify the bands, consequently changing the effective mass

and carrier mobility [37]. In addition, site-specific dopants should introduce new states into the GNR band gap and lead to entirely new GNR electronic structures [36]. Doped GNRs are also a critical component for creating atomically-precise GNR heterojunctions [19,20]. Furthermore, dopant functionalization should provide new device opportunities that don't exist for traditional materials. For example, proper placement of a single dopant atom could potentially give bottom-up GNRs completely new switching capabilities, optical capabilities, and magnetic functionality.

1.3 Summary of thesis contents

Chapter 1 provides an introduction to GNRs, including motivation and instrumental overview.

Chapter 2 describes the bottom-up fabrication of sulfur edge-doped N=13 armchair GNRs (S-13AGNRs), the characterization of their topographical structure with STM and Auger spectroscopy, and the characterization of their electronic structure using STS and comparisons to DFT calculation.

Chapter 3 reports the successful fabrication of boron-doped N=7 armchair GNRs (B-7AGNRs) on both Au(111) and Ag(111) surfaces where substitutional boron atoms were incorporated into the central backbone of the GNRs. In this configuration, the boron's empty p-orbital is in conjugation with the extended π-system of the GNR and induces a new empty state in the band gap. The effects of the substrates on electronic structure of these boron doped ribbons are studied. Topographic and local electronic structure characterization was performed via STM and CO-tip-functionalized nc-AFM, and is compared to DFT simulations.

Chapter 4 focuses on the bottom-up synthesis of ketone edge-doped chevron GNRs. This doping at the edge is able to reduce the band gap of the ribbon. BRSTM is used to characterize the chemical structure of the GNRs. The electronic structure of the ketone doped GNRs is investigated using STS and compared with DFT simulation.

Chapter 5 addresses the successful fabrication of ketone-pristine GNR heterojunctions. BRSTM is used to characterize the chemical structure of the heterojunctions and is confirmed by theoretical simulations. Topographic and local electronic structure characterization was performed via STM/STS and compared to DFT simulations.

Chapter 6 describes the study of photoswitching of azobenzene on an insulating surface of BN on Cu(111). Upon UV illumination, the molecules undergo a photoswitching process that we believe is related to *trans-cis* photoisomerization. We discuss how to prepare a BN/Cu(111) substrate decorated with Au islands to induce local surface plasmon resonance when illuminated by a UV laser. This study is also useful for understanding the effect of light on molecules adsorbed to a surface. Furthermore, it

opens up the idea of using light to induce surface polymerization in order to form GNRs on an insulating surface.

1.4 Scanning tunneling microscopy

Invented in 1982 by Binnig and Rohrer, the scanning tunneling microscope (STM) is a very powerful instrument for studying molecular structures at the nanoscale [46–48]. In a STM, an atomically sharp tip is placed within several Ångströms of a conducting surface (Figure 1.3). When we apply a bias between the tip and the sample, electrons can flow between the tip and the sample due to the quantum mechanical process of tunneling. The tunneling current exponentially depends on the tip-sample distance, which yields the very high spatial resolution of this microscopy. A theoretical treatment of the STM is given Tersoff & Hamman [49] using Bardeen's formalism for tunneling current [50]. An extensive STM discussion can be found in Dr. Ryan Yamchika's thesis [51].
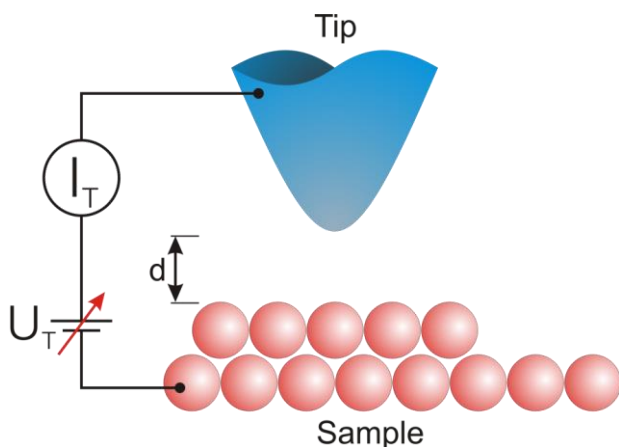
Figure 1.3: Schematics of scanning tunneling microscopy.

1.4.1 STM topography

STM topography is typically measured in a constant current feedback mode. We apply a constant bias between the tip and sample and we move the tip in a raster-like manner over the sample surface while the tunneling current is kept constant. The image is constructed by plotting the change in the z position of the tip over lateral positions.

1.4.2 STM dI/dV spectroscopy
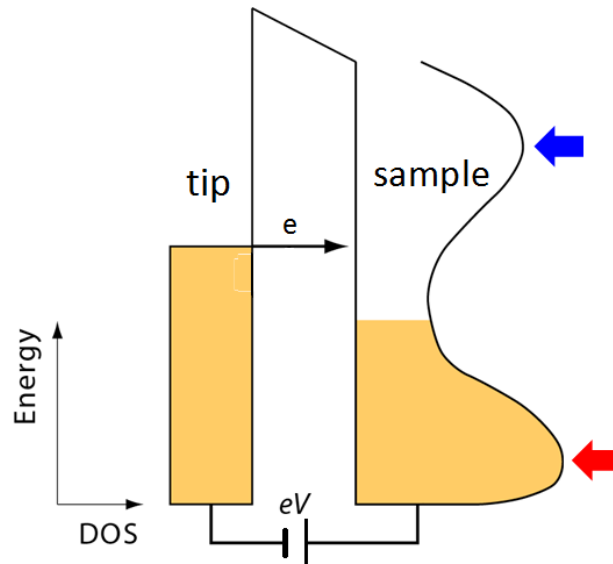
Figure 1.4: Tunneling current between the tip and sample.

In dI/dV spectroscopy, we keep the tip at a fixed position relative to the sample while sweeping the tip-sample bias. A lock-in amplifier is used to measure the dI/dV signal in order to minimize noise. Assuming that the DOS of the tip is constant, the signal of the lock-in is proportional to the sample LDOS due to dI/d$V \sim$ LDOS ($E_{\text{F}} + eV_{\text{sample bias}}$). However, in reality, the assumption of a constant DOS at the tip is not always valid. Consequently, the DOS of the tip also affects the dI/dV measurement, especially at negative sample biases. Thus, it is very important to calibrate the tip on a well-known surface before performing dI/dV spectroscopic measurement. Materials such as Au(111), Cu(111) or Ag(111)surface have well-defined surface state features and are commonly used for tip calibration. dI/dV spectra measured on these bare clean surfaces can be used as reference backgrounds.

1.4.3 STM dI/dV maps.

The STM dI/dV map is a very important technique that allows us to map the spatial distribution of the LDOS of a surface at specific energy levels. There are two common methods for taking dI/dV maps:

The first method is to measure the dI/dV signal when scanning the surface with constant current feedback. This method is simple and provides both a topographic image (z channel) and a dI/dV map (in-phase lock-in channel of dI/dV) at the same time. It is a very good method for STM systems having high thermal drift at the tip-sample junction or for sample surfaces with large height variations. However, a drawback of this method

is that the tip-sample distance changes while taking dI/dV maps in order to keep the current constant. So, the dI/dV map is not taken at the isosurface, which is very important for comparing dI/dV maps to theory calculations. Nonetheless, the dI/dV maps taken by this method compare very well to theoretical calculations for GNRs.

The second method of doing dI/dV maps is at constant height. This means that the feedback is turned off during scanning. It is important to correct the scanning slope to make sure the tip is moving on the isosurface parallel to the sample. This method requires a stable STM system without large thermal drift at the tip sample junction. Otherwise, the tip can crash into the sample surface during the measurement. In general, this method should provide better comparison with theoretical calculations.

1.5 qPlus-based atomic force microscopy

Atomic force microscopy (AFM), a descendent of STM, was invented by Binnig, Quate, and Gerger [52]. AFM provides important advantages due to its ability to scan insulating substrates [52–58]. In its most general design, the AFM consists of a cantilever (typically made of silicon or silicon nitride) with a sharp tip at the end that is used as a probe for scanning the surface. When the tip is placed close to the surface, the forces between the tip and the sample can deflect the cantilever and this deflection can be measured by a 4-quadrant photodetector. The force sensor is the heart of the AFM. Developed by Giessibl, the qPlus cantilever (also called a tuning fork) provides the following advantages over the traditional AFM design when employed as a force sensor [59,60].

1. Thermal stability: By using quartz as a cantilever material, the qPlus has been shown to be very stable under temperature variations compared to silicon cantilevers [60]. There is only very small drift of the resonance frequency due to changing temperature, which helps to reduce thermal noise sources during measurement [60].

2. Cantilever stiffness: In qPlus, the cantilever is very stiff (k ≈ 1800 N/m) which can maintain a large restoring force even with small oscillation amplitudes. Under such conditions it prevents the tip from "jump-to-contact" problems when scanning a surface that strongly interacts with the tip [59].

3. Small oscillation amplitude: The qPlus can be operated at very small amplitudes (less than 100 pm). This is very useful when operating the AFM in the repulsive regime in order to achieve high chemical bonding contrast [61].

1.5.1 Basic theory of frequency modulated atomic force microscopy (FM-AFM)
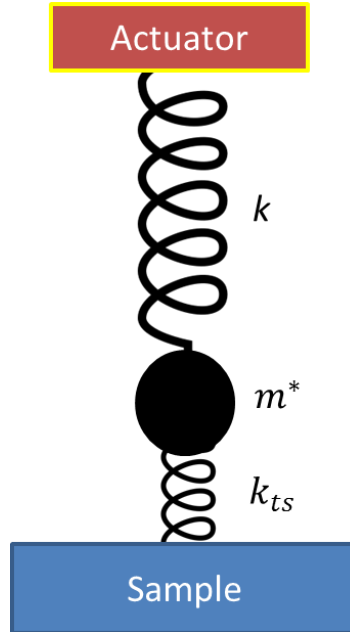
Figure 1.5: Schematics of the AFM cantilever.

In a simple model, the cantilever obeys the simple harmonic oscillator equation like a spring.

$$F = -kx$$

where F is force, k is the spring constant and x is the cantilever deflection.

So, $f_0 = \frac{1}{2\pi}\sqrt{\frac{k}{m^*}}$

where f_0 is the natural frequency of the cantilever far away from the surface, and m^* is the effective mass of the cantilever.

When the tip is brought close to the surface, there is an additional force F_{ts} between the tip and the surface that we can treat as another spring with its spring constant of $k_{ts} = -\frac{\partial F_{ts}}{\partial z}$

where z is the distance between the tip and sample.

With the reasonable approximation that $k \gg k_{ts}$, we can obtain the value for the frequency shift as below:

$$\Delta f = \frac{k_{ts}}{2k} f_0 = -\frac{f_0}{2k} \frac{\partial F_{ts}}{\partial z}$$

There are several different kinds of forces F_{ts} between the tip and the sample such as van der Waals, chemical bonding, electrostatic forces and the Pauli repulsive force, each of which dominate at different regimes of the tip-sample distance z. In FM-AFM mode, the tip is scanned in a raster-like manner over the sample surface while the frequency shift Δf is kept constant. The image is constructed by plotting the change in the z position of the tip over lateral positions.
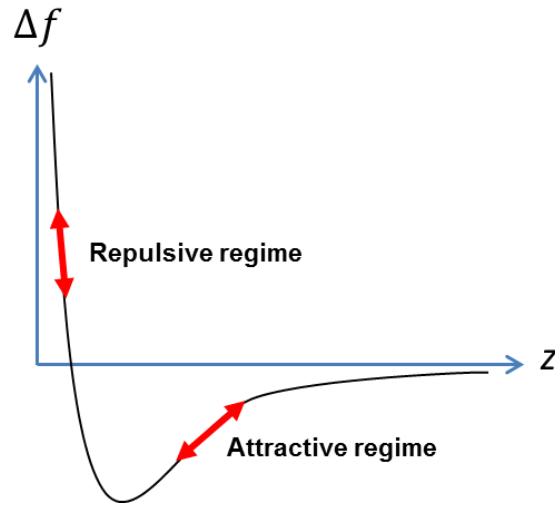
Figure 1.6: The dependence of frequency shift on the tip-sample distance.

1.5.2 FM-AFM topography in the attractive regime

In the attractive regime (the negative slope region in the curve of Figure 1.6), the van der Waals force between the tip and the sample is dominant. Although topographic images in this range provide poor resolution, the dynamic range for z control is very large. Thus, this is very useful mode for doing fast survey scanning of nanostructures on insulating substrates [53–60,62,63]. For example in Figure 1.7, we performed FM-AFM in the attractive regime in order to search for graphene edges in a sample of epitaxial graphene grown directly on a boron nitride (BN) substrate[64]. Figure 1.7a is a large scale FM-AFM topographic image (500x500 nm) in a low temperature UHV system. The image (128x128 pixels) was taken in only 15 minutes. The resolution of the image is good enough to give the information on the mono- and bilayer graphene areas as well as the bare BN surface. Figure 1.7b is a zoom-in image in the monolayer graphene area. The hexagonal structure is the 15 nm Moiré pattern of graphene on BN and is clearly visualized [64,65].
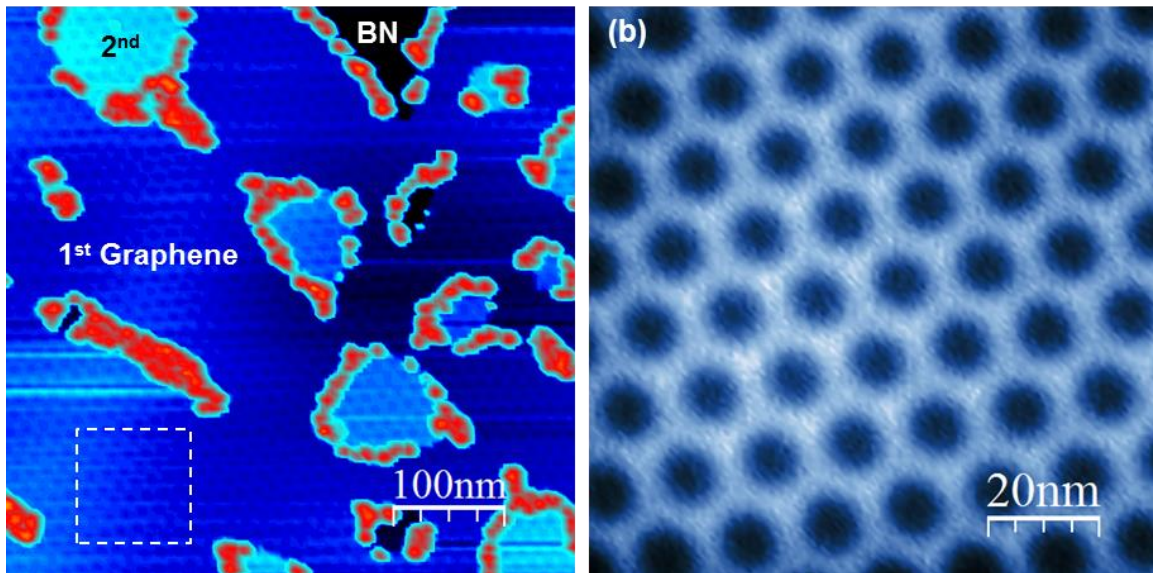
Figure 1.7: (a) FM-AFM topographic image of the 1st and 2nd layers of epitaxial graphene grown on boron nitride substrate. (b) Zoom-in FM-AFM topographic image of the white dashed square in (a) ($|\Delta f| = 2$ Hz, amplitude oscillation $= 3$ nm, $T = 4.5$ K)

This mode also has potential for applications in studying the local electronic properties of 2D material devices using low temperature UHV qPlus-based AFM & STM. 2D material devices are often small (about um scale size or even smaller) and are made on insulating substrates such as SiO_2. It is difficult to use the STM tip to search for the conducting channels on these insulating substrates. So far only the scanning gate method is considered to be successful for searching for graphene in these devices [66]. However, the spatial resolution of the scanning gate method is pretty low [66]. Using the FM-AFM mode for approaching the probe tip to the surface and scanning helps to avoid the possibility of crashing the tip into a non-conducting spot. In addition, running AFM in non-contact mode and far away from the surface protects the tip from strong interactions with the surface, minimizing tip changes during scanning. After the conductive channel is found and shown to be clean using FM-AFM, one can switch to STM mode in that area for local electronic characterization.

1.5.3 FM-AFM topography in the repulsive regime

In the repulsive regime (negative slope region in curve of the Figure 1.6), higher spatial resolution can be achieved due to the strong dependence of the frequency shift on the z distance. However, slower scan speeds are needed.

Figure 1.8 shows a FM-AFM topographic image of epitaxial graphene on BN [64] with constant frequency shift feedback mode. The image provides atomic resolution of

the graphene lattice simultaneously with the Moiré patterns of graphene on a boron nitride substrate.
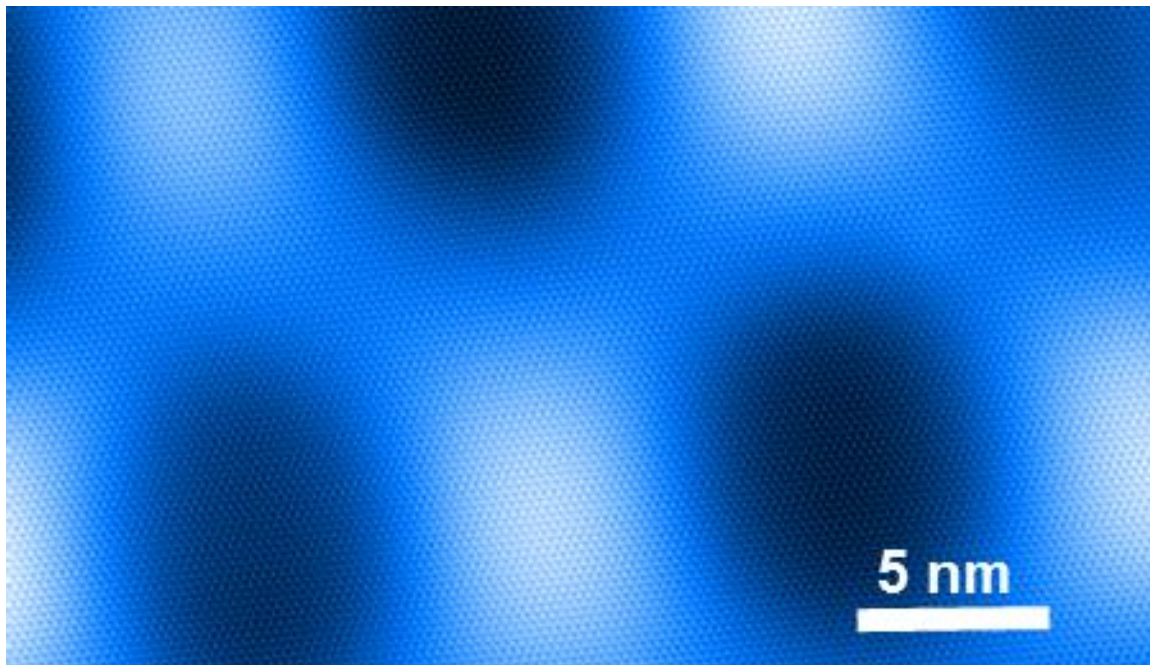
Figure 1.8: FM-AFM topographic image of epitaxial graphene grown on boron nitride substrate (Δf = 5 Hz, amplitude oscillation = 200 pm, T = 4.5 K).

1.5.4 Constant-height high resolution AFM topography with CO-functionalized tip

In the repulsive regime where the Pauli repulsive force is dominant, using a CO-functionalized tip while scanning a molecular structure in constant-height mode allows resolution of individual chemical bonds and atomic-scale structure [61,67,68].

Figure 1.9 shows an image of B-7AGNRs on Au(111). Measuring the frequency shift of the qPlus resonator while scanning over the ribbon in constant height mode with a CO-functionalized tip produced the contrast in the image. To pick up a CO molecule, the W tip is placed on top of a CO molecule with 50mV bias and 10pA tunneling current set point, then the current set point is changed to 500 pA, wait 0.5 sec, change bias to -2V, wait 0.5 sec, change the current back to 10pA, wait 0.5 sec, change bias back to 50 mV, wait for 0.5 sec, resume the scan.
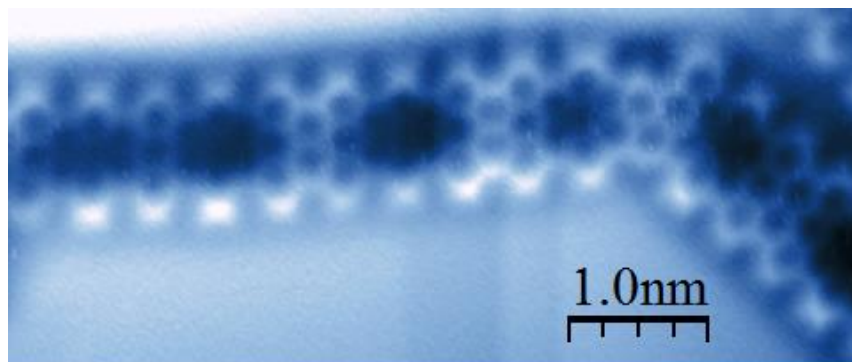
Figure 1.9: High resolution AFM image of B-7AGNR on Au(111) surface (V_s = 0 V, amplitude oscillation = 60 pm, f_0 = 25.08 kHz, Q = 19.8 k, T = 4.5 K).

1.6 Bond-resolved STM (BRSTM)

In this section, I present a new STM measurement technique, bond-resolved scanning tunneling microscopy (BRSTM), that allows investigation of bond-resolved chemical properties. This method was developed from existing techniques in which the STM tip is functionalized with adsorbates such as H_2, Xe, CH_4, CO and used to obtain chemical contrast images [69–74]. For these measurements, we chose a CO molecule for functionalizing the tip because this molecule will not affect STM spectroscopic measurements the way that H_2 does. The "effective" size of the oxygen atom in CO is also small in comparison with Xe atoms and CH_4 which helps to enhance the resolution. Theoretical simulations were performed by Yuki Sakai at University of Texas, Austin.

1.6.1 Experimental measurement setup

To accomplish BRSTM we perform a lock-in measurement in constant current mode and use the signals from both the in-phase and out-of-phase channels of the lock-in. One advantage of this mode is that the tip can be used to scan non-planer adsorbates due to the use of the feedback (as opposed to nc-AFM measurements that are typically done at constant height). At very low bias, the sample density of states (DOS) is considered constant, which means the current only depends on the distance between the tip and the surface. Therefore, in this constant current mode, the tip can follow the height profile of the surface in order to provide good contrast for images.

Figure 1.10 is used to demonstrate chemical-bond-resolved imaging when using a CO-functionalized STM tip. Without a CO functionalized tip, no chemical contrast can be resolved. Conversely, with a CO-functionalized tip, the chemical bonding structure of GNRs is revealed (Figure 1.10a-c). The origin of this chemical bond contrast will be explained in the next section for a theoretical STM model. The in-phase-signal has some signal contribution from the LDOS of the Au(111) surface states which reduces the

contrast due to the bonding orbitals on the GNRs. Conversely, the signal in the out-of-phase lock-in channel often provides the better contrasted images.
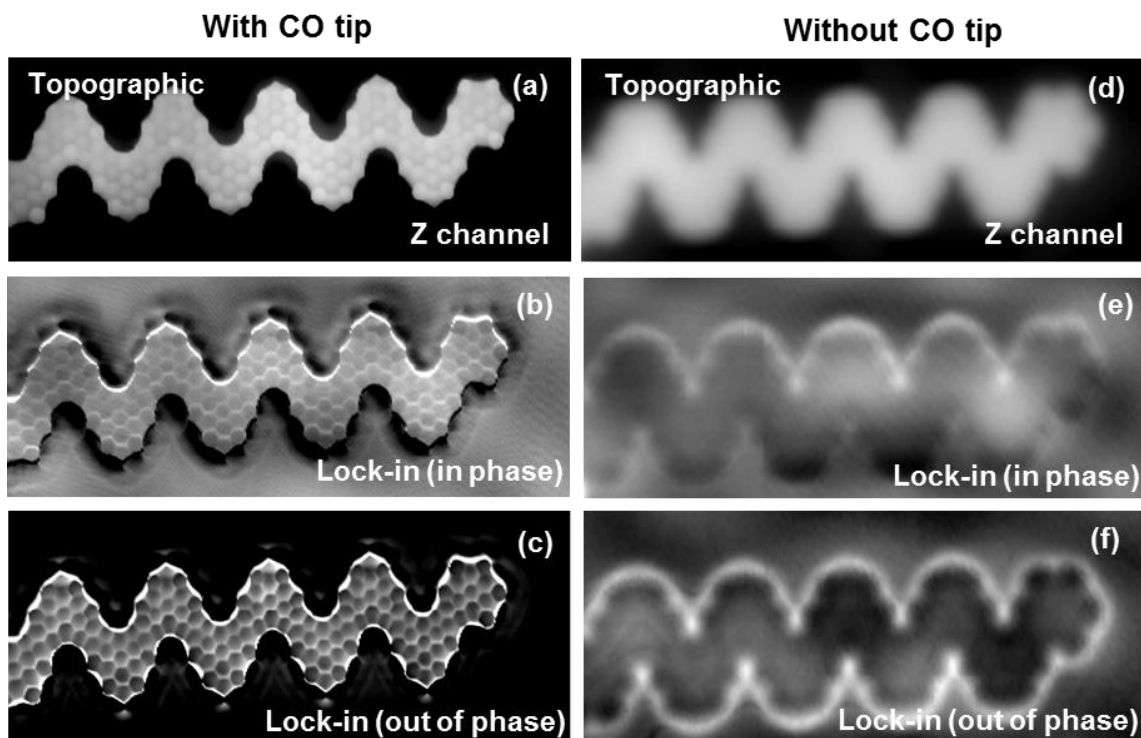
Figure 1.10: STM topographic and $\mathrm{d}I/\mathrm{d}V$ measurement with and without CO-functionalized tip on the same ketone GNR using the same scanning parameters ($V_s = 40$ mV, $I = 10$ pA, $V_{ac} = 20$ mV, $f = 401$ Hz, $T = 4.5$ K).

1.6.2 Theoretical model for bond-resolved STM (BRSTM) imaging technique

The chemical contrast in our STM measurement has the same origin as contrast obtained in nc-AFM with a functionalized tip [75]. The relaxation of the probe atom in all directions during scanning induces variation in the tunneling current. The relaxed position of the probe atom along all x, y, z directions during scanning can be obtained using a Lennard-Jones model where the tip base and the sample atoms are kept fixed [75].
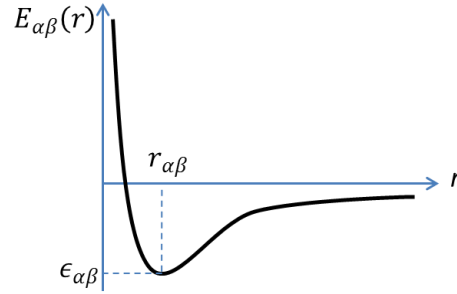
Figure 1.11: The graph of Lennard-Jones potential. $\epsilon_{\alpha\beta}$ and $r_{\alpha\beta}$ is binding energy and the equilibrium distance of the atom pair (e.g., a probe atom with each surface atom), respectively.

In the Lennard-Jones model, the potential energy and the force between a pair of atoms α, β is given by

$$E_{\alpha\beta}(r) = \frac{B_{\alpha\beta}}{r^{12}} - \frac{A_{\alpha\beta}}{r^6}$$

$$\boldsymbol{F}_{\alpha\beta}(\boldsymbol{r}) = \boldsymbol{r}(\frac{B_{\alpha\beta}}{r^{14}} - \frac{A_{\alpha\beta}}{r^8})$$

where $|\boldsymbol{r}| = |\boldsymbol{r}_\alpha - \boldsymbol{r}_\beta|$ is the distance between atoms α and β, $A_{\alpha\beta} = 2\,\epsilon_{\alpha\beta}r_{\alpha\beta}^6$ and

$$B_{\alpha\beta} = \epsilon_{\alpha\beta}r_{\alpha\beta}^{12}.$$

In a reasonable approximation, $\epsilon_{\alpha\beta} = \sqrt{\epsilon_\alpha\epsilon_\beta}$, $r_{\alpha\beta} = r_\alpha + r_\beta$

	r_α (Å)	ϵ_α (meV)
Hydrogen	1.487	0.680
Carbon	1.908	3.729
Oxygen	1.661	9.106

Table 1-1: Table of ϵ_α and r_α parameters for hydrogen, carbon and oxygen atoms from ref. [75,76].
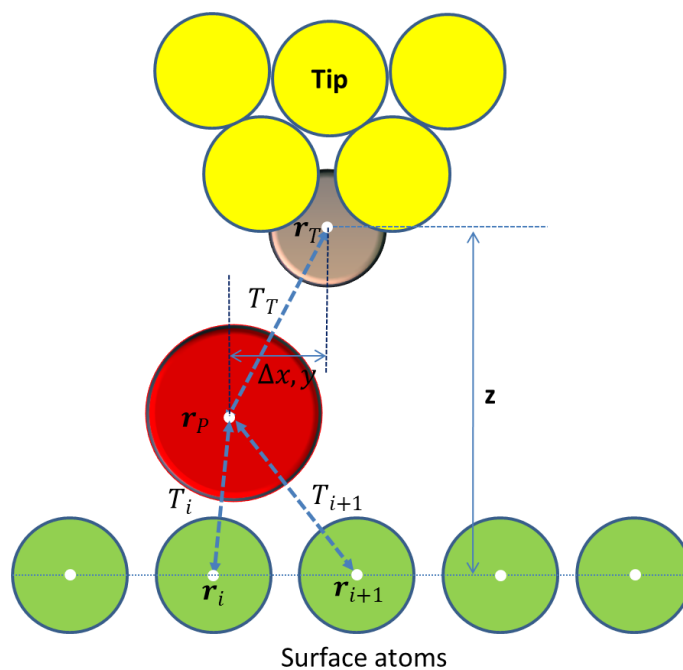
Figure 1.12: Schematic model of the CO-functionalized STM tip. The tip atoms (gold), tip base (carbon), probe atom (oxygen) and surface atoms are shown in yellow, grey, red and green, respectively. The distance z between the tip base and the surface is about ~6.9 Å.
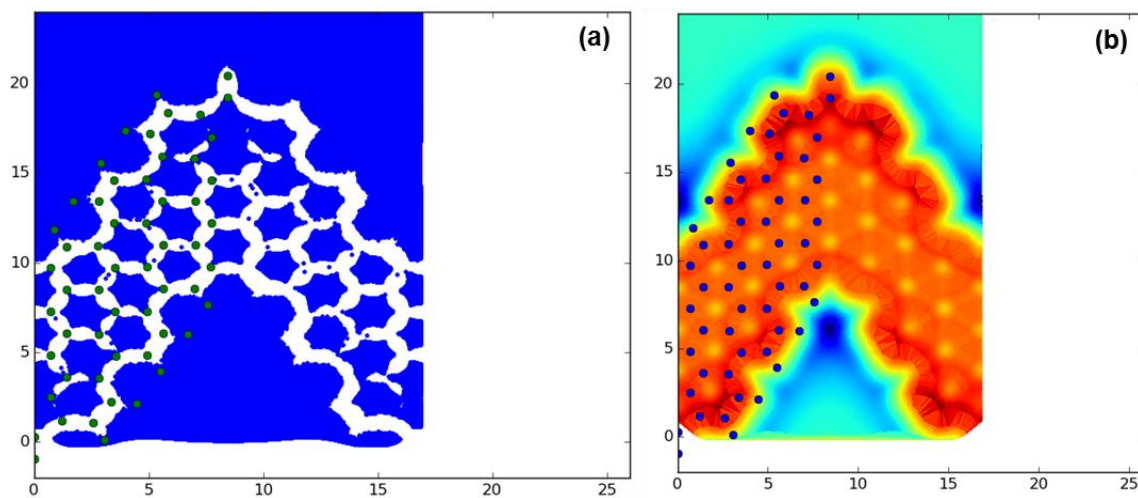
Figure 1.13: (a) The x,y position of probe atom (oxygen atom) after relaxation. Scanning with 0.05 Å grid spacing above a ketone GNR structure and the initial oxygen height of 2.9 Å (which is equivalent with set z = 6.9 Å). The dots show the positions of surface atoms.

The tunneling conductance is given by

$$\frac{dI}{dV}(\boldsymbol{r}_P, \boldsymbol{r}_T, \boldsymbol{R}_S) \propto T_T(\boldsymbol{r}_P, \boldsymbol{r}_T) T_S(\boldsymbol{r}_P, \boldsymbol{R}_S)$$

$$= T_T(\boldsymbol{r}_P, \boldsymbol{r}_T) \sum_i T_i(\boldsymbol{r}_P, \boldsymbol{r}_i)$$

where $\boldsymbol{r}_P, \boldsymbol{r}_T, \boldsymbol{R}_S$ are position vectors of the probe atom, the tip base atom and the surfaces atoms respectively. $\boldsymbol{r}_i$ is the position vector of individual atoms on surface. T_T, T_S and T_i represent the tunneling transmissivities from the tip to the probe atom and from the probe atom to the sample which can be expressed as the exponential functions below.

$$T_S \propto \exp(-\beta_S |\boldsymbol{r}_P - \boldsymbol{r}_i|)$$

$$T_T \propto \exp(-\beta_T |\boldsymbol{r}_P - \boldsymbol{r}_T|)$$

where β_S and β_T are inverse decay lengths on the order of 1 Å^{-1}

In the case of a CO-functionalized tip, there is a very stiff covalent bond between CO and the tip that leads to only small changes in the tip-probe atom distance as the tip is scanned across the surface. Thus, we can ignore the contribution of the T_T channel into the BRSTM contrast [75]. So, in our theoretical calculation, we only use the sum of the tunneling processes between the probe atom and the atoms on the surface for simulating BRSTM images. Using this method, we obtain a simulated STM image for a unit cell of ketone GNR (Chapter 4&5) in Figure 1.14.
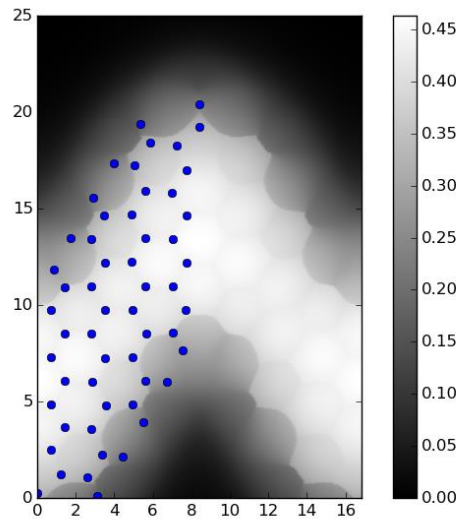
Figure 1.14: Simulated BRSTM image using tunneling probability T_S with the tip height z = 6.9 Å. The dots show the positions of surface atoms.

In order to theoretically explain excellent contrast of BRSTM images, we have to take into account the orientation-dependent tunneling due the p-orbitals of the probe atom (oxygen) as well as the surface atoms which are carbon in hexagonal structure and oxygen (more information can be found in the supplement for reference [75]).
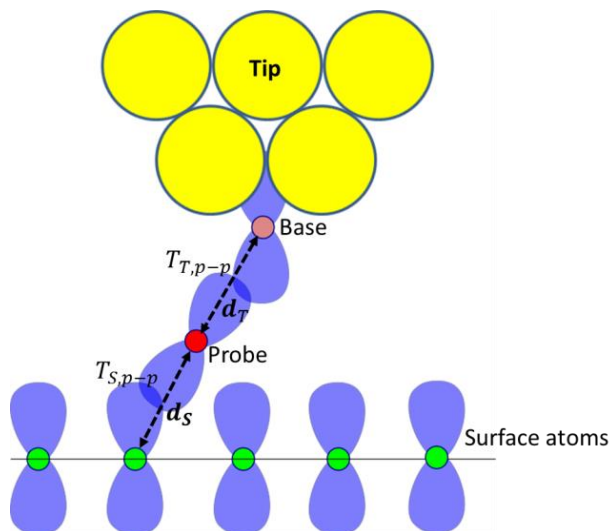
Figure 1.15: Tight binding model for tunneling probability between two p-orbitals on different atoms.

Taking this into account allows us to obtain simulated BRSTM images such as Figure 1.16, which nicely match experimental Figure 5.1.
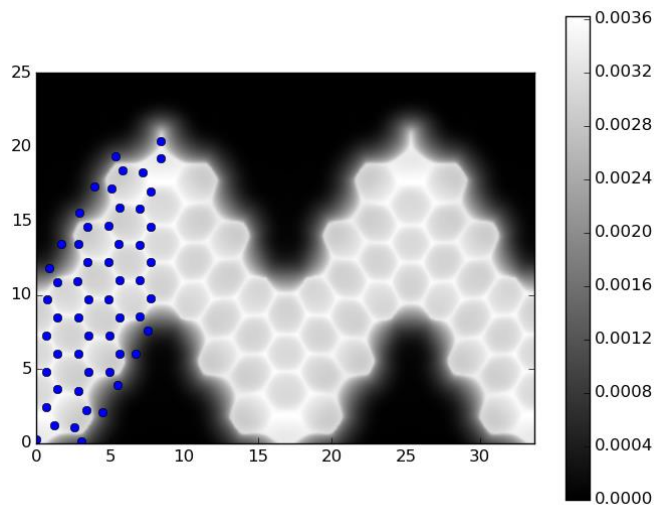
Figure 1.16: Simulated BRSTM image for a ketone GNR using tunneling probability T_S with p-orbital (z = 7 Å). The dots show the positions of surface atoms.

1.7 Instrumentation

For this dissertation, all measurements were performed using two STM instruments:

1. Home built VT-STM: This is a homebuilt variable-temperature ultra-high vacuum STM with optical access to the tip-sample junction. The machine was designed and built by Katsumi Nagaoka, Mike Crommie, Hadrian Knotz, and David Kwon [77]. There are significant modifications to the system performed by Matt Comstock [77], Niv Levy [78], Luis Berbil-Bautista, Jong Cho [79], Ivan and me [80].

2. Omicron LT system: This is a commercial Omicron STM & AFM low temperature system.

Chapter 2 : Bottom-up Synthesis of N=13 Sulfur-doped Graphene Nanoribbons

In this chapter, we report the fabrication and nanoscale characterization of atomically-precise N=13 armchair graphene nanoribbons featuring regioregular edge-doping with sulfur atoms (S-13-AGNRs) on a Au(111) surface. Scanning tunneling spectroscopy and first principle calculations reveal modification of the electronic structure of S-13-AGNRs when compared to undoped N=13 AGNRs.

This chapter is adapted with permission from G. D. Nguyen et al., "Bottom-up Synthesis of N=13 Sulfur-doped Graphene Nanoribbons", J. Phys. Chem. C **120**, 2684 (2016).

2.1 Introduction

Graphene nanoribbons (GNRs) are quasi-one-dimensional strips of graphene that exhibit novel electronic and magnetic properties [16,19,20,24,81,82]. These properties can be tuned by engineering GNR structural parameters such as width [17,33–35] and edge symmetry [16,17,23,83]. Recent advances in bottom-up GNR synthesis have yielded new techniques for modulating GNR width [16,17,35] and for introducing dopant heteroatoms [19,36,38,40] with atomic precision both along the GNR edge and, more recently, along the backbone [36,39]. Up to now, however, edge-doping in bottom-up fabricated GNRs has exclusively relied on the introduction of nitrogen heteroatoms in the form of pyridine and pyrimidine rings along the edges of chevron GNRs [19,38,40]. In this position the electron lone-pair on the trigonal planar nitrogen atoms is not in conjugation with the GNR aromatic π-system. Rather than significantly affecting the GNR density of states or energy gap, the electronegative N-atoms only induce a rigid shift of the energies of both the valence and conduction bands [19,38].

In this chapter, we report the bottom-up synthesis and characterization of atomically-precise N=13 armchair graphene nanoribbons (S-13-AGNRs) wherein alternating (CH)$_2$ groups lining the edges of the GNRs have been replaced by sulfur atoms. This alternative edge-doping pattern places one of the lone-pairs (having p-character) on trigonal planar S-atoms in full conjugation with the extended π-system of the 13-AGNR. Molecular precursors for S-13-AGNRs (**1** in Figure 2.1) are derived from 10,10'-dibromo-9,9'-bisanthracene and feature (2-phenyl)thiophene substituents. A sub-monolayer of **1** was deposited onto a Au(111) surface under ultrahigh vacuum (UHV). Subsequent heating of the decorated Au(111) surface to 200 °C induces a radical step-growth polymerization to give *poly*-**1**. A second annealing step (400 °C) induces a thermal cyclodehydrogenation to yield fully conjugated S-13-AGNRs. Both scanning tunneling microscopy (STM&STS) and Auger electron spectroscopy (AES) were used to

investigate the structure and to probe the electronic states of the resulting S-13-AGNRs. STS measurements reveal a LUMO state (lowest unoccupied molecular orbital) for S-13-AGNRs at approximately the same energy as previously recorded for undoped 13-AGNRs. When compared to undoped 13-AGNRs, the density of states (DOS) associated with the LUMO in S-13-AGNR spans a significantly broader energy range. These results are consistent with ab-initio simulations of S-13-AGNRs that indicate a sulfur-induced increase in the energy separation between CB and CB+1 as well as between VB and VB–1 13-AGNR band edges (here CB refers to the conduction band and VB refers to the valance band).

2.2 Molecular Synthesis
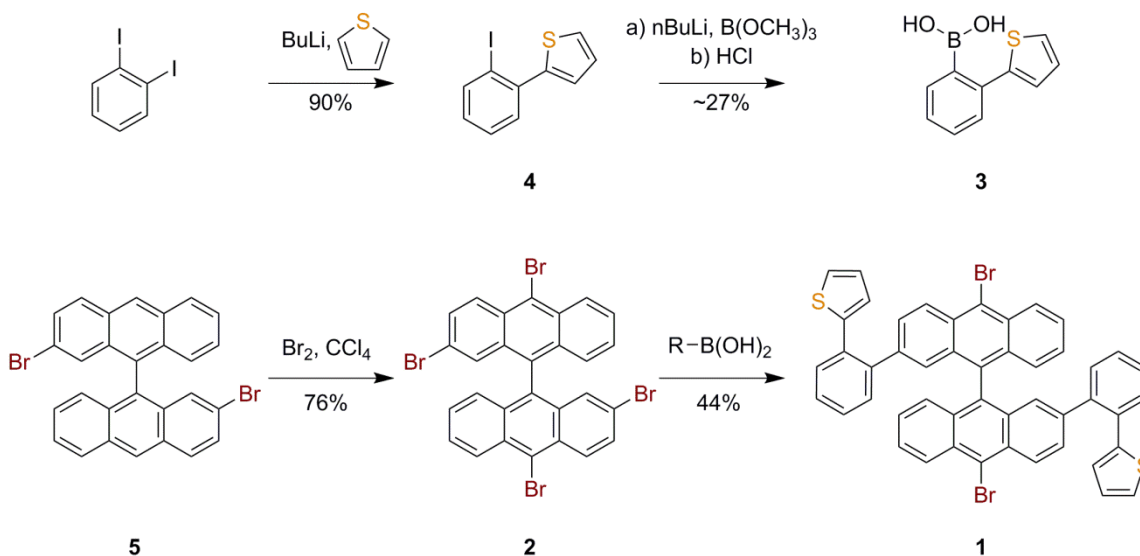
Figure 2.1: Synthesis of sulfur doped GNR molecular precursor **1**

The molecular precursor for S-13-AGNRs **1** (Figure 2.1) was synthesized through a Suzuki cross-coupling of 2,2',10,10'-tetrabromo-9,9'-bianthracene (**2**) with two equivalents of (2-(thiophen-2-yl)phenyl)boronic acid (**3**). Oxidative addition favors the sterically less hindered 2,2'-position in the bisanthracene backbone and yields the desired regioisomer **1** as the major product in 44% yield.

2.3 Bottom-up growth of S-13-AGNRs
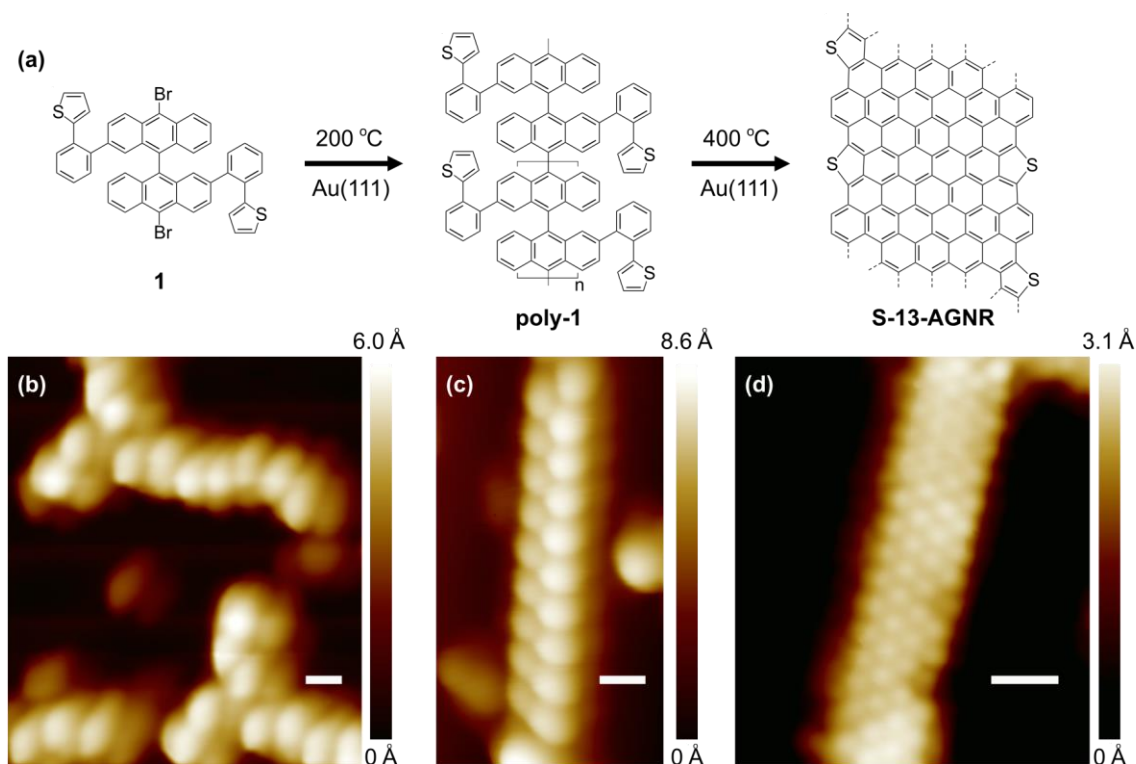
Figure 2.2: (a) Reaction scheme for bottom-up synthesis of S-13-AGNRs. Annealing at 200 °C induces radical step-growth polymerization. Annealing at 400 °C induces cyclodehydrogenation to yield S-13-AGNRs. (b) STM image of precursor **1** as deposited onto a Au(111) surface (V_s = 2.0 V, I_t = 20 pA, T = 13 K). (c) STM image of a *poly*-**1** (after first annealing step) shows characteristic pattern of alternating protrusions (V_s = 2.0 V, I_t = 20 pA, T = 13 K). (d) STM image of a fully cyclized S-13-AGNR (V_s = 0.1 V, I_t = 15 pA, T = 7 K). Scale bars are 1 nm.

A polished Au(111) single crystal was used as the substrate for the STM measurements. Standard Ar^+ sputtering/annealing cycles were applied to prepare an atomically clean Au(111) surface. The molecular building block **1** was evaporated from a home-built Knudsen cell evaporator and the deposition rate was calibrated in a test chamber using a quartz crystal microbalance (QCM). **1** was sublimed at 478 K onto a 298 K Au(111) substrate under UHV for about 2 minutes to obtain 30–90 % coverage.

STM measurements were performed on two home-built low-temperature STMs operating at 13 K and 7 K. Both tungsten and PtIr tips were used for STM topographic measurements in constant current mode.

Figure 2.2b shows an STM image of **1** on Au(111) as deposited. The molecules tend to aggregate into irregular islands along the Au(111) herringbone reconstruction with an average height of 0.5 nm. Annealing the molecule-decorated sample at 200 °C for 20 min induces homolytic cleavage of the labile C–Br bonds in **1** followed by radical step-growth polymerization of the intermediate diradical to give *poly*-**1** (Figure 2.2a). A representative STM image of a linear chain of *poly*-**1** on Au(111) is depicted in Figure 2.2c. Analogous to the polymer precursor for undoped 13-AGNRs, *poly*-**1** exhibits a pattern of alternating protrusions associated with the preferred conformation of the (2-phenyl)thiophene substituents on the Au(111) surface (the periodicity of the protrusions is 0.83 ± 0.02 nm with an apparent height of 0.43 ± 0.02 nm) [16,17,36]. Further annealing of Au(111) samples at 400 °C for 20 minutes induces a thermal cyclodehydrogenation which converts *poly*-**1** into fully cyclized S-13-AGNRs (Figure 2.2d). The average height and width of the resulting S-13-AGNRs are 0.23 ± 0.01 nm and 1.9 ± 0.2 nm respectively, and are comparable with the dimensions previously reported for undoped 13-AGNRs (0.21 ± 0.01 nm and 1.9 ± 0.2 nm) [17,20].
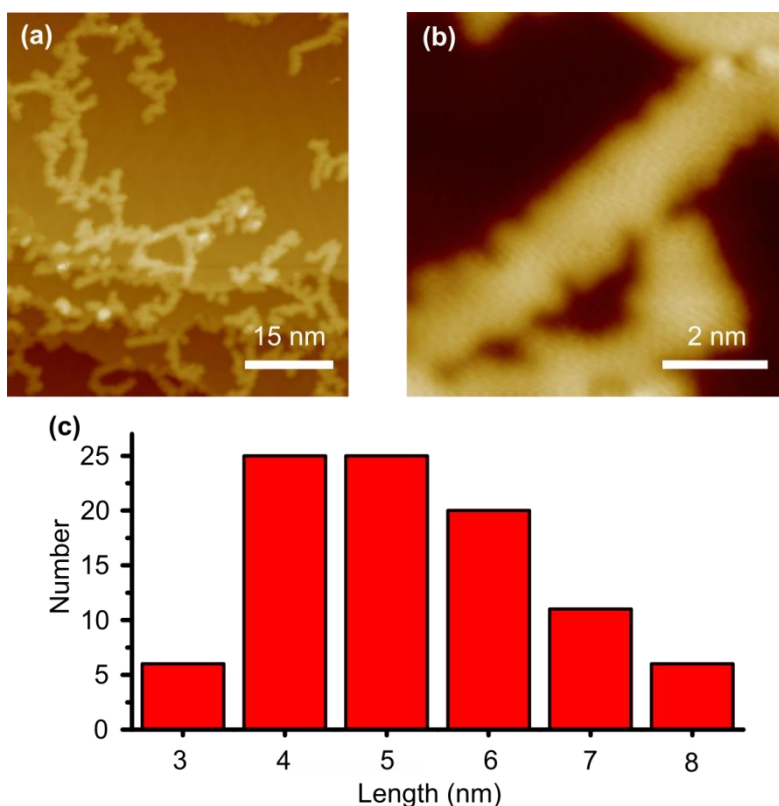
Figure 2.3: (a) Large scale STM topographic image of S-13-AGNRs ($V_s = -0.1$ V, $I_t = 20$ pA, $T = 7$ K). (b) STM topographic image of a defective 13-S-AGNR ($V_s = -0.05$ V, $I_t = 35$ pA, $T = 7$ K). (c) Length distribution of S-13-AGNRs.

Statistical analysis of STM images shows that the average length of S-13-AGNRs obtained by this growth procedure is 5 nm. We observe some irregular edge structure in our samples following the final cyclodehydrogenation step (Figure 2.3a,b). These defects might arise from the additional strain induced along the edges of GNRs by the introduction of 5-membered thiophene rings or by deletion of the thiophene ring through fragmentation of the (2-phenyl)thiophene C–C bond during the thermal annealing at 400 °C.

2.4 Auger spectroscopy of S-13-AGNRs

The Auger spectra show evidence of the presence of sulfur on the sample both after deposition of the molecules and after annealing the sample up to 400 C. This shows that sulfur is still present after the sample is brought to the temperature at which fully cyclized sulfur-doped graphene nanoribbons (S-13-AGNRs) are formed.

	ΣC_{KLL}	ΣS_{LMM}	$\Sigma C_{KLL}/\Sigma S_{LMM}$
Nominal [$C_{48}H_{28}Br_2S_2$]	-	-	24
Precursor molecules on Au(111)	2517865	110877	23
S-13-AGNRs on Au(111)	2516645	84413	30

Table 2-1: ΣC_{KLL} and ΣS_{LMM} are the integrated areas (in arbitrary units) for the C_{KLL} and S_{LMM}.

Auger transitions taken from the Auger spectra in Figure 2.4b and normalized by the sensitivity factors for carbon (0.2) and sulfur (0.8) [84]. The experimental $\Sigma C_{KLL}/\Sigma S_{LMM}$ ratio is 23 for the precursor molecules on Au(111), and 30 for S-13-AGNRs on Au(111). These values are in reasonable agreement (within the experimental error of 20% [85–87]) with the carbon to sulfur ratio of the precursor molecule **1** [$C_{48}H_{28}Br_2S_2$], which is 24.
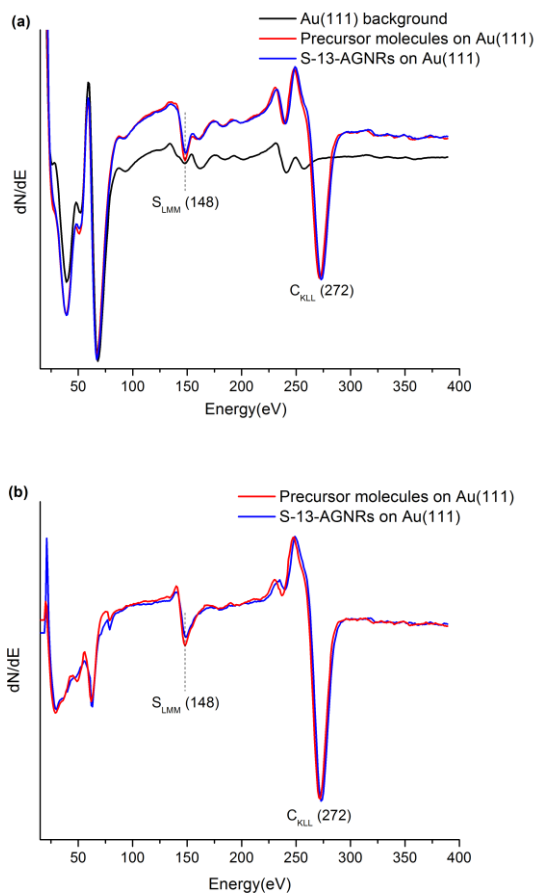
Figure 2.4: (a) Auger spectra of bare Au(111), Au(111) decorated by precursor molecules, and Au(111) decorated by S-13-AGNRs (primary electron energy E_p = 3 keV, modulation voltage E_{pp} = 5 mV). (b) Auger spectra for precursor molecules on Au(111) and S-13-AGNRs on Au(111) after subtracting the Au(111) background and correcting for the background offset (due to the non-linearity of the secondary electron contribution), to allow for C and S quantification.

2.5 STM spectroscopy of S-13-AGNRs on Au(111)

The local electronic structure of S-13-AGNRs was characterized by recording dI/dV spectra at various positions above the S-13-AGNR decorated surface. Figure 2.5 shows typical dI/dV spectra measured at the center and edges of an S-13-AGNR compared to a reference spectrum measured with the STM tip placed above the bare Au(111) substrate. The Au(111) reference spectrum is dominated by a peak centered at a sample bias of V = –0.3 V which drops steeply for $V \leq$ –0.5 V. This feature is known to originate from the Au(111) surface state [88], which has a band edge at 0.5 eV below the

Fermi energy E_F (E_F corresponds to $V = 0$). All spectra recorded with the STM tip positioned above S-13-AGNRs show a peak for $V < 0$ that is similar to the peak observed when the tip is held above bare Au(111). This makes it difficult to discern whether this feature (when seen at locations above an S-13-AGNR) is due to the intrinsic S-13-AGNR electronic structure (such as the valence band edge) or is due to the underlying Au(111) surface state. A more unambiguous S-13-AGNR spectral feature is observed at $V = 1.22 \pm 0.23$ V. Here a peak can be seen in the dI/dV spectra at the S-13-AGNR edges that is not observed at either the S-13-AGNR center or in the Au(111) reference spectrum. This behavior is consistent with the spectral signature of GNR band edge states observed previously for N = 5, N = 7 and N = 13 AGNRs [17,20,35,89], and is assigned to the S-13-AGNR conduction band edge. This band edge feature lies at almost the same energy as the undoped 13-AGNR conduction band edge ($V = 1.21 \pm 0.06$ V) [17], but is significantly broadened with a full width at half maximum (FWHM) of $\Delta E = 0.37 \pm 0.2$ eV compared to $\Delta E = 0.19 \pm 0.07$ eV for the undoped 13-AGNR.
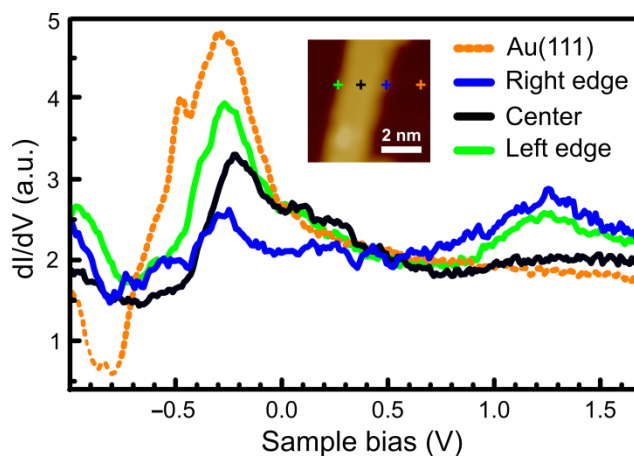
Figure 2.5: dI/dV spectra of S-13-AGNRs at different spatial positions compared to reference spectrum obtained on bare Au(111). Crosses in topographic STM image (inset) indicate the positions of recorded spectra ($T = 13$ K).

2.6 DFT theoretical calculation and discussion

First-principles calculations of sulfur-doped graphene nanoribbons were performed using DFT in the local density approximation implemented in the Quantum Espresso package [90]. A supercell arrangement was used, with the cell dimension carefully tested to avoid interactions between the nanoribbon and its periodic image. We used norm-conserving pseudopotentials [91], with a planewave energy cut-off of 60 Ry. The structure was fully relaxed until the force on each atom was smaller than 0.02 eV/Å. All the σ dangling bonds of carbon atoms on the edge of the nanoribbon were capped by hydrogen atoms. The unit cell dimension along the periodic direction is fully relaxed. The cell sizes along the nanoribbon plane normal direction and edge normal direction are set

to 13 Å and 30 Å, respectively, in order to avoid interactions between the S-13-AGNR and its periodic images. The Gaussian broadening used in plotting the density of states is 0.1 eV.
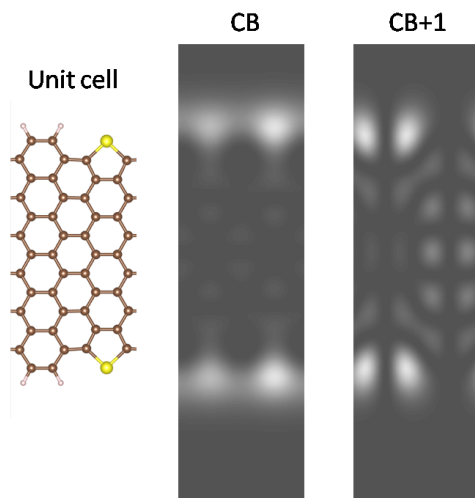
Figure 2.6: Calculated local density of states (LDOS) of the CB and CB+1 band edges at a height of 4 Å above the nanoribbon plane.

As seen from the two plots, the local density of states at the edges of the nanoribbon is larger than in the nanoribbon interior. This behavior is consistent with the experimental observation that dI/dV intensity at the edges is larger than in the interior (Figure 2.5).
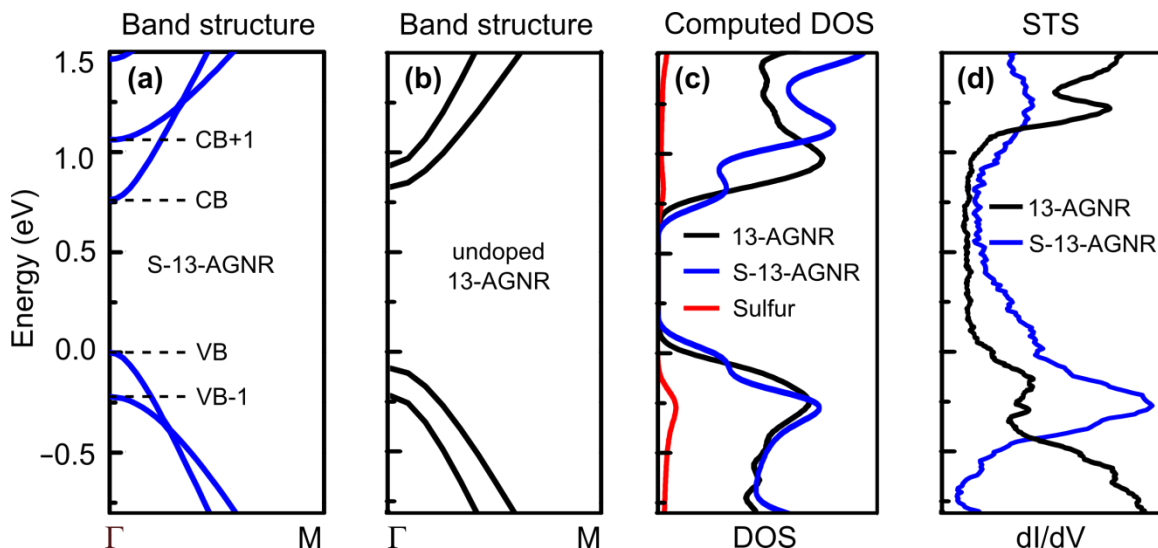
Figure 2.7: Computed band structures of (a) an S-13-AGNR and (b) a pristine 13-AGNR. (c) Calculated density of states (DOS) of an S-13-AGNR (blue), as well as the partial density of states (PDOS) of sulfur orbitals (red), and the DOS of a pristine 13-AGNR (black) (Gaussian broadened by 0.1 eV). (d) Experimental dI/dV spectrum for an S-13-AGNR (blue) compared to the dI/dV spectrum for a pristine 13-AGNR (black).

In order to better understand how the electronic properties of 13-AGNRs are affected by substitutional sulfur edge-doping, we performed density functional theory (DFT) calculations within the local density approximation (LDA) for both S-doped (Figure 2.7a) and undoped (Figure 2.7b) free-standing 13-AGNRs. Our calculations suggest that incorporation of sulfur atoms into the armchair edges only slightly reduces the band gap (at the DFT-LDA level) of a pristine 13-AGNR, from 0.90 eV to 0.76 eV. In addition, when referenced to the vacuum potential, the CB minimum and VB maximum of S-13-AGNRs have similar energy alignment compared to pristine 13-AGNRs. This behavior is quite different from the previously studied case of nitrogen edge-doped chevron GNRs, whose band edges undergo a nearly rigid shift of ≈ –0.5 eV compared to undoped chevron GNRs [19]. This difference in behavior for N-doped and S-doped GNRs can be explained by the small difference in electronegativity between sulfur and carbon as compared to the large difference between nitrogen and carbon [92]. Furthermore, the sulfur edge-doping causes a significant increase in the energy difference between the CB and CB+1 band edges, as well as between the VB and VB–1 band edges, when compared with pristine 13-AGNRs (Figure 2.7). This modification to the electronic structure is due to the strong hybridization of S-dopant orbitals with the aromatic network in S-13-AGNRs (Figure 2.7c) (due to conjugation of the S lone pair with the π-system).

The calculated band structure of S-13-AGNRs is consistent with the experimentally observed dI/dV spectra of Figure 2.7d. The experimental conduction band

edge of S-13-AGNRs is very closely aligned with the conduction band edge observed for undoped 13-AGNRs (similar to the simulated DOS depicted in Figure 2.7c). The significant broadening of the experimental LUMO feature for S-13-AGNRs compared to undoped 13-AGNRs is consistent with the predicted increase in energy separation between the CB and CB+1 band edges for S-13-AGNRs as compared to undoped 13-AGNRs (Figure 2.7). The reason that the experimental measurement shows only a single feature instead of two peaks is likely due to broadening arising from interaction between S-13-AGNRs and the gold substrate [93].

2.7 Summary

In conclusion, we have demonstrated the successful bottom-up synthesis of substitutional sulfur edge-doped 13-AGNRs on Au(111), as well as determination of the effect of sulfur edge-doping on the electronic structure of N=13 AGNRs. Both the theoretically determined and experimentally measured S-13-AGNR electronic structure are consistent with the hybridization of sulfur orbitals with the conjugated π-system of the extended carbon network. This characteristic leads to enhanced energy separation of the CB (VB) and CB+1 (VB-1) band edges but, because sulfur and carbon electronegativities are similar, the energy alignments of N=13 AGNR bands remain relatively unchanged by sulfur doping.

Chapter 3 : Bottom-up Synthesis of Boron-doped N=7 Armchair Graphene Nanoribbons

In this chapter, we report the atomically precise introduction of group III dopant atoms into bottom-up fabricated semiconducting armchair GNRs (AGNRs). Trigonal-planar boron atoms along the backbone of the GNR share an empty p-orbital with the extended π-band for dopant functionality. Topographic and local electronic structure characterization was performed via STM and CO-tip-functionalized nc-AFM, and compared to DFT simulations.

This chapter is adapted with permission from R. R. Cloke et al., "Site-Specific Substitutional Boron Doping of Semiconducting Armchair Graphene Nanoribbons", J. Am. Chem. Soc., 137, 8872 (2015) and a prepared manuscript titled "Band Gap Reduction of Bottom-up Graphene Nanoribbons due to Boron Doping". The coauthors are Giang D. Nguyen, Arash A. Omrani, Hsin-Zon Tai, Ting Cao, Ryan R. Cloke, Tomas Marangoni, Daniel J. Rizzo, Trinity Joshi, Christopher Bronner, Won-Woo Choi, Chen Chen, Zahra Pedramrazi, Steven G. Louie, Felix R. Fischer and Michael F. Crommie.

3.1 Introduction

Recent advances in the bottom-up fabrication of atomically precise GNRs from molecular precursors have demonstrated the rational modulation of the width, the symmetry, the edge structure (armchair, chevron, cove), and the incorporation of nitrogen atom dopants in the form of pyridine and pyrimidine rings into the edges of chevron-GNRs [17,20,38,94–97]. Since the lone-pair of the N-heteroatom in these structures is not in conjugation with the extended π-system of the GNR, edge-doping only shifts the position of both the conductance and valence band edges of the ribbon without introducing dopant states into the gap [19,38]. Controlled n-/p-doping, i.e., the controlled introduction of filled/empty donor or acceptor states into the gap of atomically defined GNRs, instead requires the incorporation of dopant heteroatoms at precise positions along the backbone of the ribbon where the filled/empty p-orbitals are in conjugation with the extended π-system.

In this chapter, we report an experimental study focused on more accurately characterizing the electronic properties of B-7AGNRs in order to test theoretical predictions regarding B-7AGNR electronic structure. To accomplish this we have used STS to probe the local electronic properties of B-7AGNRs on both Au(111) and Ag(111) substrates, and have compared these results to theoretical DFT-GW simulations. The additional use of Ag(111) as a substrate allows us to change how the B-7AGNR

electronic structure hybridizes with the Shockley surface state known to inhabit the close-packed faces of FCC metals [98], Since the Ag(111) surface state band edge lies at a higher energy then the Au(111) surface state, the B-7AGNR valence band structure is more readily apparent for B-7AGNRs on Ag(111) compared to Au(111). Combining this fact with a strategy of comparing both point spectra and dI/dV maps to theoretical predictions allows us to confidently assign conduction and valence band features for B-7AGNRs on Ag(111). Armed with the new insight gained by examining B-7AGNRs on Ag(111), we are able to better understand the behavior of the more difficult B-7AGNR/Au(111) system. Overall, this provides us with strong experimental evidence for a new boron-induced unoccupied band in B-7AGNRs on Ag(111) and Au(111), consistent with theoretical predictions [21]. We find that the band gap for B-7AGNRs on Ag(111) is 1.4 ± 0.1 eV, while the band gap for B-7AGNRs on Au(111) is 1.3 ± 0.3 eV, both of which are significantly less than the band gap of pristine N=7 AGNRs on Au(111) (2.5 ± 0.1 eV) [17,89].

3.2 Molecular Synthesis

The boron-doped 7-AGNR precursor **1** was obtained through selective monolithiation of 9,10-dibromo-anthracene (**2**), followed by borylation with 5,10-dibromo-5,10-dihydroboranthrene (**3**) in 73% yield (Figure 3.1). Despite the reported instability of this class of substituted boranthrenes, crystals of **1** are stable in air at 24 °C showing no signs of degradation over several months, as indicated by ^{1}H NMR spectroscopy [99–101]. DSC and TGA analysis reveals a melting point above 350 °C and a gradual mass loss associated with partial dehalogenation above this temperature.

Orange crystals of **1** suitable for X-ray diffraction were obtained by slow evaporation of a $C_2H_2Cl_4$ solution. **1** adopts a C_i symmetry in the crystal lattice. The geometry around the boron atom is trigonal-planar with bond angles and bond distances ranging between 119.7–120.9° and 1.56–1.78 Å, respectively. While the two 9-bromoanthracene units are coplanar, the central boranthrene is twisted out of planarity with a dihedral angle C(2)–C(1)–B(1)–C(15) = 97.6°. This nonplanar conformation is crucial as it sterically shields the Lewis acidic B atoms from nucleophilic attack and imparts a favorable nonplanar geometry to the molecule, a prerequisite for an efficient radical step-growth polymerization on the Au(111) substrate [16,17,19,38,89,94–96,102–105].
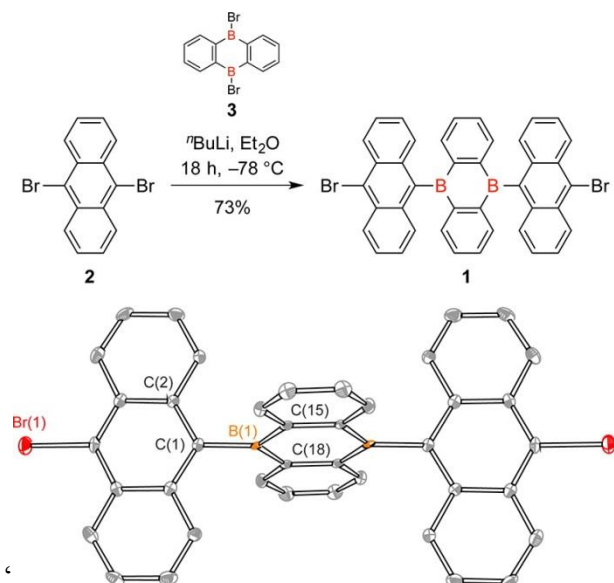
Figure 3.1: Synthesis of the B-doped molecular precursor **1** (top). ORTEP representation of the X-ray crystal structure of **1** (bottom). Thermal ellipsoids are drawn at the 50% probability level. Color coding: C (gray), Br (red), B (orange). Hydrogen atoms and cocrystallized solvent molecules are omitted for clarity. Relevant structural parameters: C(1)–B(1), 1.578(5) Å; C(15)–B(1), 1.561(5) Å; C(18)–B(1), 1.562(5) Å; C(2)–C(1)–B(1)–C(15), 97.6°; $C_{46}H_{30}B_2Br_2Cl_{12}$; 1189.54 g mol^{-1}; triclinic; P–1; orange; a = 8.6046(3) Å; b = 9.8632(4) Å; c = 14.5013(6) Å; α = 82.148(2)°, β = 82.067(2)°; γ = 74.011(2)°; 100 (2) K; Z = 1; R1 = 0.0387; GOF on F^2 = 1.036.

3.3 Bottom-up fabrication of B doped N=7 AGNRs on Au(111)

Fully cyclized B-7AGNRs were fabricated by sublimation of molecular building block **1** at 250–270 °C in UHV onto pristine Au(111) held at 24 °C. STM imaging at 13 K prior to polymerization reveals that the molecules assemble into irregular islands with an apparent height of 0.4 nm (Figure 3.2b), clustered around the Au(111) herringbone reconstruction. Gradual annealing of submonolayer samples of **1** on Au(111) to 220 °C (20 min) induces homolytic cleavage of the labile C–Br bond, followed by step-growth polymerization of the carbon-centered diradical intermediates to form extended linear polymer chains *poly*-**1** (Figure 3.2c). STM images of polymer chains display a characteristic pattern of alternating protrusions (average distance between white markers 0.95 ± 0.04 nm, Figure 3.2d) along the polymer backbone. The repulsive interaction between *peri*-hydrogen atoms in adjacent anthracene units prevents a coplanar arrangement of monomer units in the polymer backbone (this observation is consistent with images of polyanthracene, the precursor to undoped 7-AGNRs) [16,103]. Unique to the B-doped GNR precursors is a distinctive secondary structure along the polymer that

correlates with the length of a monomer unit (Figure 3.2a) in *poly*-**1** (average distance between black markers 1.40 ± 0.04 nm, Figure 3.2d). While the anthracene fragments appear as brighter spots in topographic STM images, the more electron-deficient boranthrenes correlate with a weaker signal that alternates along the edges of the polymer. The observation of this characteristic secondary pattern in images of *poly*-**1** indicates that the exocyclic B–C bonds are stable under the polymerization conditions and no undesired fragmentation of monomer building blocks is observed during the step-growth process.
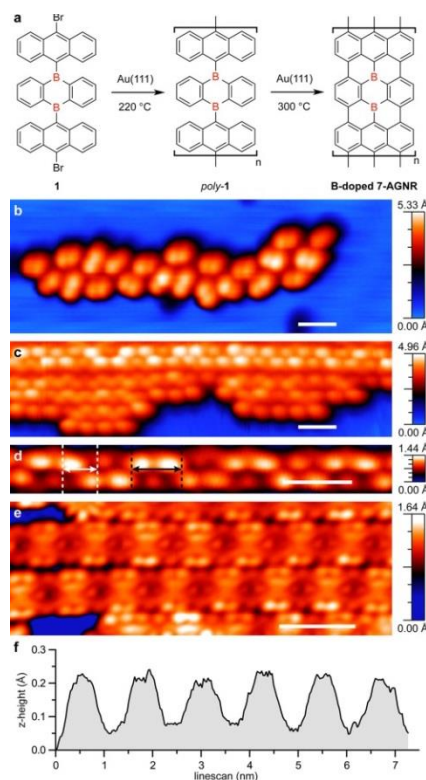
Figure 3.2: (a) Schematic representation of the bottom-up synthesis of B-7AGNRs. (b) STM topographic image of molecular building block **1** as deposited onto a pristine Au(111) surface held at 24 °C (V_s = 1.5 V, I_t = 30 pA, T = 13 K). Subsequent annealing steps induce the homolytic cleavage of the labile C–Br bonds, followed by radical step-growth polymerization (220 °C) and thermal cyclization/dehydrogenation (300 °C) to yield B-7AGNRs. (c) STM topographic image of *poly*-**1** (V_s = 1.0 V, I_t = 20 pA, T = 13 K). (d) STM topographic image of poly-**1** showing a characteristic pattern of alternating protrusions (V_s = 1.0 V, I_t = 20 pA, T = 13 K). (e) STM topographic image of fully cyclized B-7AGNRs (V_s = −0.1 V, I_t = 3 pA, T = 4.5 K). (f) Representative *z*-axis profile showing the characteristic height modulation along the long axis of a B-7AGNR. Scale bar is 2 nm.

Further annealing of the Au(111) substrate at 300 °C (20 min) induces a thermal cyclization/dehydrogenation sequence that converts *poly*-**1** into fully conjugated B-7AGNRs (Figure 3.2e). The apparent width and average height of the resulting GNRs are 1.6 nm and 0.16 ± 0.04 nm, respectively. Statistical analysis of large area STM images of densely packed ribbons shows that the majority of B-7AGNRs ranges in length between 4–12 nm with a few examples exceeding 16 nm (Figure 3.3). STM topography at negative bias reveals a characteristic stripe pattern corresponding to a height modulation (amplitude 0.14 ± 0.02 Å) along the length of the B-7AGNRs (Figure 3.2f). The periodicity of this topographic feature, 1.30 ± 0.05 nm, correlates with the expected spacing between boranthene units along the backbone of a B-7AGNR (Figure 3.2).
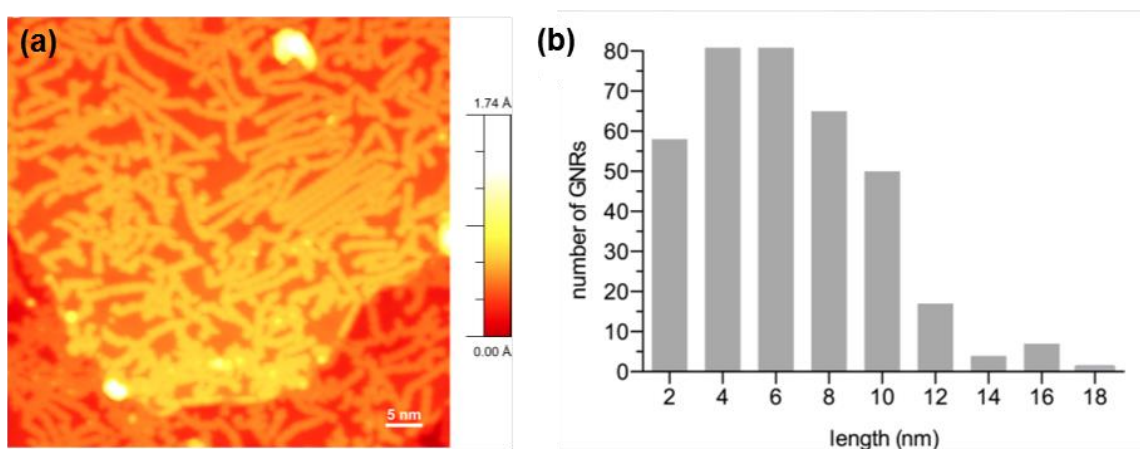
Figure 3.3: (a) Large area STM of B-7AGNRs on A(111) surface (V_s = 1.5 V, I_t = 5 pA, T = 4.5 K). (b) Statistical analysis of the length distribution of B-7AGNRs on Au(111).

3.4 DFT calculation for B-7AGNRs

First-principles calculations of boron-doped graphene nanoribbons were performed using DFT implemented in the Quantum Espresso package [90]. A supercell arrangement was used, with the cell dimension carefully tested to avoid interactions between the nanoribbon and its periodic image. We used norm conserving pseudopotentials [91], with a planewave energy cut-off of 60 Ry. The structure was fully relaxed until the force on each atom was smaller than 0.02 eV Å−1. All σ dangling bonds on the edge of the nanoribbon were capped by hydrogen atoms.

Quasiparticle band structure calculations were performed within the ab initio *GW* approach as implemented in the BerkeleyGW package [106]. Since the boron doped graphene nanoribbon was directly deposited on the gold surface, we used a common model in the literature to include the environment screening effects. Here we add to the intrinsic polarizability of the nanoribbon an environmental screening term in the form of:

$$\varepsilon_{environment} = \frac{1 + \varepsilon_{substrate}}{2}$$

This expression corresponds to the case of small separation between the nanoribbon plane and the gold or silver surface. Since the screening effects of noble metals at the static limit follow the Thomas-Fermi model of an electron gas, we employed a wave-number dependent dielectric function to describe the screening effects of metal substrate

$$\varepsilon_{substrate} = 1 + \frac{k_0^2}{q^2}$$

where the screening wave-vector is k_0 = 1.7 Å-1. The method described above has been used in much previous theoretical work in the graphene field. With this additional screening term in the dielectric polarizability matrix of the free standing boron doped graphene nanoribbon and within the COHSEX approximation of GW, the quasiparticle band gap between the valence band (VB) and the first conduction band (CB) is calculated to be 0.8 eV. Comparing this quasiparticle band gap with the LDA band gap of 0.5 eV, we obtain a self-energy correction of 0.3 eV. On the other hand, the quasiparticle band gap between the VB and the second conduction band (CB+1) is calculated to be 2.5 eV, which is 0.5 eV larger than the LDA band gap of 2.0 eV. Comparing the GW energy levels of CB and CB+1 with that of VB, the boron dopants have p-type character.

3.5 Band Gap Reduction of Graphene Nanoribbons on Metal Surfaces due to Boron Doping
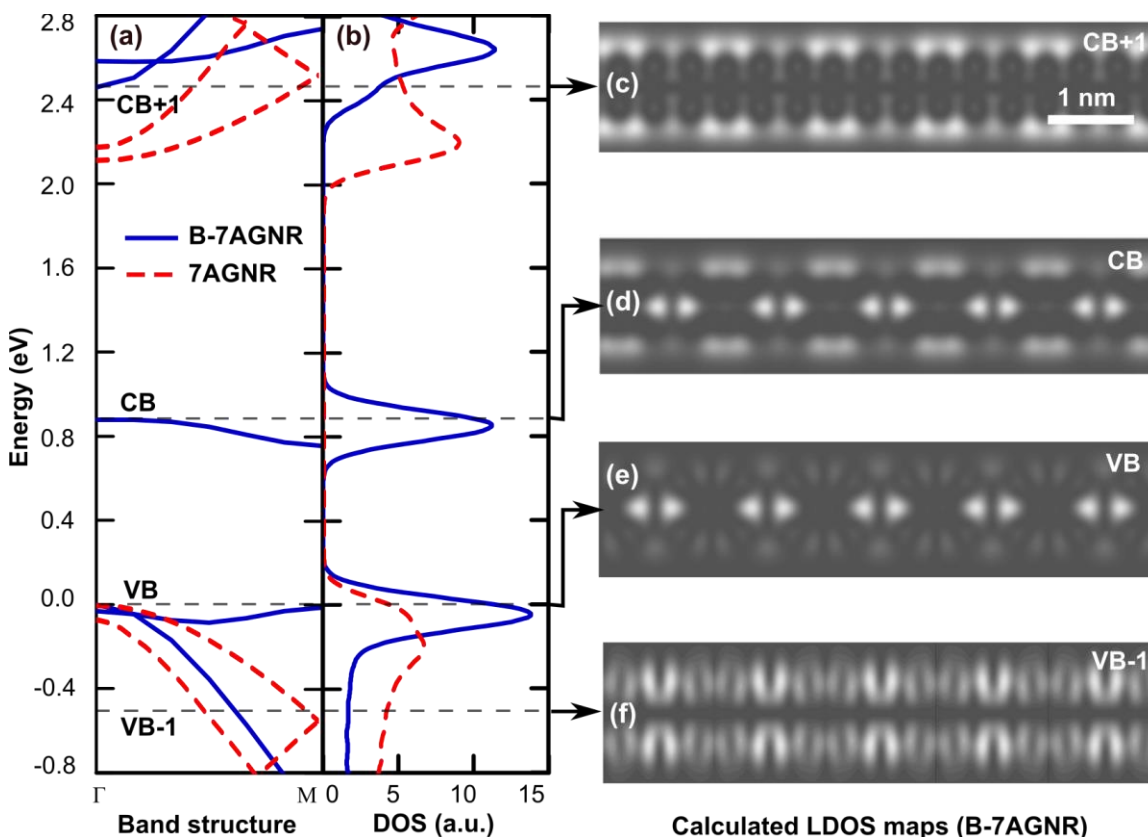
Figure 3.4: (a) Schematic representation of on-surface fabrication of B-7AGNRs on a metal surface. (b) STM topography of a B-7AGNR on Au(111) ($V = -1.0$ V, $I = 10$ pA, $T = 4.5$ K). (c) STM topographic image of a B-7AGNR on Ag(111) ($V = -1.0$ V, $I = 20$ pA, $T = 4.5$ K). (d) Constant-height nc-AFM image of a B-7AGNR on Au(111) with CO-functionalized tip.

Figure 3.4 shows the theoretical electronic structure predicted for an isolated B-7AGNR compared to an undoped N=7 AGNR (7AGNR) using *ab initio* DFT including the GW approximation. The screening effects of a metal substrate are incorporated into this calculation by adding an additional Thomas-Fermi screening term to the calculation. Boron doping along the backbone of the B-7AGNR is seen to induce a new, unoccupied band (the conduction band (CB)) and to also cause some flattening of other bands relative to an undoped 7AGNR (Figure 3.4a). The flattened bands can be seen as peaks in the GNR density of states (DOS) (Figure 3.4b). The energy difference between the center of the conduction band peak and the valence band peak leads to a theoretically predicted band gap of 0.9 eV for B-7AGNRs, significantly smaller than the 2.3 eV band gap

theoretically predicted for undoped 7AGNRs (dashed line). Figures 3.4c-f show the spatial distribution of the calculated local density of states (LDOS) 4 Å above the GNR surface at different band energies within the B-7AGNR electronic structure (i.e. wave function maps). At the highest energy shown, near the CB+1 band edge (Figure 3.4c), the electronic states is predicted to have high density near the B-7AGNR edges and low density in the interior. At lower energy in the conduction band (Figure 3.4d), however, the boron sites in the interior light up with high LDOS density while some diminished intensity remains near the edges. As we move further down in energy to the valence band edge (Figure 3.4e), the electronic density is predicted to be high at the boron sites and low elsewhere, qualitatively consistent with expectations for a highly localized flat band. At still lower energy (Figure 3.4f) the valence band is predicted to become more highly dispersive (labeled VB-1), causing the LDOS to shift away from the backbone to a more delocalized distribution near the GNR edges.
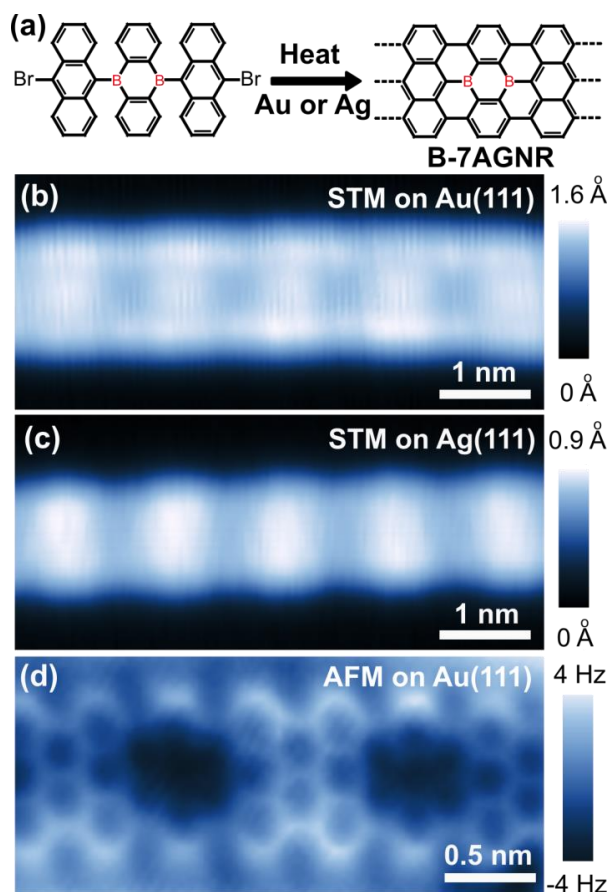
Figure 3.5: (a) Schematic representation of on-surface fabrication of B-7AGNRs on a metal surface. (b) STM topography of a B-7AGNR on Au(111) ($V = -1.0$ V, $I = 10$ pA, $T = 4.5$ K). (c) STM topographic image of a B-7AGNR on Ag(111) ($V = -1.0$ V, $I = 20$ pA, $T = 4.5$ K). (d) Constant-height nc-AFM image of a B-7AGNR on Au(111) with CO-functionalized tip.

In order to experimentally test these predictions we grew B-7AGNRs on both Au(111) and Ag(111) and explored them systematically using STM spectroscopy. B-7AGNRs on Au(111) were fabricated through on-surface thermal polymerization at 220°C followed by cyclodehydrogenation at 300°C (see sketch in Figure 3.5a) as described in previous publications [21,39]. A typical STM topographic image of a B-7AGNR on Au(111) is shown in Figure 3.5b, and exhibits a periodic superstructure of 1.3 nm [21,39]. The CO-tip nc-AFM image of Figure 3.5d shows that these stripes arise from the linked anthracene units between the boron sites, as reported previously in ref. [39]. B-7AGNRs were grown on Ag(111) using a similar recipe, but with a polymerization temperature of 150°C and a cyclodehydrogenation temperature of 300°C [107]. A typical STM image of a B-7AGNR on Ag(111) is shown in Figure 3.5c and exhibits a periodic superstructure that is essentially identical to the B-7AGNRs grown on Au(111). The typical apparent height and width of B-7AGNRs on Ag(111) is 0.10 ± 0.03 nm and 1.6 ± 0.2 nm.

We first characterized the local electronic structure of B-7AGNRs on Au(111) by performing dI/dV point spectroscopy at different points across the nanoribbons. Figure 3.6a shows typical dI/dV spectra measured at the backbone position (blue) and at the edge (red) of a B-7AGNR compared to a reference spectrum (dashed green) measured with the same STM tip placed above the bare Au(111) substrate (the Au(111) reference spectrum shows the onset of the surface state at about 0.5 V below the Fermi level). The dI/dV spectrum recorded at the edge of the B-7AGNR on Au(111) shows a well-defined peak at 1.63 ± 0.04 eV above the Fermi level (V = 0) (Kawai, et al. [39] also observed a spectroscopic feature at this energy). The spectrum recorded at the backbone of the B-7AGNR (blue) reveals a broad new peak at the lower energy of 1.0 ± 0.2 eV above E_F (this peak does not exist for undoped 7AGNRs). We were unable to observe any reproducible peaks below the Fermi level (E_F) in our dI/dV point spectra recorded on B-7AGNRs on Au(111) (this is in contrast to Kawai et al. [39] who observed a small shoulder in dI/dV at 0.8 eV below E_F which they identified as the B-7AGNR valence band edge). Comparing these spectroscopic peaks to the theoretical B-7AGNR DOS (Figure 3.4b), it is natural (based on the number and location of the peaks) to assign the peak at +1.0 eV to the B-7AGNR/Au(111) conduction band and the peak at +1.6 eV to the B-7AGNR/Au(111) CB+1 band.
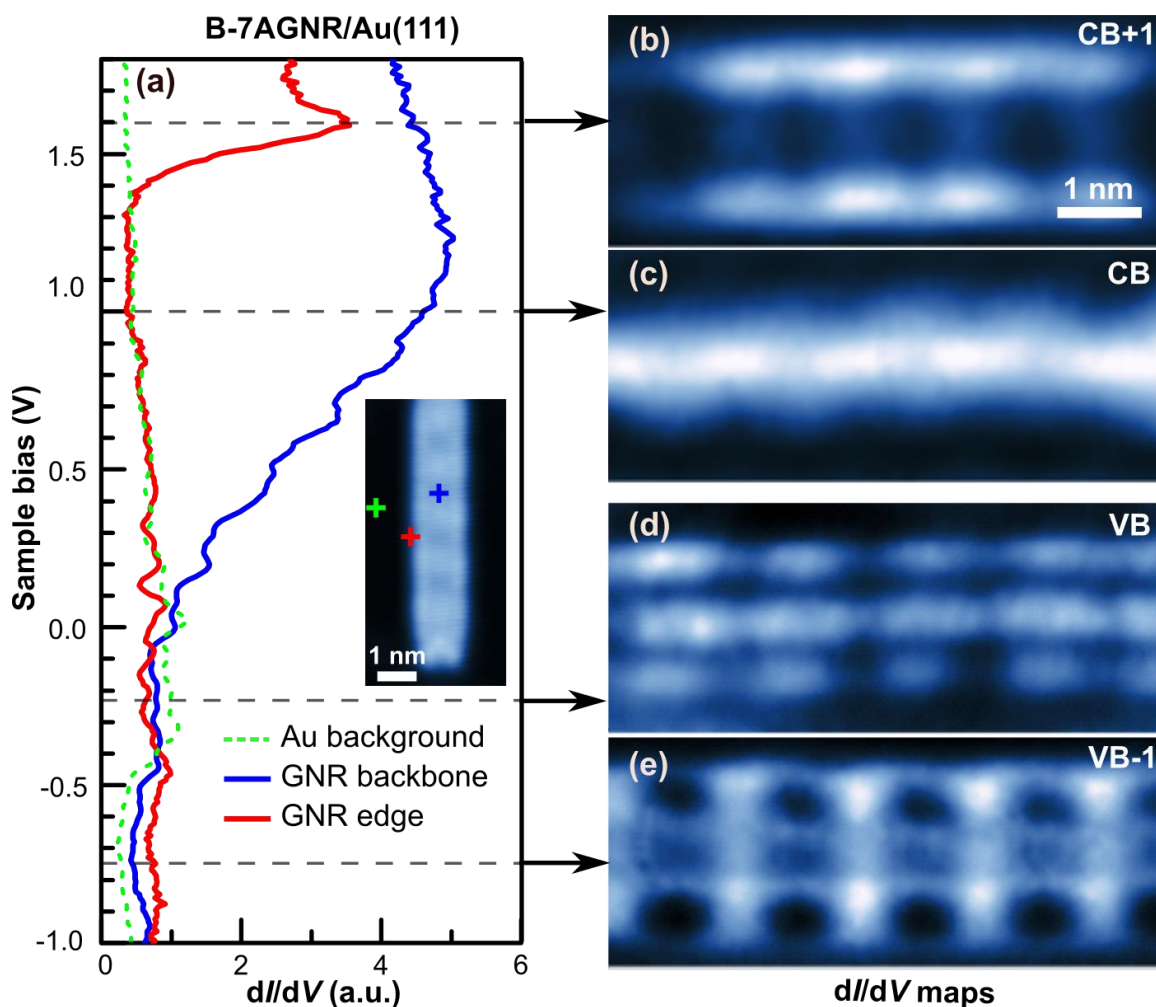
Figure 3.6: (a) dI/dV spectra at the edge (red) and the backbone (blue) of the B-7AGNR shown in the inset image compared to a reference spectrum (green dashed) obtained on bare Au(111) (f = 401 Hz, V_{ac} = 10 mV, T = 4.5 K). (b)-(e) Experimental dI/dV maps of a B-7AGNR on Au(111) at different bias voltages (f = 401 Hz, V_{ac} = 20 mV, T = 4.5 K).

The fact that we could not detect the B-7AGNR/Au(111) valence band via point spectroscopy suggests that the Au(111) surface state might be obscuring the B-7AGNR electronic structure. So, in order to obtain a clearer picture of intrinsic B-7AGNR electronic behavior we changed the substrate to Ag(111). Like Au(111), Ag(111) also has a Shockley surface state, but its band edge is 0.1 eV below E_F rather than 0.5 eV below E_F as seen for Au(111). Fig. 4a shows typical dI/dV spectra measured at the backbone (blue) and at the edge (red) of a B-7AGNR on Ag(111), as well as a reference spectrum (dashed green) measured with the same STM tip placed above the bare Ag(111) substrate. As expected, the bare Ag(111) reference spectrum shows the onset of the Shockley surface state at –0.1 eV with respect to E_F. The dI/dV spectrum recorded at the edge of

the B-7AGNR on Ag(111) shows two relatively broad peaks at 1.47 ± 0.02 eV and 1.09 ± 0.02 eV above E_F. These two peaks are at very similar locations compared to the two peaks seen for B-7AGNRs on Au(111). The dI/dV spectrum measured at the B-7AGNR/Ag(111) backbone has a local maximum 1.5 eV above E_F and a broad tail that extends all the way down to V=0. It is possible to fit this feature with two Lorentzian resonances at 1.5 eV and 1.1 eV. Comparing these spectroscopic peaks to the theoretical B-7AGNR DOS (Fig. 1b), it is natural to assign the peak at 1.1 eV to the B-7AGNR/Ag(111) conduction band and the peak at 1.5 eV to the B-7AGNR CB+1 band.

Below E_F we observe a significant difference in the dI/dV spectra for B-7AGNRs on Ag(111) compared to spectra for B-7AGNRs on Au(111) (Figure 3.7a). The dI/dV spectrum at the B-7AGNR/Ag(111) backbone shows a new peak at -0.3 V $\pm$ 0.1 eV relative to E_F that occurs below the onset of the Ag(111) surface state. This reproducible feature can be seen more clearly in the expanded scale of the inset (which has the same energy-axis as the main plot). An additional peak at even lower energy (-0.96 ± 0.02 eV) can also be seen in the spectrum recorded at the B-7AGNR/Ag(111) edge. Neither of these filled-state peaks are seen in the spectroscopic data for B-7AGNRs on Au(111) which is partially obscured by the lower-energy onset of the Au(111) surface state. Comparing these spectroscopic peaks to the theoretical B-7AGNR DOS (Figure 3.4b), it is natural to assign the peak at -0.3 eV to the B-7AGNR/Ag(111) valence band and the peak at -1.0 eV to the B-7AGNR/Ag(111) VB-1 band.
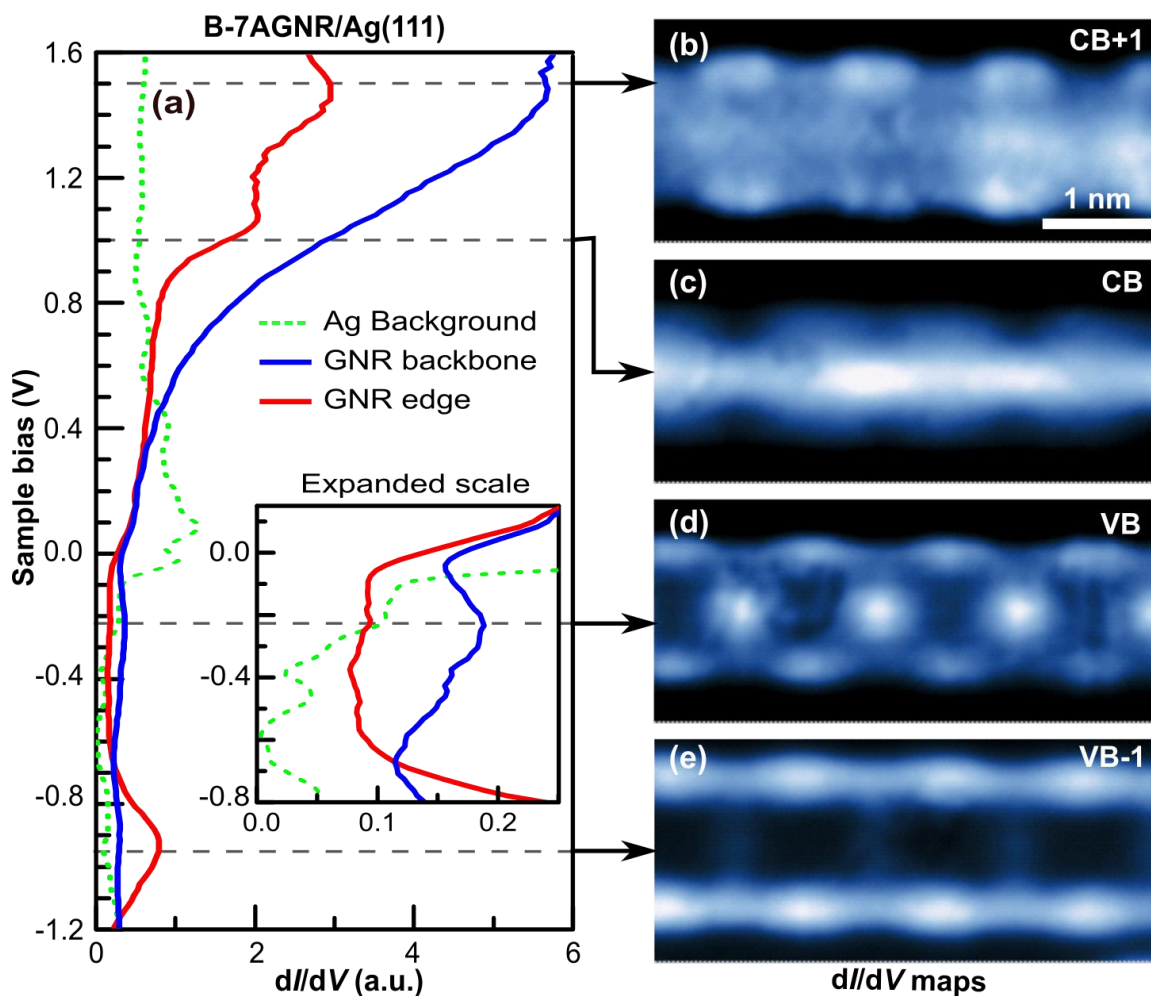
Figure 3.7: (a) dI/dV spectra at the edge (red) and the backbone (blue) of a B-7AGNR compared to a reference spectrum (green dashed) obtained on the bare Ag(111) surface (f = 401 Hz, V_{ac} = 10 mV). The inset shows a magnification of the VB peak. (b)-(e) Experimental dI/dV maps of a B-7AGNR on Ag(111) at different bias voltages (f = 401 Hz, V_{ac} = 20 mV, T = 4.5 K).

To further clarify the electronic structure origins of the four peaks observed in our dI/dV point spectroscopy for B-7AGNRs on Ag(111), we performed constant-current dI/dV maps at the four peak energies (dI/dV maps of B-7AGNRs/Ag(111) obtained at other energies can be seen in the Figure 3.8). These wave function maps provide experimental access to the energy-resolved spatial LDOS distribution of individual GNRs. The dI/dV map recorded at the highest-energy spectroscopic peak (1.5 eV above E_F) shows significant LDOS intensity at the B-7AGNR/Ag(111) edges, as well as some interior density (Fig. 4b). The dI/dV map near the peak at +1.1 eV (Figure 3.7c) exhibits an LDOS pattern that is much more intense along the B-7AGNR/Ag(111) backbone and

weaker at the edges compared to the higher-energy dI/dV map of Figure 3.7b. The LDOS pattern measured near the peak at −0.3 eV shows a much higher degree of localization along the backbone (Figure 3.7d), including bright regions at the sites of the boron atoms and some intensity at the GNR edges. The lowest energy spectroscopic peak at −1.0 eV exhibits an LDOS pattern that is highly localized at the B-7AGNR/Ag(111) edges and shows no intensity along the backbone.

| +1.6 V | +1.5 V | +1.4 V | +1.3 V | +1.0 V | +0.9 V | +0.5 V |

| −0.12 V | −0.22 V | −0.32 V | −0.42 V | −0.62 V | −0.95 V |
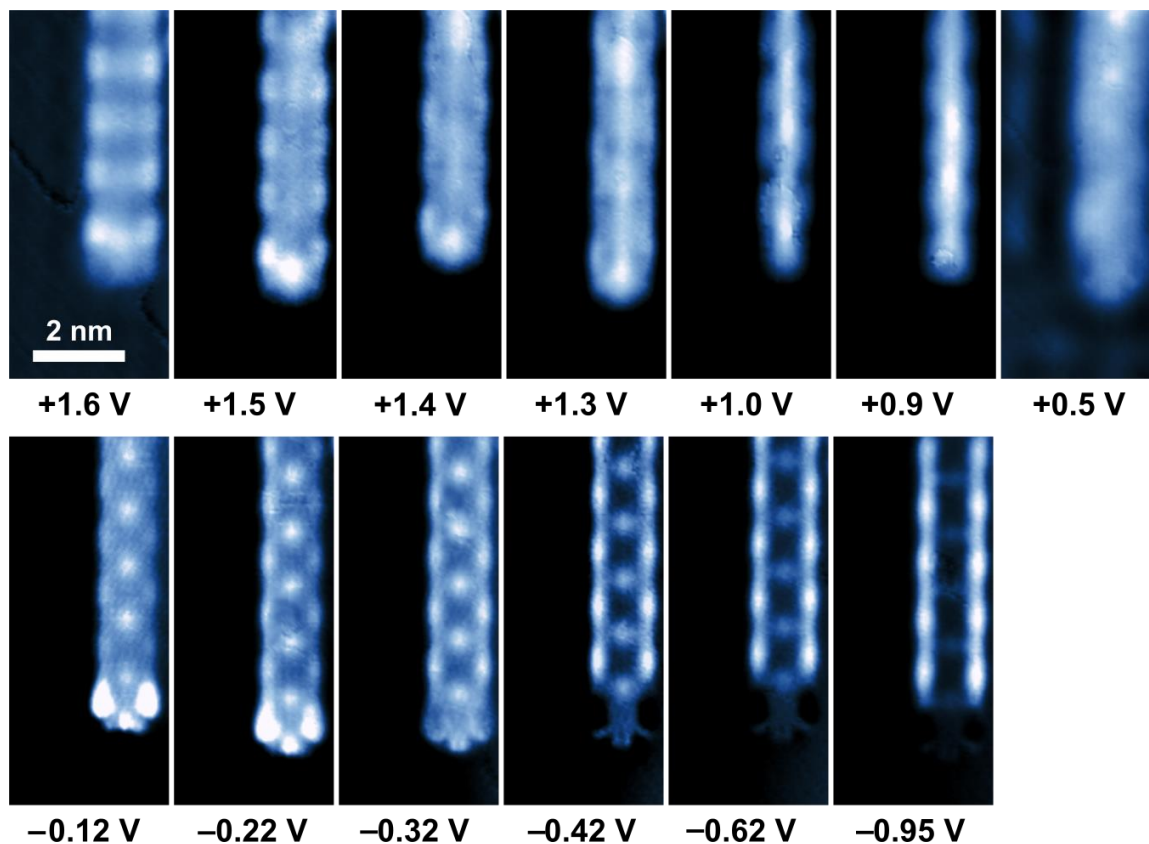
Figure 3.8: Constant current dI/dV maps of B-7AGNRs on Ag(111) at different bias (f = 401 Hz, V_{ac} = 20 mV, T = 4.5 K).

To interpret these experimental wave function maps we compare them to the theoretical LDOS maps calculated for an isolated B-7AGNR as shown in Figures 3.4c-f. We first compare the theoretical LDOS map for the CB+1 band (Figure 3.4c) to the B-7AGNR/Ag(111) experimental map obtained at the +1.5 eV peak (Figure 3.7b). Both maps show significant density at the GNR edges. Moving down in energy we next compare the theoretical LDOS map for the conduction band (Figure 3.4d) to the experimental map taken near the +1.1 eV peak (Figure 3.7c). Both the theoretical and experimental maps show a significant redistribution of LDOS from the GNR edge to the GNR backbone. This is a behavior that does not occur for undoped 7AGNRs which have no comparable spectroscopic feature along the backbone [89]. The results correlation

between experiment and theory here provides further evidence supporting our assignment of the experimental peak at +1.1 eV as the B-7AGNR/Ag(111) conduction band and the experimental peak at +1.5 eV as the B-7AGNR/Ag(111) CB+1 band.

We next compare the B-7AGNR/Ag(111) dI/dV map taken near the –0.3 eV spectroscopic peak (Figure 3.7d) to the theoretical valence band LDOS map of Figure 3.4e. Both maps show significant LDOS intensity along the GNR backbone and, compared to the conduction band LDOS, both maps also exhibit increased localization of the LDOS. As energy is reduced even further below the valence band edge, the theoretical LDOS map (Figure 3.4f) changes significantly compared to the valence band LDOS map in that the LDOS completely shifts from the B-7AGNR backbone (Figure 3.4e) to the B-7AGNR edge (Figure 3.4f). This is precisely the same trend that we observe experimentally in the dI/dV map obtained at the lowest spectroscopic peak energy of –1.0 eV (Figure 3.7e) where the experimental LDOS has shifted from the GNR backbone (Figure 3.7d) to the GNR edges (Figure 3.7e). These results provide further evidence supporting our assignment of the experimental peak at –0.3 eV to the B-7AGNR/Ag(111) valence band and the experimental peak at –1.0 eV to the B-7AGNR/Ag(111) VB-1 band. The difference in energy between the resulting B-7AGNR/Ag(111) conduction band peak (+1.1 eV) and the B-7AGNR/Ag(111) valence band peak (-0.3 eV) yields an experimental band gap of 1.4 ± 0.1 eV for B-7AGNRs on Ag(111), significantly less than the 2.5 eV experimental band gap observed for pristine N=7 AGNRs on the surface of gold [17] and much closer to the theoretically predicted B-7AGNR band gap of 0.9 eV [36].This confirms that incorporation of boron atoms into the backbone of N=7 AGNRs induces a new band (the conduction band) in the B-7AGNR electronic structure, resulting in a greatly reduced band gap.

Comparison of the B-7AGNR/Au(111) valence band structure to theoretical predictions is hampered by the lack of peaks in the filled-state point spectroscopy. However, it is useful to notice that there is a clear transition from one distinct experimental LDOS pattern to another as energy is lowered down into the filled-state regime (e.g. from Figure 3.6c to Figure 3.6d). The new LDOS pattern in Figure 3.6d exhibits more highly localized features compared to Figure 3.6c and has similarities to the LDOS pattern seen for B-7AGNRs on Ag(111) as energy is decreased from the conduction band (Figure 3.7c) down to the valence band (Figure 3.7d). This experimental LDOS trend is similar to the theoretical LDOS trend from conduction to valence band (Figure 3.4d to Figure 3.4e) in that it exhibits density along the GNR backbone as well as a higher degree of localization (some disagreement occur here also in that the experimental dI/dV map (Figure 3.6d) has more density at the GNR edges than is seen theoretically (Figure 3.4e)). As energy is lowered even further in the experiment we observe another transition to a new experimental LDOS pattern where density reduces along the GNR backbone and increases along the GNR edges (Figure 3.6e). This experimental transition is similar to the theoretical transition observed as energy is reduced from the valence band to the VB-1 band (Figure 3.4e to Figure 3.4f), as well as

what is seen experimentally for B-7AGNRs on Ag(111) (Figure 3.7d to Figure 3.7e). The correlation between experiment and theory that is seen here (as well as the similarity to the behavior of B-7AGNRs on Ag(111)) allows us to conclude that the B-7AGNR/Au(111) LDOS pattern of Figure 3.6d arises from the B-7AGNR valence band while the B-7AGNR/Au(111) LDOS pattern of Figure 3.6e arises from the B-7AGNR VB-1 band. Determining precise band edges here is difficult because the experimental transition from one LDOS pattern to another is continuous. However, if we mark the band energy as the center energy between LDOS pattern transitions (see Figure 3.9) then we arrive at an experimental VB energy for B-7AGNRs/Au(111) of –0.30 ± 0.25 eV and an experimental VB-1 energy for B-7AGNRs/Au(111) of –0.75 ± 0.40 eV. This leads to a band gap of 1.3 ± 0.3 eV for B-7AGNRs on Au(111), very similar to the band gap determined for B-7AGNRs on Ag(111) (1.4 ± 0.1 eV).
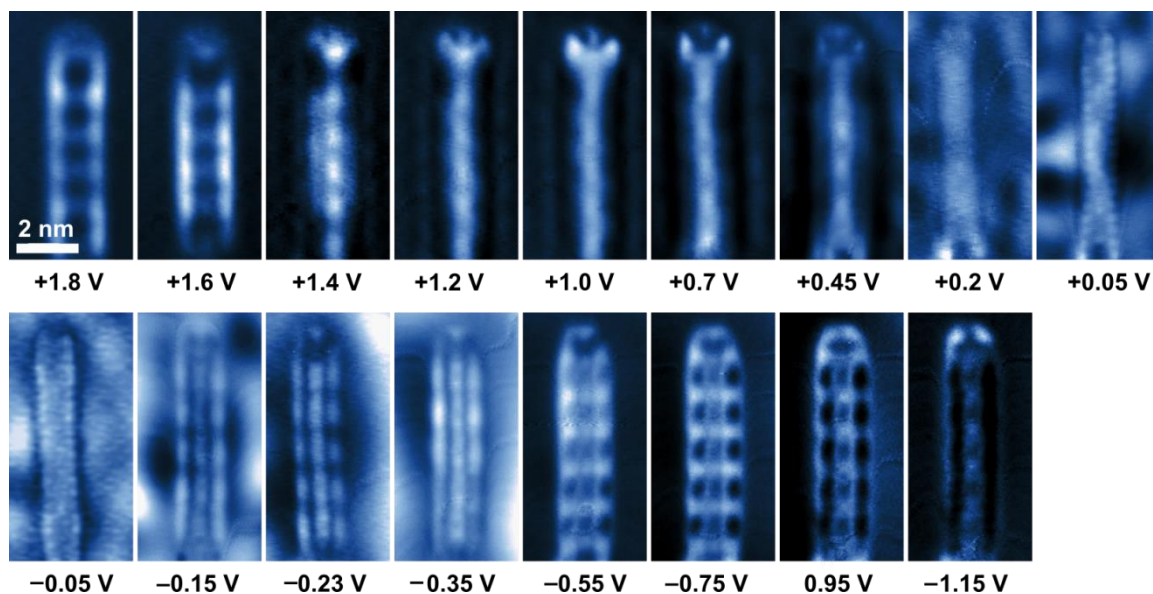
Figure 3.9: Constant current dI/dV maps of a B-7AGNRs on Au(111) at different bias (f = 401 Hz, Vac = 20 mV, T = 4.5 K).

Although there is significant agreement between our experimental results and the theoretical predictions for isolated B-7AGNRs (e.g., the number and order of bands, reduction in the energy gap, and the LDOS maps), there also remain some discrepancies. Examples of discrepancies are the significant energy broadening of the conduction band, the difficulty in observing valence band features for B-7AGNRs on Au(111) via point spectroscopy, and the presence of LDOS intensity at the GNR edges for states at the B-7AGNR valence band edge on both surfaces. A likely explanation for these discrepancies is the interaction of the B-7AGNRs with the metal substrate. As seen in Figure 3.5d (and also noted previously in ref. [39]), the depressions seen in high resolution nc-AFM images of B-7AGNRs at the boron atom sites suggest that the boron interacts strongly with the metal surface. This would explain the broadening of the conduction band and

might also lead to mixing between bands (thus causing the observed deviation between experimental LDOS plots and isolated B-7AGNR theoretical LDOS maps). The difficulty in seeing B-7AGNR/Au(111) valence band features in point spectroscopy likely comes from interaction between the B-7AGNR states and the Au(111) Shockley surface state, which is very prominent in the valence band energy range (i.e., near -0.3 eV). This explains our success in observing the B-7AGNR/Ag(111) valence band via point spectroscopy, since the Ag(111) surface state band edge is higher in energy (–0.1 eV) thus causing the Ag(111) surface state to not strongly hybridize with B-7AGNR/Ag(111) valence band.

2.4 Summary

In conclusion, we have characterized the electronic structure of B-7AGNRs grown on Au(111) and Ag(111) substrates using scanned probe microscopy and DFT simulations. By comparing the local electronic behavior of B-7AGNRs on these two surfaces we have determined that incorporation of boron atoms into the 7AGNR backbone leads to the formation of a new unoccupied band of states. Because this band lies where the energy gap would be for undoped 7AGNRs, the energy gap for B-7AGNRs (1.4 eV) is considerably reduced compared to the undoped 7AGNR gap (2.5 eV) as measured by STM spectroscopy. Our observed energy gap reduction, as well as the observed spatial distribution of the different band states, are qualitatively consistent with DFT-GW theoretical predictions for isolated B-7AGNRs. Some discrepancies do exist, however, likely arising from the interaction of B-7AGNRs with noble metal substrate atoms, which was not taken into account by the theoretical model. These results confirm that it is possible to dramatically alter the electronic structure of bottom-up-synthesized GNRs (including the number of bands and the band gap) by doping them with Group III elements.

Chapter 4 : Bottom-up synthesis of ketone doped graphene nanoribbons

In this chapter we report the fabrication and STM characterization of atomically-precise ketone edge-doped chevron graphene nanoribbons (ketone GNRs) on a Au(111) surface. Scanning tunneling spectroscopy (STS) and first principle calculations reveal modification of the electronic structure of ketone GNRs when compared to pristine chevron GNRs. The electronic structure of partially cyclized ketone GNRs is also resolved. At lower annealing temperatures, heterojunctions formed by partially and fully cyclized GNRs are characterized by STM spectroscopic measurements.

This chapter is adapted from a prepared manuscript titled "Atomic Fabrication of Graphene Heterojunctions". The coauthors are Giang D. Nguyen, Hsin-Zon Tai, Arash A. Omrani, Griffin F. Rodgers, Daniel J. Rizzo, Meng Wu, Tomas Marangoni, Ryan R. Cloke, Yuki Sakai, James Chelikowsky, Steven G. Louie, Felix R. Fischer and Michael F. Crommie.

4.1 Introduction
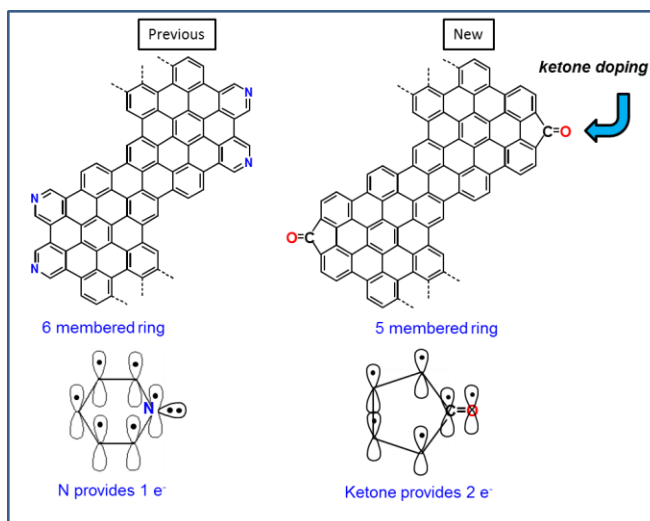
Figure 4.1: Schematic of doping chevron GNRs with ketone functional group. The ketone doping provides 2 electrons into the GNR extended π-system, unlike previous nitrogen doping which only provides 1 electron.

Bottom-up fabrication allows modification of GNRs through the introduction of dopant atoms at the GNR edges. This type of modification is a very intriguing approach since functionalization at the edge (rather than in the interior of GNRs) permits

integration of a wider range of dopant species. Thus far, controlled edge doping has only successfully used nitrogen in the form of pyridine and pyrimidine rings incorporated along chevron GNRs [19,38,40,41] and in our recent work using sulfur along the edge of N=13 AGNRs [37]. However, these dopants do not change the GNR band gap.

In this chapter, we report the bottom-up synthesis and characterization of atomically-precise ketone edge-doped chevron graphene nanoribbons (ketone GNRs) wherein ketone C=O groups decorate the GNR edges. In this configuration, the ketone groups will contribute two electrons into the π-system, as opposed to the previous studies of nitrogen doped chevron GNRs that contribute one electron (Figure 4.1) [19,38,40,41]. Consequently, we expect the band gap of these ketone doped chevron GNRs will be reduced in comparison with pristine chevron GNRs, and this is confirmed by both theoretical density functional theory (DFT) calculations and scanning tunneling spectroscopy (STS).

4.2 Bottom-up growth of ketone GNRs

The molecular precursors for ketone GNRs synthesized by Fischer's group are shown in Figure 4.2. These molecular precursors were evaporated from a home-built Knudsen cell evaporator and the deposition rate was calibrated in a test chamber using a quartz crystal microbalance. The sublimation temperature is 420 K onto a Au(111) substrate held at room temperature under ultra-high vacuum for about 5 minutes to obtain 30–70 % coverage.
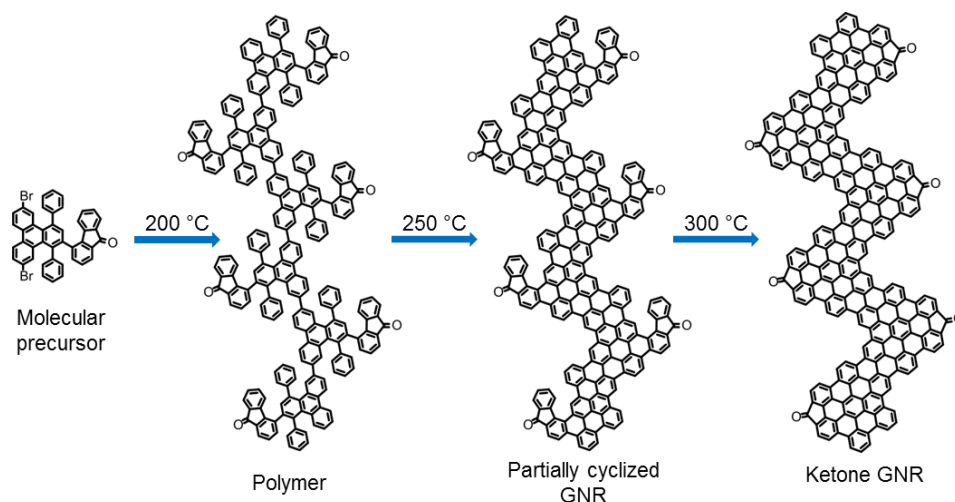
Figure 4.2: Schematic of bottom-up fabrication of ketone doped chevron GNRs.

After deposition, the sample was cooled down to 4.5 K in the STM chamber. The molecular coverage was checked with STM survey scans in several regions of the sample. Figure 4.3 shows a typical STM image of molecular precursors as deposited on

Au(111). The molecules tend to aggregate into irregular chains on the surface with an average height of 0.5 nm.
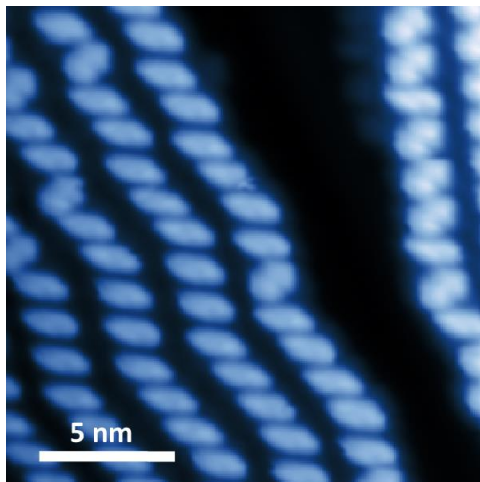
Figure 4.3: STM topographic image of molecular precursors on Au(111) after deposition (V_s = 0.5 V, I_t = 3 pA, T = 4.5 K).

Annealing the molecule-decorated sample at 200 °C for 1 hour induces homolytic cleavage of the labile C–Br bonds in monomers followed by radical step-growth polymerization of the intermediate diradical to give polymers (see in Figure 4.4).
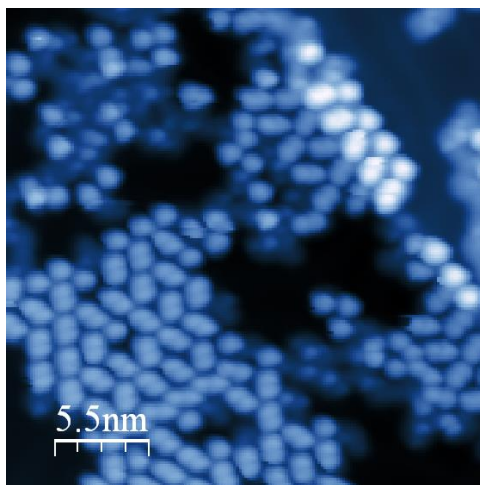
Figure 4.4: STM topographic images of the polymer state of ketone GNRs on Au(111) (V_s = 2 V, I_t = 5 pA, T = 4.5 K).

Further annealing of Au(111) samples at 250 °C for 30 minutes induces a thermal cyclodehydrogenation along the backbone of polymers, which converts the polymers into partially cyclized GNRs. Figure 4.5a shows a typical STM image of partially cyclized

GNRs. The ribbons appear to have a bright spots at the edge. By performing chemical bond resolved STM (BRSTM) imaging, we can recognize the structure of these partially cyclized ketone GNRs as seen in Figure 4.5b. These bright spots correspond to the ketone wings that have not cyclized to form fully conjugated ketone GNRs. The proposed chemical structure of a partially cyclized GNR can be seen in Figure 4.5c.
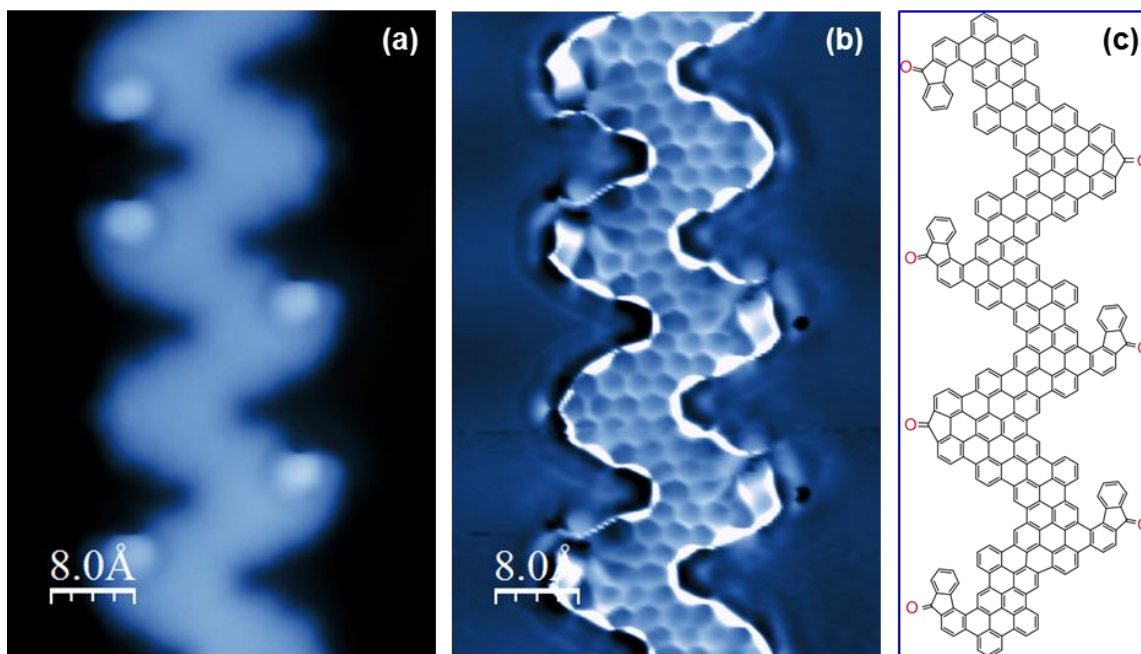
Figure 4.5: (a) STM image at high bias of partially cyclized ketone GNR on Au(111) (V_s = 1.4 V, I_t = 5 pA, T = 4.5 K). (b) Bond resolved STM (BRSTM) image of the same partially cyclized ketone GNR on Au(111) using a CO-functionalized tip (V_s = 40 mV, I_t = 10 pA, V_{ac} = 20 mV, f = 401 Hz, T = 4.5 K). (c) Proposed chemical structure of the partially cyclized ketone GNR in (a)&(b).

A third annealing step (300 °C) induces a full thermal cyclodehydrogenation to yield fully conjugated ketone GNRs. A typical image of fully cyclized ketone GNRs is shown in Figure 4.6. Scanning at the same bias of 1.6 V, the STM images after annealing at higher temperature show much fewer bright spots near the edges of the ribbons, indicating fewer partially cyclized GNRs. The ribbons are shown to be flat with the typical height of 0.18 nm (Figure 4.6).
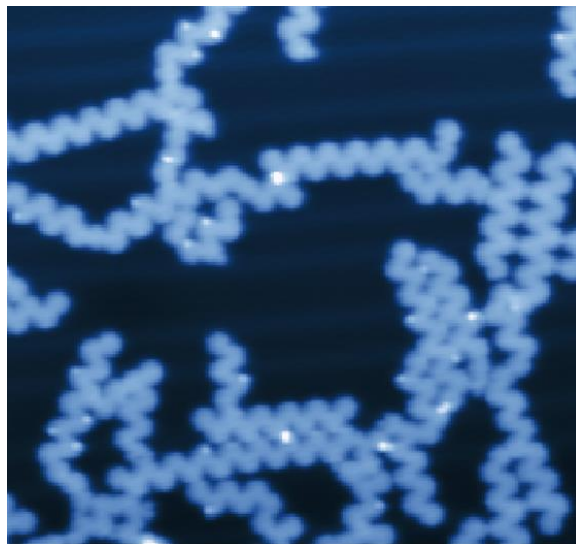
Figure 4.6: STM topographic image showing fully cyclized ketone GNRs on Au(111) (V_s = 1.6 V, I_t = 5 pA, T = 4.5 K)

At high coverage, the ketone GNRs prefer to aggregate to form an aligned, parallel assembly as shown in Figure 4.7. There are adsorbates in between these aligned ketone GNRs or sticking to the ketone functional groups of the GNRs. These adsorbates could be Au adatoms or other possible contamination in the sample preparation chamber of our STM system. It is possible to remove the adsorbates by applying a tip pulse of 3 V with a width of 300 ms (Figure 4.8).
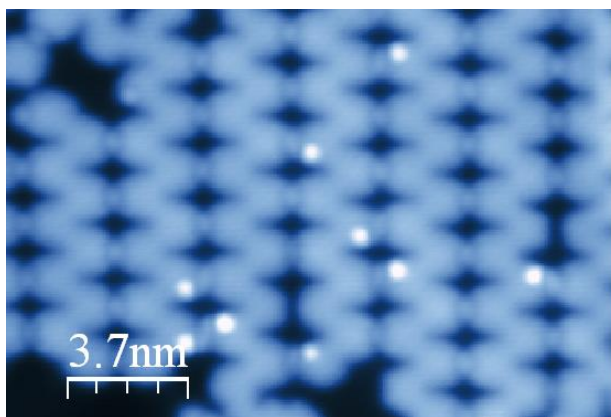
Figure 4.7: STM topographic image of self-assembled ketone GNRs on Au(111) (V_s= 1.4 V, I=5 pA, T = 4.5 K).

Figure 4.8: Adsorbate removal using a tip pulse of V_s = 3 V, width 500 ms. The tip-sample distance is defined by the set point parameters of bias voltage at 50 mV and a tunneling current of 5 pA.

4.3 STM spectroscopic measurement

The local electronic structure of partially cyclized ketone GNRs on Au(111) was characterized by STS measurements with a CO-functionalized tip. Figure 4.9a shows a typical STM dI/dV spectra at various positions on a partially cyclized ketone GNR compared with a reference spectrum on Au(111) (positions shown in the inset image). The dI/dV spectrum on the ketone position, called the outer edge (red), clearly shows one peak at energy -1.17 ± 0.03 eV in the occupied states and two peaks with energies 1.60 ± 0.02 eV and 2.0 ± 0.02 eV in the unoccupied states. The dI/dV spectrum recorded at the inner edge (blue) shows a stronger peak in the occupied states with energy of -1.1 ± 0.03 eV. The spatial distrubution of the local density of states (LDOS) of these three peaks is revealved by performing constant current dI/dV maps (Figure 4.9b-d).
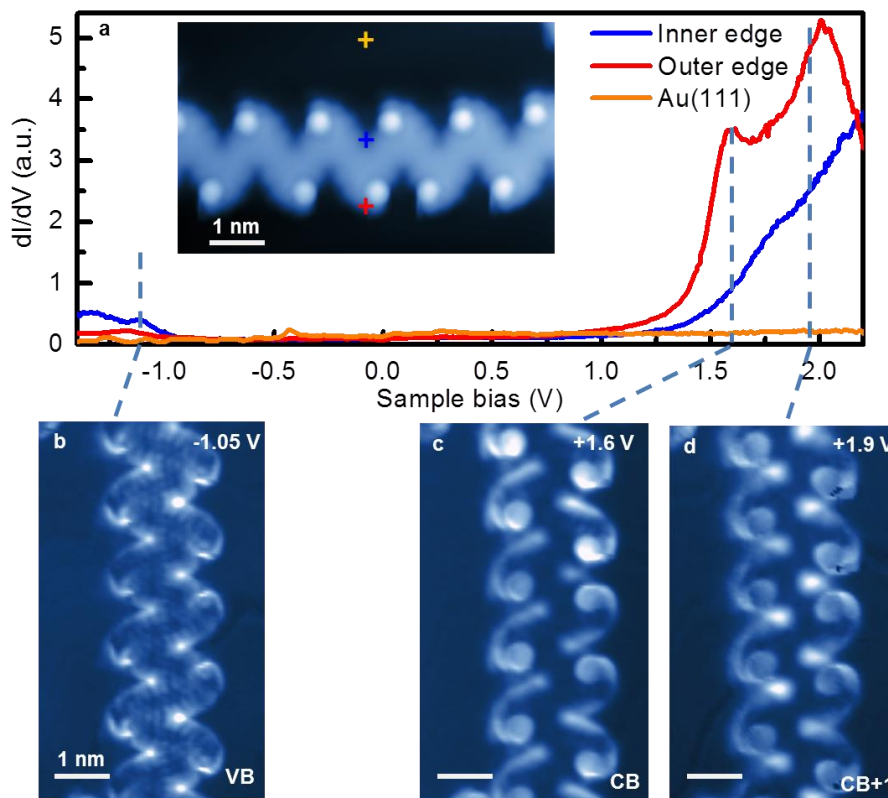
Figure 4.9: (a) STM dI/dV spectroscopic measurements on a partially cyclized ketone GNR taken at different positions and compared to the reference spectrum obtained on bare Au(111) (V_{ac} = 10 mV, f = 401 Hz, T = 4.5 K). Crosses in the topographic STM image (inset) indicate the positions of recorded spectra. (b)-(d), dI/dV spatial maps at the valence band (VB), conduction band (CB) and CB+1 peaks of a partially cyclized ketone GNR (V_{ac} = 20 mV, f = 401 Hz, T = 4.5 K).

The local electronic structure of fully cyclized ketone GNRs on Au(111) was characterized by STS measurements with a CO-functionalized tip and compared to density functional theory (DFT) calculations. Figure 4.10a shows a typical STM dI/dV spectra at various positions on a ketone GNR compared with a reference spectrum on Au(111) (positions shown in the inset image). The dI/dV spectrum recorded at the edge of the ketone GNRs shows two clear peaks at the energies 1.37 ± 0.03 eV (in the unoccupied states) and –0.96 ± 0.01 eV (in the occupied states). The spatial distribution of the LDOS of these two peaks is revealed by performing constant current dI/dV maps (Figure 4.10b,c). There is very good agreement between these dI/dV maps (Figure 4.10b,c) and the calculated LDOS maps of the CB and VB for ketone GNRs (Figure 4.10c,f). Therefore, we can assign the peaks at 1.37 ± 0.03 eV and –0.96 ± 0.01 eV as the CB and VB energies, respectively, of the ketone GNRs. Consequently, the band gap of ketone GNRs is 2.33 ± 0.03 eV.
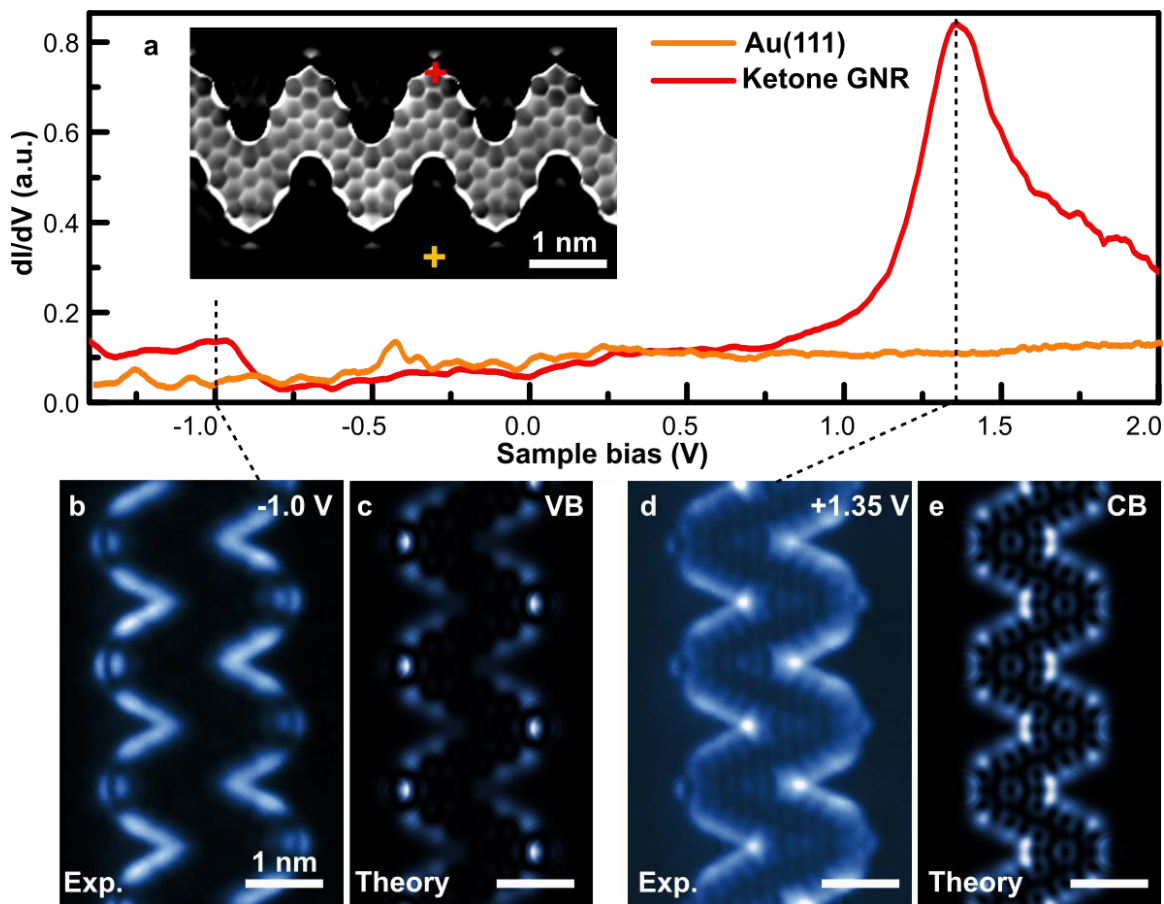
Figure 4.10: (a), STM dI/dV spectroscopic measurement of a ketone GNR (V_{ac} = 10 mV, f = 401 Hz, T = 4.5 K). (b),(d) Experimental dI/dV maps of the VB and CB of a ketone GNR (V_{ac} = 20 mV, f = 401 Hz, T = 4.5 K). (c),(d), Theoretical LDOS maps of the VB and CB of a ketone GNR.

In order to compare the electronic structure of these ketone GNRs with pristine GNRs, we performed similar measurements on pristine GNRs using the same instrument (Figure 4.11). With more accurate electronic measurements than those available in literature [19], we could compare the band gap of ketone GNRs with that of the pristine GNRs in a reliable way. An average of 38 spectra taken on 18 different pristine GNRs on Au(111) yield a band gap of 2.51 ± 0.05 eV, which indicates the ketone functionalization reduces the band gap of the GNRs by 0.19 ± 0.06 eV. This behavior is very different from previous studies of sulfur or nitrogen edge-doped GNRs, which showed no change in band gap [19,37,38]. Moreover, both the CB and VB in ketone GNRs have shifted to lower energies compared with the CB and VB of pristine GNRs. This can be explained by the higher electronegativity of the oxygen atom in the ketone functional group compared that of the carbon atoms [37]. These observations are consistent with DFT calculations for free standing pristine and ketone GNRs (Figure 4.12). At the DFT-LDA level, the

band gap of ketone GNRs is reduced by 0.21 eV compared to pristine GNRs and both CB and VB undergo a downward shift in energy.
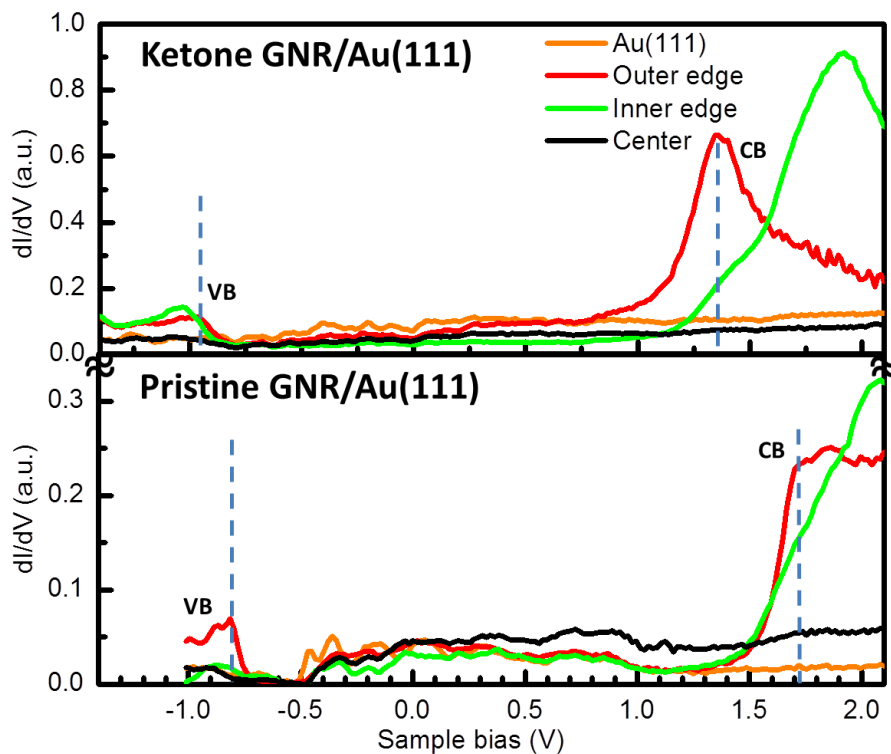
Figure 4.11: Comparison of the STM dI/dV spectroscopic measurement of ketone GNRs on Au(111) and pristine GNRs on Au(111) at different positions (V_{ac} = 10 mV, f = 401 Hz, T = 4.5 K). The orange line indicates the reference spectrum obtained on bare Au(111).
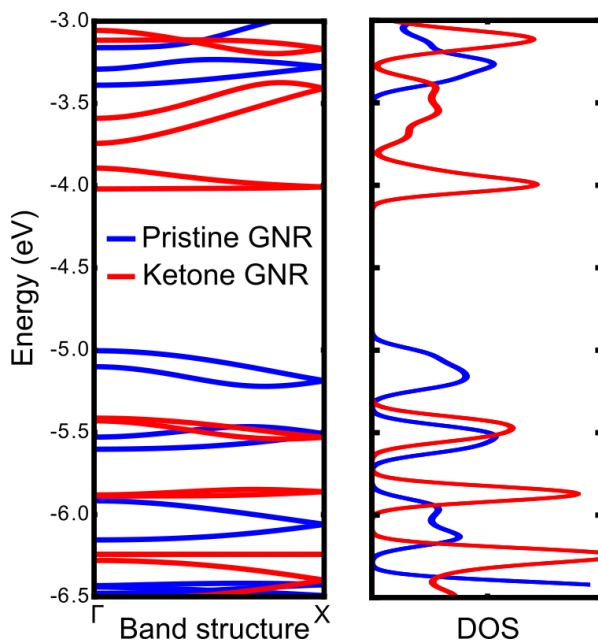
Figure 4.12: Comparison of the band structures and DOS of pristine GNR (blue) and ketone GNR (red). For both, the bands are aligned to vacuum potential.

4.5 Summary

In conclusion, we have demonstrated synthesis of atomically precise ketone GNRs with ketone groups incorporated along the outer edges of chevron GNRs. Both experimental STM measurements and first principle calculations show a band gap reduction for ketone GNRs compared with pristine GNRs. Moreover, both the CB and VB in ketone GNRs are shifted to lower energies compared to the CB and VB in pristine GNRs. This creates potential for forming a type II heterojunctions between ketone and pristine GNRs, which will be shown in the next chapter.

Chapter 5 : Atomic fabrication of graphene nanoribbon heterojunctions

In this chapter, we report the fabrication and nanoscale characterization of atomically-precise graphene nanoribbon heterojunctions on a Au(111) surface. Scanning tunneling spectroscopy and first principle calculations reveal modification of the electronic structure of the junctions when compared to pristine chevron GNRs.

This chapter is adapted from a prepared manuscript titled "Atomic Fabrication of Graphene Heterojunctions". The coauthors are Giang D. Nguyen, Hsinzon Tai, Arash Omrani, Griffin F. Rodgers, Daniel J. Rizzo, Meng Wu, Tomas Marangoni, Ryan R. Cloke, Yuki Sakai, James Chelikowsky, Steven G. Louie, Felix R. Fischer and Michael F. Crommie.

5.1 Introduction

Graphene nanoribbons (GNRs) have attracted great interest due to their fundamental properties as well as their potential in industrial applications. Their tunable electronic structure makes them a useful material for applications in molecular electronic devices. Discovered in 2010, bottom-up synthesized GNRs provides a flexible way to fabricate GNRs [16]. There are a number of different molecular precursors used to synthesize ribbons, and by combining precursors, previous studies have successfully fabricated graphene heterojunctions (7-13 heterojunction [20] and p-n chevron heterojunction [19]). However, this method lacks control over the fabrication of heterojunctions due to random statistical processes of self-assembly of the two precursor monomers.

In this chapter, we report the fabrication of controlled GNR heterojunctions using only a single molecular precursor. This precursor with a ketone functional group is used to grow ketone functionalized GNRs on a Au(111) surface. The ketone functional groups can be removed by annealing or potentially by atomic manipulation using a tip pulse to form a pristine GNR segment. We demonstrate the successful fabrication of an atomically sharp type II ketone-pristine GNR heterojunction with a band gap engineered by the ketone groups. The structure of the junction is discovered by bond-resolved STM (BRSTM) and confirmed by theoretical simulation. The electronic properties of these heterojunctions are characterized by scanning tunneling spectroscopy (STS) and compared with density functional theory (DFT) calculations.

5.2 Ketone-pristine GNR heterojunction
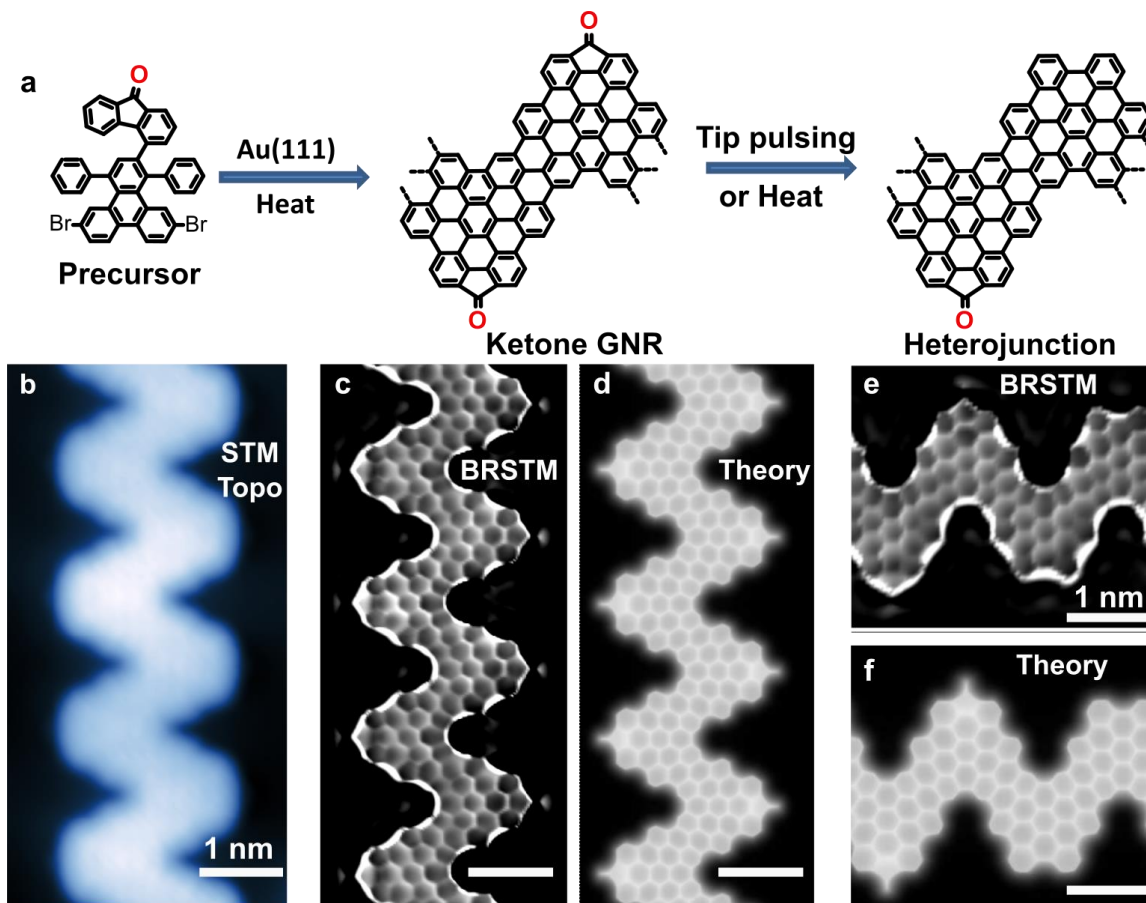
Figure 5.1: (a), Reaction scheme for the synthesis of ketone GNRs and heterojunctions. (b), Typical STM topographic image with a CO-functionalized tip of a ketone GNR ($V_s = -1.0$ V, $I_t = 10$ pA). (c),(e), BRSTM images of a ketone GNR and a ketone-pristine heterojunction ($V_s = 40$ mV, $I_t = 10$ pA, $V_{ac} = 20$ mV, $f = 401$ Hz). (d),(f), Simulated BRSTM images of (c) and (e).

Ketone GNRs were fabricated on Au(111) from molecular precursors (Figure 5.1a) by a standard thermally grown process of thermal polymerization at 200°C followed by cyclodehydrogenation at 300°C. A typical STM topographic image using a CO-functionalized tip of a ketone GNR is shown in Figure 5.1b. The ketone functional groups are not easily visualized in the standard STM images of the ketone GNRs, making their appearance very similar to other types of chevron GNRs. However, the bond-resolved STM (BRSTM) image in Figure 5.1c can resolve the pentagon structure and the ketone group on the outer edges of the ketone GNRs, allowing us to determine the chemical structure of these ketone GNRs. The faint circular sectors near the pentagon structure at the edge of the GNR are the ketone groups. This image is obtained taking a

constant current dI/dV map of the ketone GNRs at very low bias (40 mV) with a CO-functionalized tip. Figure 5.1d shows the simulated BRSTM image which takes into account a lateral relaxation of the probe atom (oxygen) on the CO tip while scanning across the ketone GNRs [75]. Based on structured optimization from DFT calculations, the CC bond length in pentagonal rings is 1.52 Å, while the CC bond length in hexagonal rings is 1.38 Å. As a result, we expect weaker bond strength for the CC bonds connecting the ketone group to GNR in comparison with the CC bonds of the conjugated hexagonal structure of the GNRs (since longer bonds tend to be weaker [76]). This suggests the possibility of selectively removing ketone groups from the ketone GNRs in order to form a ketone-pristine GNR heterojunction. In our study, we were able to remove the ketone groups by annealing the sample to a higher temperature (above 350 °C) after the formation of ketone GNRs. Second suggested method is to use STM tip pulses near the ketone groups to remove the ketone groups. Figure 5.1e shows a BRSTM image of a segment of a ketone-pristine heterojunction formed through thermal processes. The image clearly shows two ketone groups removed from the ribbon via annealing on the right to form a pristine GNR segment. A simulated BRSTM image of this heterostructure is shown in Figure 5.1f, confirming the molecular structure.

The experimental electronic structure of a ketone-pristine heterojunction is shown in Figure 5.2. Figure 5.2a presents a ketone-pristine heterojunction created by thermally annealing the sample at 350 °C for 1 hour. The red dashed circles on the BRSTM image in Figure 5.2a indicate the positions of the ketone groups. The STM dI/dV point spectrum at these ketone positions (plotted in red) shows that the peak positions of the VB and CB are consistent with those of the pure ketone GNRs (Figure 4.10a). Similarly, the dI/dV spectrum at the pristine positions where ketone groups were removed (plotted in green) shows peak positions of the VB and CB that are consistent with those of the pristine GNRs (Figure 4.11). Both spectra show a peak at the energy of about –0.3 V below the Fermi level, which is also seen in the reference spectrum (orange) taken on bare Au(111). Thus, we can assign this peak as a background peak due to the Au(111) surface state. Comparing the energy alignment between the VB and CB on different segments of a ketone-pristine heterojunction are able to determine that it is a type II heterojunction. Using a Gaussian fit, the positions of the VB (peak 1) and CB (peak 2) of the ketone-pristine heterojunction are at the energy of –0.85 ± 0.02 eV and 1.39 ± 0.02 eV, respectively.
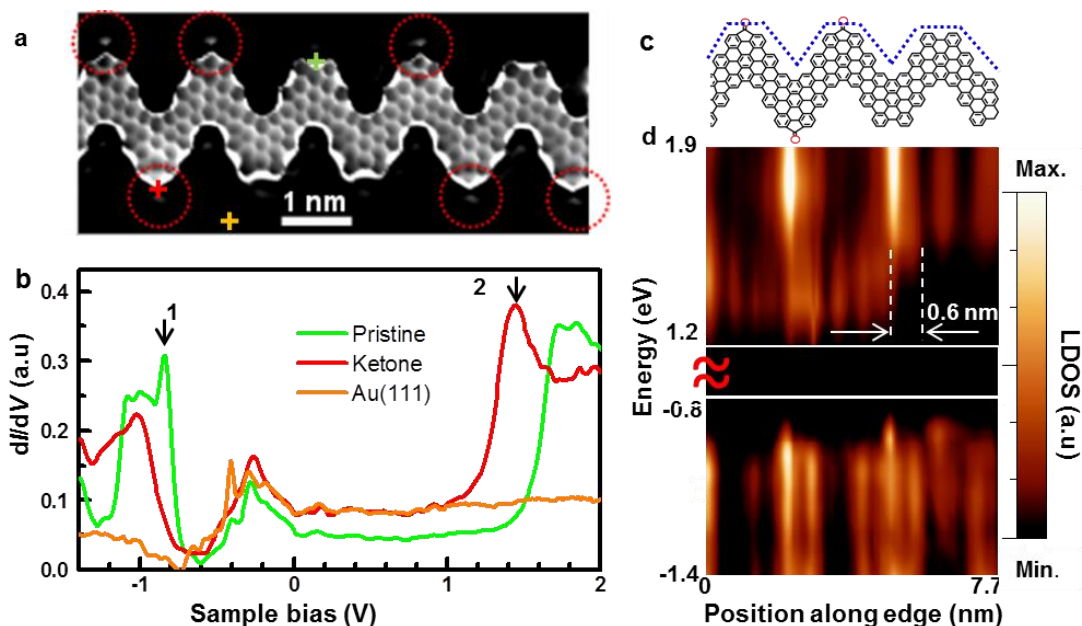
Figure 5.2: (a), BRSTM image of a ketone-pristine heterojunction (V_s = 40 mV, I_t = 10 pA, V_{ac} = 20 mV, f = 401 Hz). The red dashed rings indicate the position of ketone functional groups. (b), STM dI/dV spectroscopic measurement of the pristine-chevron heterojunction shown in (a). (d), dI/dV spectroscopic measurement along the edge of the heterojunction shown in (c) (blue dashed line). Band bending occurs over a distance of about 0.6 nm. A CB offset of ~0.30 eV leads to an effective field of 5×10^8 V/m across the interface.

In order to visualize the band alignment of the heterojunction, we performed dI/dV point spectroscopy measurements along the edge of the ketone-pristine heterojunction (dashed blue line in Figure 5.2c). Figure 5.2d shows the measured LDOS along the edge of the junction. The energy of the CB begins increasing sharply at the position of the first removed ketone group, indicating an atomically sharp interface region. Band bending occurs over a distance of about 0.6 nm. Over this narrow interface region, a CB band offset of ~0.30 eV leads to a huge effective field of 5×10^8 V/m across the interface, which is two orders of magnitude higher than the effective fields of traditional semiconductor p-n junctions [108]. Thus, there are promising electronic device applications for these ketone-pristine heterojunctions [108].
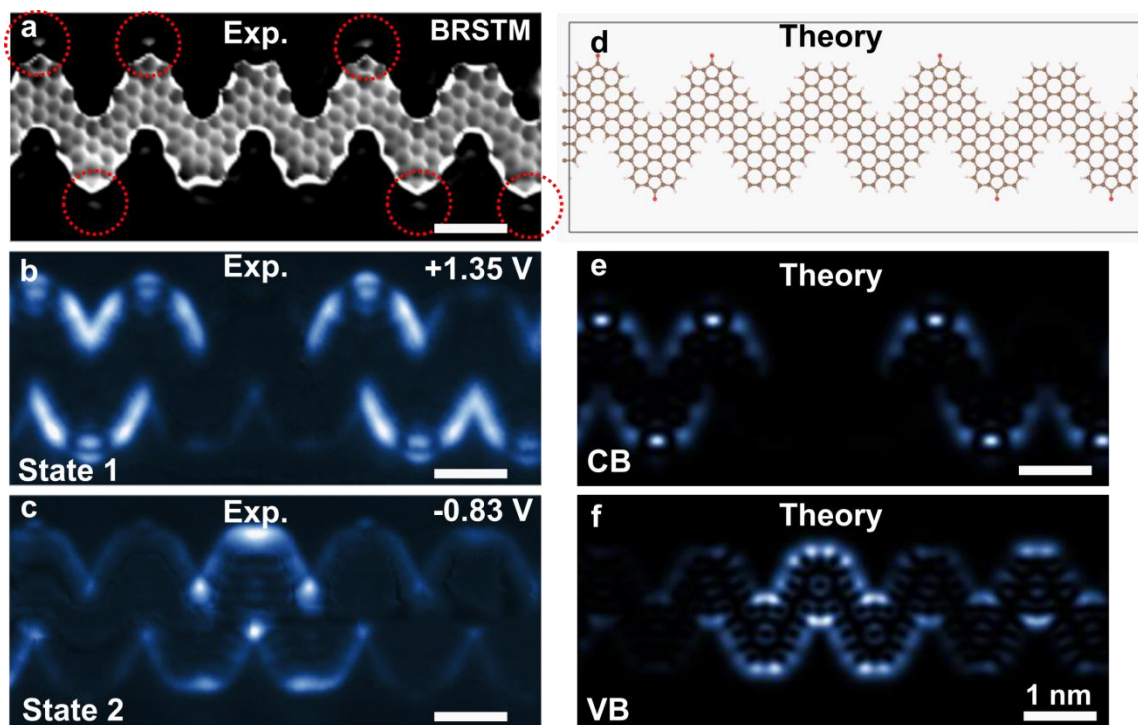
Figure 5.3: (a), BRSTM image of a ketone-pristine heterojunction (V_s = 40 mV, I_t = 10 pA, V_{ac} = 20 mV, f = 401 Hz). The red dashed rings indicate the positions of ketone groups. (b),(c) Experimental STM dI/dV maps of a pristine-chevron heterojunction recorded at the energy of spectroscopic peaks 1 and 2 in Figure 5.2b (V_{ac} = 20 mV, f = 401 Hz). (d), A unit cell resembling the same structure as experiment. (e),(f), Calculated LDOS maps of the CB and the VB at a constant height of 4 Å.

Figure 5.3a-c shows a BRSTM image (red dashed circles indicate the ketone positions) together with dI/dV maps of the same ketone-pristine GNR heterojunction as shown in Figure 5.2. dI/dV maps taken at the energies of the CB (state 1, 1.35 eV) (Figure 5.3b) and VB (state 2, −0.83 eV) (Figure 5.3c) of the heterojunction show alternation in LDOS intensity at the ketone segments and pristine segments, respectively. The LDOS pattern localized on the ketone segments at the energy of state 1 is the same as seen for the pure ketone GNR CB (Figure 4.10). Similarly, the LDOS pattern localized on the pristine segments at the energy of state 2 is the same as seen for the fully pristine GNR VB. This suggests a localization of the density of states in the different GNR regions and an absence of interference or hybridization between the ketone and pristine segments of the heterojunction. DFT calculations for the exact same structure (unit cell is shown in Figure 5.3d) allow us to compare the experiment to the theoretical CB LDOS (Figure 5.3e) and VB LDOS (Figure 5.f). We observe excellent agreement between the experimental dI/dV maps in Figure 5.3b,c with the theoretical LDOS maps in Figure 5e,f.

5.4 Summary

In conclusion, we have successfully fabricated an atomically sharp type II ketone-pristine GNR heterojunction with a band gap engineered by ketone functional groups. The electronic and structural properties of heterojunctions are characterized with scanning tunneling microscopy and spectroscopy (STM & STS) and chemical bond-resolved STM (BRSTM), respectively. First principle calculations are provided to strongly support our findings.

Chapter 6 :   Photoswitching   of Azobenzene on BN/Cu(111)

One of the ultimate goals of this research is to incorporate an optical functionality into our GNRs. From a bottom-up synthesis perspective, this could be accomplished by introducing covalently bonded ligands in the GNR that directly provide such functionality. One such potential ligand is azobenzene, a small molecule with well-known optical activity. Although we have not yet incorporate azobenzene into GNRs, this chapter describes our preliminary explorations of the behavior of azobenzene on surface that might allow observation of local molecular optical activity,

6.1 Introduction
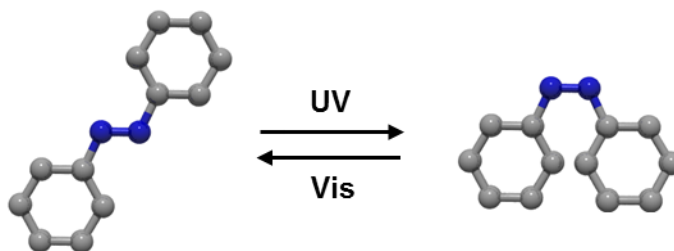
Figure 6.1: Photo-isomerization of an azobenzene molecule when illuminating with light.

Azobenzene molecules ($C_6H_5N=NH_5C_6$) is part of a novel class of molecular structures that can switch between two isomer states by photoexcitation [109–114]. This interesting property makes them a potential candidate for future opto-mechanical devices such as light-powered nanomachines [115,116], molecular electronics [116–118], and biochemical elements [109,117,119]. When irradiated by ultraviolet (UV) and visible light, azobenzene molecules reversibly switch between the *trans* and *cis* states (see Figure 6.1) [10,120]. However, in order to use this molecule for device applications, it is important to be able to study the molecule on a substrate [121,122]. Indeed, the substrate has a strong influence on the photo-switching properties of the molecules compared with gas- and solution-based environments [10,123,124]. This has been shown in previous studies with several different techniques such as electron energy loss spectroscopy [125], Raman spectroscopy [126,127], two-photon photoemission spectroscopy [128,129], and scanning tunneling microscopy (STM) [123,130–135]. Studies of azobenzene photoswitching so far have been conducted on metal surfaces such as Au(111) [10,113,133,135–138] and on the semiconductor surface GaAs(110) [123]. It has been found that bonding of the molecules to the surface often prevents photoswitching due to the reduction of the degrees of freedom in addition to hybridization of azobenzene states with surface states [10,77–80,134]. Consequently, successful photoswitching of

azobenzene molecules on these surfaces has only been accomplished by functionalizing the molecules to decouple them from the surface [10,136].

In this chapter, we describe an STM study of molecular photomechanical switching of pristine azobenzene molecules adsorbed on an insulating monolayer of CVD-grown boron nitride (BN) on Cu(111) [139,140]. This substrate was chosen because BN is insulating and will therefore reduce the coupling of the molecules to the substrate [141–144]. Molecules were deposited on the BN/Cu(111) at low temperature to form self-assembled islands. Upon exposure to UV radiation ($\lambda = 375$ nm) azobenzene islands on BN/Cu(111) did exhibit structural changes. However, the light-induced switching efficiency was not as high as those reported for azobenzene derivatives on other substrates such as Au(111) and GaAs(110) [123,137]. In order to increase the switching efficiency, we have explored using surface plasmon resonances to enhance the local field near the molecules [145–149]. Gold nanoislands were patterned on BN/Cu(111) through UHV deposition [150–152]. Due to the Moiré pattern of BN/Cu(111), gold deposited on the surface aggregates in specific regions of the Moiré pattern to form a periodic pattern [150–152]. Here we describe this work in greater details.

6.2 CVD growth of boron nitride (BN) on Cu(111)
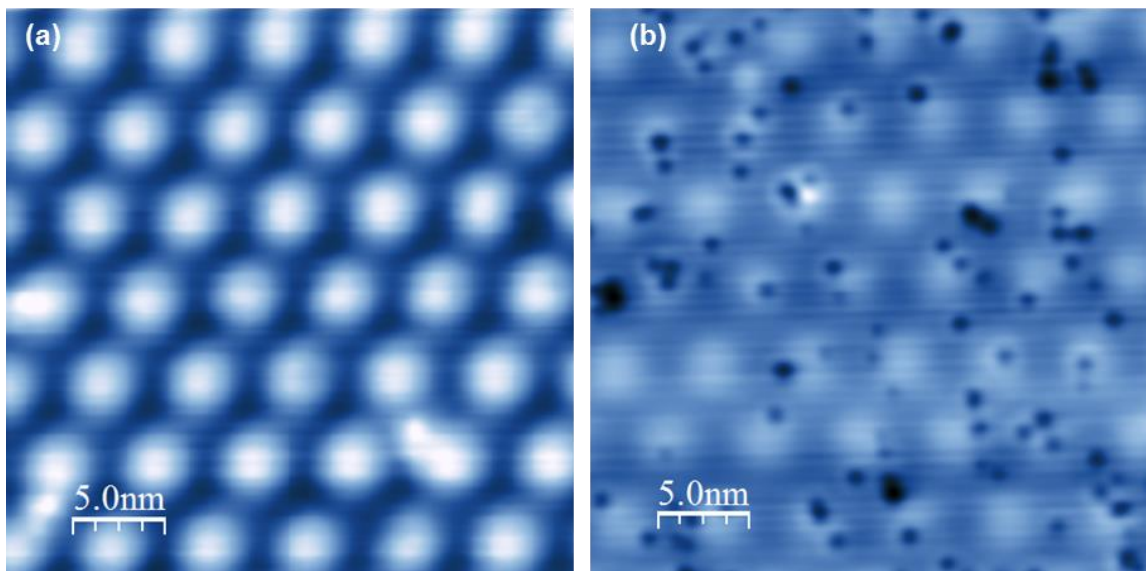
Figure 6.2: The typical STM images of the Moiré pattern of BN on Cu(111) scanning at different bias (a) ($V_s = 4.2$ V, $I_t = 100$ pA), (b) ($V_s = 0.5$ V, $I_t = 40$ pA).

The BN monolayer was grown on the Cu(111) crystal using a chemical vapor deposition method from borazine (HBNH)$_3$ precursors in a UHV system as shown in appendix A [139,140]. A Cu(111) single crystal was used as a substrate and cleaned by standard Ar$^+$ sputtering/annealing cycles. The borazine precursors were introduced into

the chamber through a leak valve while the Cu(111) substrate was kept at a temperature of about 800 °C. The typical images of BN/Cu(111) are seen in Figure 6.2. Scanning the surface at a high bias of 4.2 V, we are able to see the Moiré pattern of BN on a Cu(111) surface (Figure 6.2a) [139]. The periodicity of the observed Moiré pattern can vary from 5 nm to 14 nm, consistent with a previous report [139]. The higher the substrate temperature during growth, the larger the domain size of the Moiré patterns [139]. Scanning at a low bias of 0.5 V, defects on the Cu(111) surface underneath the BN can be observed (Figure 6.2b).

6.3 Photoswitching of Azobenezene on BN/Cu(111).
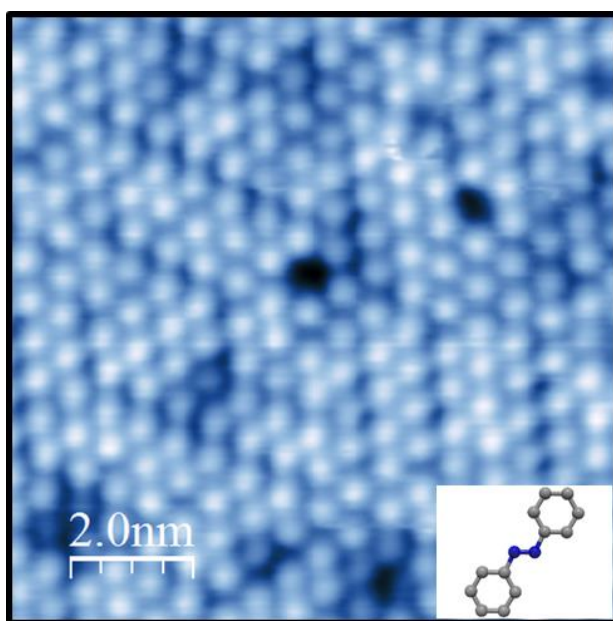
Figure 6.3: STM topographic images of self-assembled azobenzene molecules on the BN/Cu(111) ($V_s = -1.4$ V, $I_t = 20$ pA). The chemical structure of an azobenzene molecule is shown in the inset.

Azobenzene molecules were deposited onto a BN/Cu(111) surface through a leak valve between the molecule source and preparation chamber [77,113]. The molecules in powder form are contained in a sealed glass tube. In order to get a high purity of azobenzene vapor, the sealed tube is passed through several pump and purge cycles. We find it is important to precool the BN/Cu(111) substrate in the STM chamber at 13 K [153] before depositing the molecules. The sample is then taken out into the preparation chamber and left on the manipulator facing toward the molecular source for a few minutes. During the deposition, the leak valve was controlled to maintain the pressure in the preparation chamber at about $\sim 10^{-9}$ torr. After deposition, the sample was transferred into the STM chamber and cooled down to 13 K before scanning. Likely due to small

interaction between azobenzene molecules and the BN surface, these molecules seem to be very mobile on the surface. It was not possible to get stable STM images of the molecules on BN at positive sample biases. However, STM images at negative biases were more stable and were best at about −1.4 V. A typical image of azobenzene molecules on BN/Cu(111) is shown in Figure 6.3. The molecules in the *trans* state are self-assembled in a close packed structure [77,113].

Figure 6.4 shows the d*I*/d*V* spectroscopic measurement on molecules at different regions (hollow and valley) on the Moiré pattern of BN/Cu(111). Due to a variation of local work function at different regions [141], we observed the highest occupied molecular orbital (HOMO) peak at different energies in the Moiré pattern (−1.4 eV at Moiré hollow positions and −1.22 eV at Moiré valley positions). This energy level of the HOMO is comparable with measuremenst in a previous study of azobenzene on Au(111) [138]. In addition, the fact that the HOMO energy level of azobenzene molecules lies between −1.4 eV and −1.2 eV explains why a sample bias of -1.4V provides the best image contrast. At this bias, the electrons from the HOMO of the molecules can tunnel into unoccupied states of the tip.
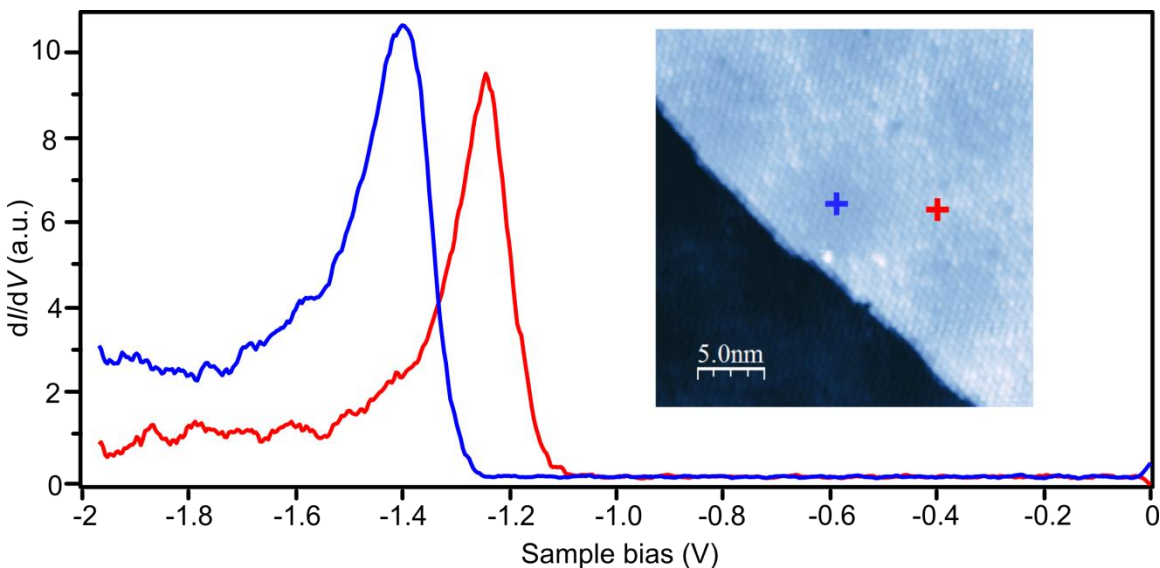
Figure 6.4: STM d*I*/d*V* spectra of azobenzene recorded on the hollow (blue) and valley (red) of the Moiré pattern of BN/Cu(111) (hollow: blue, valley: red). Crosses in the topographic STM image (inset) indicate the positions of recorded spectra ($V_s = -1.4$ V, $I_t = 30$ pA).

To study the photo-switching of azobenzene on BN/Cu(111), the surface was illuminated using a UV laser with a wavelength of 375 nm [10,123,133,135]. The same spots were always checked before and after illumination.
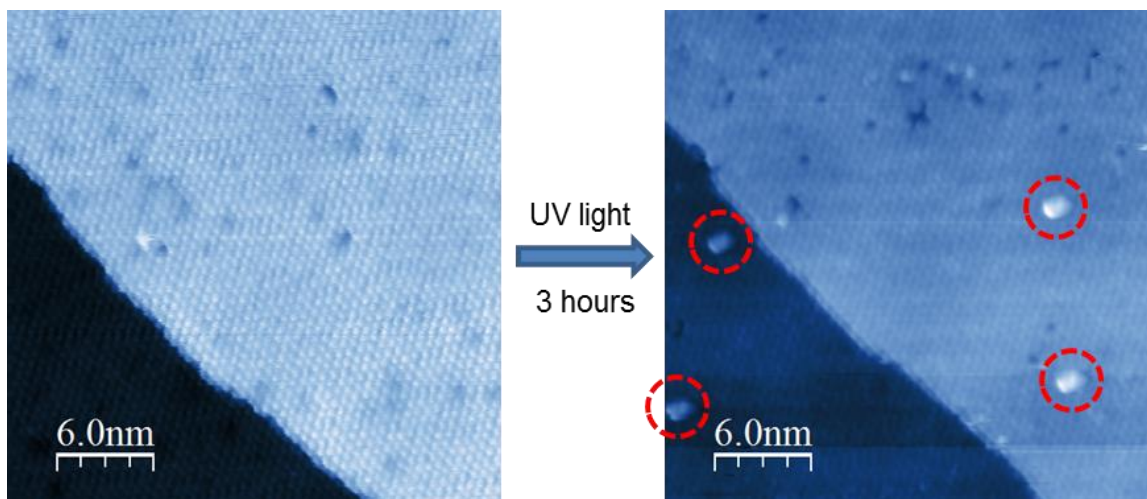
Figure 6.5: The STM topographic images of azobenzene on BN/Cu(111) taken at the same place before and after shining UV light (tip is kept 50 nm away from the surface during illumination). Scanning parameters are $V_s = -1.4$ V, $I_t = 30$ pA.

Figure 6.5 shows STM topographic images before and after shining a UV laser on azobenzene/BN/Cu(111) for 3 hours. The tip was left close to the surface during the illumination. The red circles identify switched molecules on the surface after shining.
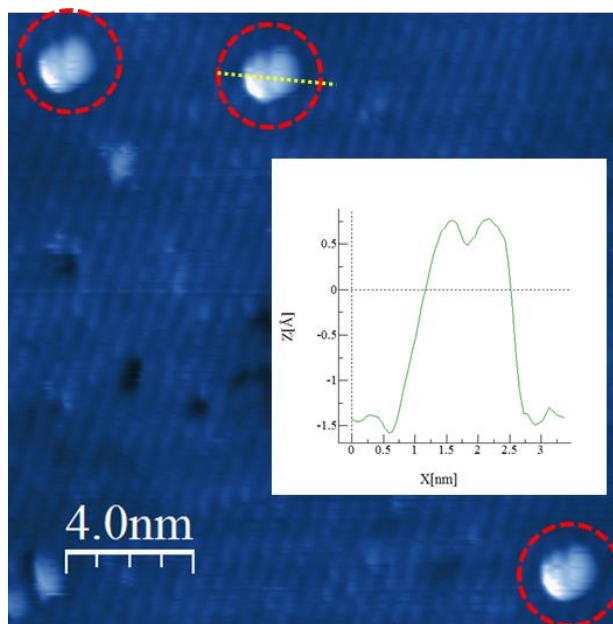
Figure 6.6: Zoom-in STM topographic image on switched molecules after shining UV light ($V_s = -1.4$ V, $I_t = 30$ pA). Inset image is a cross section above a switched molecule.

In order to the better understand the switched molecules that appear after shining light, we took a closer look as shown in Figure 6.6. The inset presents a cross-section of a switched molecule. The height and width are comparable with the size of a single azobenzene molecule which indicates that the switched molecules are lying on top of molecular islands. In addition, there are more dark holes on the molecular islands after shining UV light.

Due to these observations, we propose a process whereby azobenzene molecules absorb light and transform from *trans* to *cis* states and then hop onto the second layer. The reason for this is that the switched molecules in the *cis* state do not fit the self-assembled monolayer structure and therefore increased strain that makes it energetically favorable for them to pop up on top of the molecular islands and leave behind a dark hole.

To avoid the possibility of a shadowing of the surface by the tip, we also illuminated the molecules on BN/Cu(111) when the tip was retracted far from the surface. Figure 6.7 present an STM image at the same spot before and after 0.5 hours of light exposure. Here we are able to see more switched molecules on the surface that are very interactive with the STM tip during scanning. They sometimes disappear after one scan. This behavior can be attributed to the small binding energy of switched molecules to the underlying island, allowing them to easily jump to the STM tip during scanning.
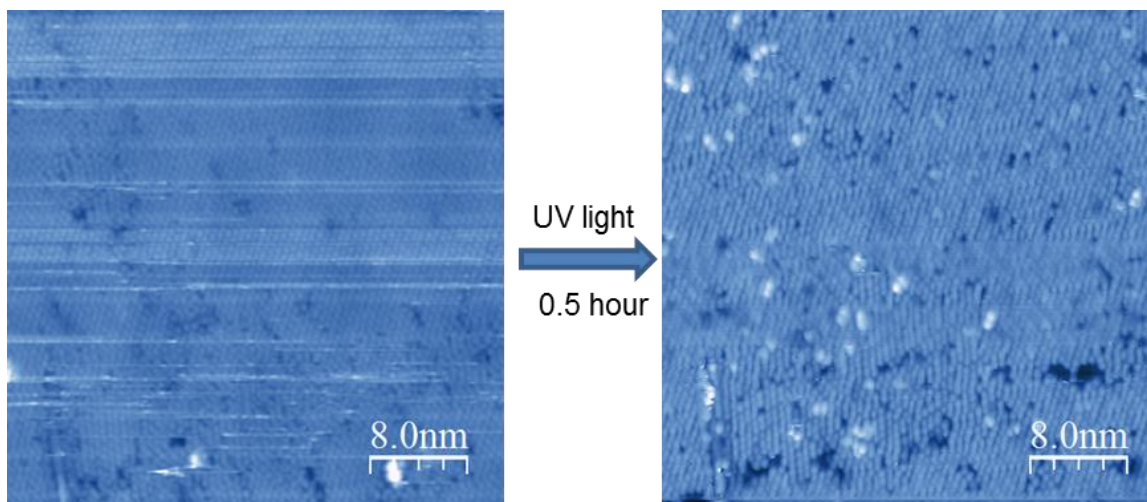
Figure 6.7: The STM topographic images of azobenzene on BN/Cu(111) taken at the same places before and after shining UV light. The tip was fully withdrawn far away from the surface when shining light. Scanning parameters are $V_s = -1.4$ V, $I_t = 30$ pA.

Figure 6.8 presents the change in the structure of azobenzene molecular islands after shinning UV light for 7 hours. We observe many more switched molecules after

shining light for this long period. However, the surface is very unstable which we believe is due to the large quantity of switched molecules on top of the islands.
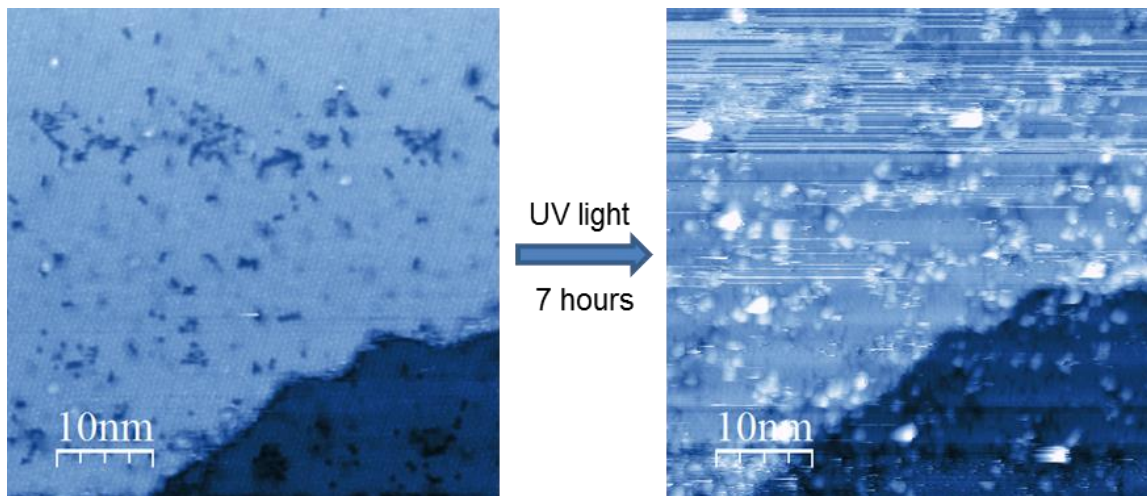
Figure 6.8: The STM topographic images of azobenzene on BN/Cu(111) taken at the same places before and after shining UV light. The tip was fully withdrawn far away from the surface when shining light. Scanning parameters are $V_s = -1.4$ V, $I_t = 30$ pA.

6.4 Growth of gold clusters on BN/Cu(111)
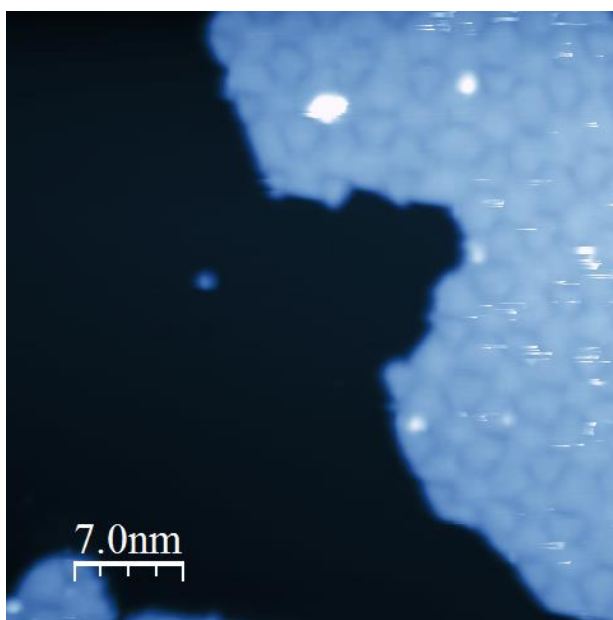
Figure 6.9: The typical STM image of the Moiré pattern of Au submonolayer on Cu(111) after deposition 1 mins ($V_s = 0.5$ V, $I_t = 20$ pA).

In order to increase the photo-switching efficiency as well as control molecular photoswitching at the molecular scale, we attempted to utilize field enhancement due to the local surface plasmon resonance of nanoparticles [126,145–149]. The idea here is to decorate BN/Cu(111) surface with gold islands by using evaporating gold into the UHV system. A gold evaporator was first tested using a Quartz Crystal Microbalance (QCM) in a test chamber. The sublimation rate was then re-calibrated again after mounting the evaporator onto the preparation chamber and depositing gold onto a clean Cu(111) surface. Due to the mismatch of lattice constant between gold and copper, we can clearly see the Moiré pattern created by the submonolayer of gold on Cu(111) (Figure 6.9) .

Gold was then deposited onto a BN/Cu(111) substrate held at room temperature. Figure 6.10a shows an STM topographic image of Au islands on BN/Cu(111) [150,152]. The gold clusters typically stay within the Moiré pattern on BN/Cu(111) [150,152]. This can be explained by an attractive dipole field created in the Moiré pattern of BN on Cu(111) [150]. Figure 6.10b shows the cross section across a single gold island. The diameter and the height of gold clusters are between 6 nm to 10 nm and 0.7 nm to 1.2 nm respectively. Future plans involve using these gold clusters on BN/Cu(111) as a substrate for depositing azobenzene molecules. Upon illuminating with UV light, we expect the local field around gold clusters to be higher, thus increasing the switching efficiency of azobenzene molecules.
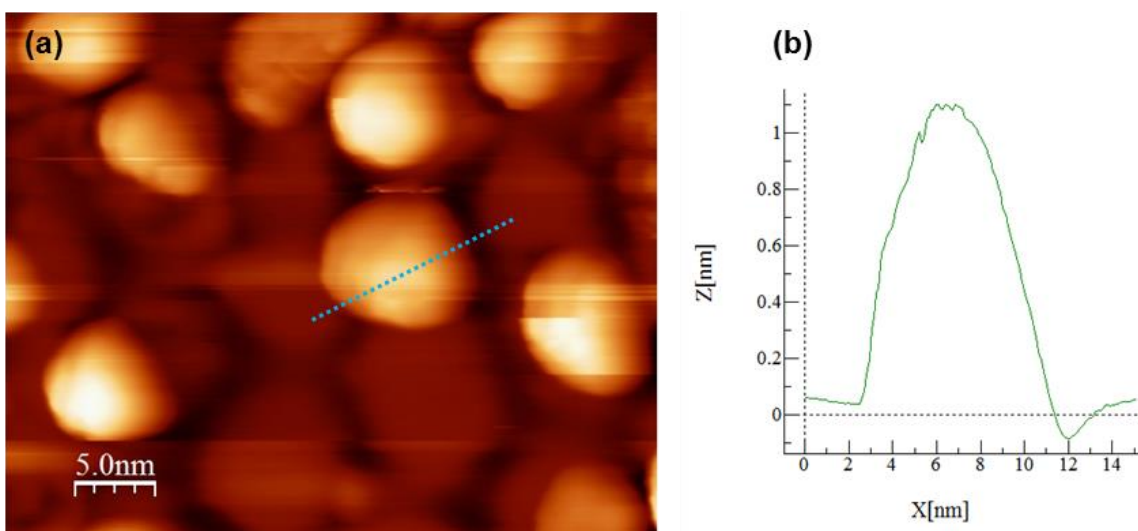
Figure 6.10: (a) The typical STM topographic image of Au clusters on BN/Cu(111) after deposition in 1 mins ($V_s = 4$ V, $I_t = 40$ pA). (b) The line cross of the image in (a).

6.5 Summary

We have performed a preliminary study on the photoswitching properties of azobenzene on an insulating BN monolayer on Cu(111). We find that the molecules are

very mobile on the BN/Cu(111) surface, but appear to be self-assembled in close-packed islands in STM topographic images when scanning at negative bias. Upon UV illumination, the molecules undergo a photoswitching process which we believe is related to *trans-cis* photoisomerization. However, future investigation must be done to fully understand the switching properties. We propose that gold islands deposited on BN/Cu(111) can be used to enhance azobenzene switching efficiency through a local surface plasmon resonance.

Bibliography

[1]   D.A. Buchanan, D.J. Frank, K.E. Ismail, G.A. Sai-Halasz, R.G. Viswanathan, H.-J.C. Wann, and S.J. Wind, Proceedings of the IEEE **85**, 486–504 (1997).

[2]   S. Mutoh, T. Douseki, Y. Matsuya, T. Aoki, S. Shigematsu, and J. Yamada, IEEE Journal of Solid-State Circuits **30**, 847–854 (1995).

[3]   B. Davari, R.H. Dennard, and G.G. Shahidi, Proceedings of the IEEE **83**, 595–606 (1995).

[4]   S. Novak, C. Parker, D. Becher, M. Liu, M. Agostinelli, M. Chahal, P. Packan, P. Nayak, S. Ramey, and S. Natarajan, in *2015 IEEE International Reliability Physics Symposium* (IEEE, 2015), pp. 2F.2.1–2F.2.5.

[5]   C.-H. Jan, F. Al-amoody, H.-Y. Chang, T. Chang, Y.-W. Chen, N. Dias, W. Hafez, D. Ingerly, M. Jang, E. Karl, S. K.-Y. Shi, K. Komeyli, H. Kilambi, A. Kumar, K. Byon, C.-G. Lee, J. Lee, T. Leo, P.-C. Liu, N. Nidhi, R. Olac-vaw, C. Petersburg, K. Phoa, C. Prasad, C. Quincy, R. Ramaswamy, T. Rana, L. Rockford, A. Subramaniam, C. Tsai, P. Vandervoorn, L. Yang, A. Zainuddin, and P. Bai, in *2015 Symposium on VLSI Technology (VLSI Technology)* (IEEE, 2015), pp. T12–T13.

[6]   EE Times (2014).

[7]   Kerry Bernstein, Ralph K. Cavin, Wolfgang Porod, Alan Seabaugh, and Jeff Welser, Proceedings of the IEEE **98**, 2169–2184 (2010).

[8]   Dmitri E. Nikonov and Ian a. Young, IEEE Proceedings **101**, 2498–2533 (2013).

[9]   Yong Chen, Gun-Young Jung, Douglas A A Ohlberg, Xuema Li, Duncan R Stewart, Jan O Jeppesen, Kent A Nielsen, J Fraser Stoddart, and R Stanley Williams, Nanotechnology **14**, 462–468 (2003).

[10]   Matthew J Comstock, Niv Levy, Armen Kirakosian, Jongweon Cho, Frank Lauterwasser, Jessica H Harvey, David A Strubbe, Jean M J Fréchet, Dirk Trauner, Steven G Louie, and Michael F Crommie, Physical Review Letters **99**, 038301 (2007).

[11]   Wesley R Browne and Ben L Feringa, Nature Nanotechnology **1**, 25–35 (2006).

[12]   A. N. Aleshin, Advanced Materials **18**, 17–27 (2006).

[13]   G. Whitesides, J. Mathias, and C. Seto, Science **254**, 1312–1319 (1991).

[14]   I. H. Campbell, S. Rubin, T. A. Zawodzinski, J. D. Kress, R. L. Martin, D. L. Smith, N. N. Barashkov, and J. P. Ferraris, Physical Review B **54**, R14321–R14324 (1996).

[15]   Ali Javey, Jing Guo, Qian Wang, Mark Lundstrom, and Hongjie Dai, Nature **424**, 654–7 (2003).

[16]   Jinming Cai, Pascal Ruffieux, Rached Jaafar, Marco Bieri, Thomas Braun, Stephan Blankenburg, Matthias Muoth, Ari P Seitsonen, Moussa Saleh, Xinliang Feng, Klaus Müllen, and Roman Fasel, Nature **466**, 470–3 (2010).

[17]   Yen Chia Chen, Dimas G. De Oteyza, Zahra Pedramrazi, Chen Chen, Felix R. Fischer, and Michael F. Crommie, ACS Nano **7**, 6123–6128 (2013).

[18]   Leopold Talirz, Pascal Ruffieux, and Roman Fasel, Advanced Materials (Deerfield Beach, Fla) (2016).

[19]   Jinming Cai, Carlo A. Pignedoli, Leopold Talirz, Pascal Ruffieux, Hajo Söde, Liangbo Liang, Vincent Meunier, Reinhard Berger, Rongjin Li, Xinliang Feng, Klaus Müllen, and Roman Fasel, Nature Nanotechnology **9**, 896–900 (2014).

[20]   Yen-Chia Chen, Ting Cao, Chen Chen, Zahra Pedramrazi, Danny Haberer, Dimas G. de Oteyza, Felix R. Fischer, Steven G. Louie, and Michael F. Crommie, Nature Nanotechnology **10**, 156–160 (2015).

[21]   Ryan R Cloke, Tomas Marangoni, Giang D Nguyen, Trinity Joshi, Daniel J Rizzo, Christopher Bronner, Ting Cao, Steven G Louie, Michael F Crommie, and Felix R Fischer, Journal of the American Chemical Society **137**, 8872–5 (2015).

[22]   Thomas Dienel, Shigeki Kawai, Hajo Söde, Xinliang Feng, Klaus Müllen, Pascal Ruffieux, Roman Fasel, and Oliver Gröning, Nano Letters **15**, 5185–5190 (2015).

[23]   Patrick Han, Kazuto Akagi, Filippo Federici Canova, Hirotaka Mutoh, Susumu Shiraki, Katsuya Iwaya, Paul S Weiss, Naoki Asao, and Taro Hitosugi, ACS Nano **8**, 9181–7 (2014).

[24]   Patrick B. Bennett, Zahra Pedramrazi, Ali Madani, Yen-Chia Chen, Dimas G. de Oteyza, Chen Chen, Felix R. Fischer, Michael F. Crommie, and Jeffrey Bokor, Applied Physics Letters **103**, 253114 (2013).

[25]   Pascal Ruffieux, Shiyong Wang, Bo Yang, Carlos Sánchez-Sánchez, Jia Liu, Thomas Dienel, Leopold Talirz, Prashant Shinde, Carlo A. Pignedoli, Daniele Passerone, Tim Dumslaff, Xinliang Feng, Klaus Müllen, and Roman Fasel, Nature **531**, 489–492 (2016).

[26]   Junzhi Liu, Bo-Wei Li, Yuanzhi Tan, Angelos Giannakopoulos, Carlos Sanchez-Sanchez, David Beljonne, Pascal Ruffieux, Roman Fasel, Xinliang Feng, and Klaus Müllen, Journal of the American Chemical Society **137**, 6097–6103 (2015).

[27]   A. K. Geim and K. S. Novoselov, Nature Materials **6**, 183–191 (2007).

[28]   A. H. Castro Neto, N. M. R. Peres, K. S. Novoselov, and A. K. Geim, Reviews of Modern Physics **81**, 109–162 (2009).

[29]   Jens Baringhaus, Ming Ruan, Frederik Edler, Antonio Tejeda, Muriel Sicot, Amina Taleb-Ibrahimi, An-Ping Li, Zhigang Jiang, Edward H Conrad, Claire Berger, Christoph Tegenkamp, and Walt A de Heer, Nature **506**, 349–54 (2014).

[30]   Li Yang, Marvin L Cohen, and Steven G Louie, Nano Letters **7**, 3112–5 (2007).

[31]   Ricardo Faccio, Pablo A Denis, Helena Pardo, Cecilia Goyenola, and Alvaro W Mombrú, Journal of Physics Condensed Matter : An Institute of Physics Journal **21**, 285304 (2009).

[32]   Young-Woo Son, Marvin L Cohen, and Steven G Louie, Nature **444**, 347–9 (2006).

[33]   Melinda Han, Barbaros Özyilmaz, Yuanbo Zhang, and Philip Kim, Physical Review Letters **98**, 206805 (2007).

[34]   Young-Woo Son, Marvin L. Cohen, and Steven G. Louie, Physical Review Letters **97**, 216803 (2006).

[35]   Haiming Zhang, Haiping Lin, Kewei Sun, Long Chen, Yulian Zagranyarski, Nabi Aghdassi, Steffen Duhm, Qing Li, Dingyong Zhong, Youyong Li, Klaus Müllen, Harald Fuchs, and Lifeng Chi, Journal of the American Chemical Society **137**, 4022–5 (2015).

[36]   Ryan R. Cloke, Tomas Marangoni, Giang D. Nguyen, Trinity Joshi, Daniel J. Rizzo, Christopher Bronner, Ting Cao, Steven G. Louie, Michael F. Crommie, and Felix R. Fischer, Journal of the American Chemical Society **137**, 8872–8875 (2015).

[37]   Giang D. Nguyen, Francesca M. Toma, Ting Cao, Zahra Pedramrazi, Chen Chen, Daniel J. Rizzo, Trinity Joshi, Christopher Bronner, Yen-Chia Chen, Marco Favaro, Steven G. Louie, Felix R. Fischer, and Michael F. Crommie, The Journal of Physical Chemistry C **120**, 2684–2687 (2016).

[38]   Christopher Bronner, Stephan Stremlau, Marie Gille, Felix Brauße, Anton Haase, Stefan Hecht, and Petra Tegeder, Angewandte Chemie - International Edition **52**,

4422–4425 (2013).

[39]   Shigeki Kawai, Shohei Saito, Shinichiro Osumi, Shigehiro Yamaguchi, Adam S Foster, Peter Spijker, and Ernst Meyer, Nature Communications **6**, 8098 (2015).

[40]   Yi Zhang, Yanfang Zhang, Geng Li, Jianchen Lu, Xiao Lin, Shixuan Du, Reinhard Berger, Xinliang Feng, Klaus Müllen, and Hong-Jun Gao, Applied Physics Letters **105**, 023101 (2014).

[41]   Timothy H Vo, U Gayani E Perera, Mikhail Shekhirev, Mohammad Mehdi Pour, Donna A Kunkel, Haidong Lu, Alexei Gruverman, Eli Sutter, Mircea Cotlet, Dmytro Nykypanchuk, Percy Zahl, Axel Enders, Alexander Sinitskii, and Peter Sutter, Nano Letters **15**, 5770–7 (2015).

[42]   Akimitsu Narita, Xiao-Ye Wang, Xinliang Feng, and Klaus Müllen, Chemical Society Reviews **44**, 6616–6643 (2015).

[43]   Gengchiau Liang, Neophytos Neophytou, Dmitri E. Nikonov, and Mark S. Lundstrom, IEEE Transactions on Electron Devices **54**, 677–682 (2007).

[44]   Simon M. Sze and Kwok K. Ng, John Wiley & Sons, Inc (2007).

[45]   B.I. Shklovskii and A.L. Efros, *Electronic Properties of Doped Semiconductors* (Springer Science & Business Media, 2013).

[46]   G. Binnig, H. Rohrer, Ch. Gerber, and E. Weibel, Physical Review Letters **50**, 120–123 (1983).

[47]   G. Binnig, Applied Physics Letters **40**, 178 (1982).

[48]   G. Binnig, H. Rohrer, Ch. Gerber, and E. Weibel, Physical Review Letters **49**, 57–61 (1982).

[49]   J. Tersoff and D. R. Hamann, Physical Review B **31**, 805–813 (1985).

[50]   J. Bardeen, Physical Review Letters **6**, 57–59 (1961).

[51]   Ryan Tsuyoshi Yamachika, PhD Thesis - University of California, Berkeley (2009).

[52]   G. Binnig and C. F. Quate, Physical Review Letters **56**, 930–933 (1986).

[53]   S. a. Burke, J. M. Mativetsky, S. Fostner, and P. Grütter, Phys Rev B **76**, 1–9 (2007).

[54]   T Fukuma, K Kobayashi, K Noda, K Ishida, T Horiuchi, H Yamada, and K Matsushige, Surface Science **516**, 103–108 (2002).

[55]   J V Lauritsen and M Reichling, Journal of Physics Condensed Matter : An Institute of Physics Journal **22**, 263001 (2010).

[56]   Bartosz Such, Pawel Czuba, Piotr Piatkowski, and M Szymonski, Surface Science **451**, 203–207 (2000).

[57]   J Wang, A Howard, R G Egdell, J B Pethica, and J S Foord, **515**, 337–343 (2002).

[58]   Mendel In't Veld, Patrizia Iavicoli, Sam Haq, David B Amabilino, and Rasmita Raval, Chemical Communications (Cambridge, England) 1536–8 (2008).

[59]   Franz J. Giessibl, Applied Physics Letters **73**, 3956–3958 (1998).

[60]   Franz J Giessibl, Reviews of Modern Physics **75**, 949–983 (2003).

[61]   Leo Gross, Fabian Mohn, Nikolaj Moll, Peter Liljeroth, and Gerhard Meyer, Science (New York, NY) **325**, 1110–4 (2009).

[62]   G. M. King, J. S. Lamb, and G. Nunes, Applied Physics Letters **79**, 1712 (2001).

[63]   G. M. King and G. Nunes, Review of Scientific Instruments **72**, 4261 (2001).

[64]   Wei Yang, Guorui Chen, Zhiwen Shi, Cheng-Cheng Liu, Lianchang Zhang, Guibai Xie, Meng Cheng, Duoming Wang, Rong Yang, Dongxia Shi, Kenji Watanabe, Takashi Taniguchi, Yugui Yao, Yuanbo Zhang, and Guangyu Zhang, Nature Materials **12**, 792–7 (2013).

[65]   Régis Decker, Yang Wang, Victor W Brar, William Regan, Hsin-Zon Tsai, Qiong Wu, William Gannett, Alex Zettl, and Michael F Crommie, Nano Letters **11**, 2291–5 (2011).

[66]   J. Xua, PhD Thesis - University of Arizona (2012).

[67]   Bruno Schuler, Wei Liu, Alexandre Tkatchenko, Nikolaj Moll, Gerhard Meyer, Anish Mistry, David Fox, and Leo Gross, Physical Review Letters **111**, 106103 (2013).

[68]   Dimas G de Oteyza, Patrick Gorman, Yen-Chia Chen, Sebastian Wickenburg, Alexander Riss, Duncan J Mowbray, Grisha Etkin, Zahra Pedramrazi, Hsin-Zon Tsai, Angel Rubio, Michael F Crommie, and Felix R Fischer, Science (New York, NY) **340**, 1434–7 (2013).

[69] Chi-lun Chiang, Chen Xu, Zhumin Han, and W Ho, Science (New York, NY) **344**, 885–8 (2014).

[70] Prokop Hapala, Ruslan Temirov, F Stefan Tautz, and Pavel Jelínek, Physical Review Letters **113**, 226101 (2014).

[71] Georgy Kichin, Christian Weiss, Christian Wagner, F Stefan Tautz, and Ruslan Temirov, Journal of the American Chemical Society **133**, 16847–51 (2011).

[72] J I Martínez, E Abad, C González, F Flores, and J Ortega, Physical Review Letters **108**, 246102 (2012).

[73] R Temirov, S Soubatch, O Neucheva, A C Lassise, and F S Tautz, New Journal of Physics **10**, 053012 (2008).

[74] C Weiss, C Wagner, C Kleimann, M Rohlfing, F S Tautz, and R Temirov, Physical Review Letters **105**, 086103 (2010).

[75] Prokop Hapala, Georgy Kichin, Christian Wagner, F. Stefan Tautz, Ruslan Temirov, and Pavel Jelínek, Physical Review B **90**, 085421 (2014).

[76] Maurice L. Huggins, Journal of the American Chemical Society **75**, 4126–4133 (1953).

[77] M. J. Comstock, PhD Thesis - University of California, Berkeley (2013).

[78] Niv Levy, PhD Thesis - University of California, Berkeley (2009).

[79] J. Cho, PhD Thesis - University of California, Berkeley (2010).

[80] I. V. Pechenezhskiy, PhD Thesis - University of California, Berkeley (2013).

[81] Young-Woo Son, Marvin L Cohen, and Steven G Louie, Nature **444**, 347–349 (2006).

[82] Chenggang Tao, Liying Jiao, Oleg V. Yazyev, Yen-Chia Chen, Juanjuan Feng, Xiaowei Zhang, Rodrigo B. Capaz, James M. Tour, Alex Zettl, Steven G. Louie, Hongjie Dai, and Michael F. Crommie, Nature Physics **7**, 616–620 (2011).

[83] Patrick Han, Kazuto Akagi, Filippo Federici Canova, Ryota Shimizu, Hiroyuki Oguchi, Susumu Shiraki, Paul S Weiss, Naoki Asao, and Taro Hitosugi, ACS Nano **9**, 12035–44 (2015).

[84] R. E Davis, L. E., MacDonald, N. C., Palmberg, P. W., Riach, G. E., Weber, *Handbook of Auger Electron Spectroscopy* (Physical Electronics Industries:

Minnesota, 1976).

[85]   J.L. Ong and L.C. Lucas, Biomaterials **19**, 455–464 (1998).

[86]   Siegfried Hofmann, *Auger- and X-Ray Photoelectron Spectroscopy in Materials Science* (Springer Berlin Heidelberg, Berlin, Heidelberg, 2013).

[87]   M. Maglietta, F. Pratesi, and G. Rovida, Chemical Physics Letters **36**, 436–440 (1975).

[88]   W. Chen, V. Madhavan, T. Jamneala, and M. F. Crommie, Physical Review Letters **80**, 1469–1472 (1998).

[89]   Pascal Ruffieux, Jinming Cai, Nicholas C. Plumb, Luc Patthey, Deborah Prezzi, Andrea Ferretti, Elisa Molinari, Xinliang Feng, Klaus Müllen, Carlo A. Pignedoli, and Roman Fasel, ACS Nano **6**, 6930–6935 (2012).

[90]   Paolo Giannozzi, Stefano Baroni, Nicola Bonini, Matteo Calandra, Roberto Car, Carlo Cavazzoni, Davide Ceresoli, Guido L Chiarotti, Matteo Cococcioni, Ismaila Dabo, Andrea Dal Corso, Stefano de Gironcoli, Stefano Fabris, Guido Fratesi, Ralph Gebauer, Uwe Gerstmann, Christos Gougoussis, Anton Kokalj, Michele Lazzeri, Layla Martin-Samos, Nicola Marzari, Francesco Mauri, Riccardo Mazzarello, Stefano Paolini, Alfredo Pasquarello, Lorenzo Paulatto, Carlo Sbraccia, Sandro Scandolo, Gabriele Sclauzero, Ari P Seitsonen, Alexander Smogunov, Paolo Umari, and Renata M Wentzcovitch, Journal of Physics Condensed Matter : An Institute of Physics Journal **21**, 395502 (2009).

[91]   N. Troullier and José Luriaas Martins, Physical Review B **43**, 1993–2006 (1991).

[92]   Zhi Yang, Zhen Yao, Guifa Li, Guoyong Fang, Huagui Nie, Zheng Liu, Xuemei Zhou, Xi'an Chen, and Shaoming Huang, ACS Nano **6**, 205–11 (2012).

[93]   V. Madhavan, W. Chen, T. Jamneala, M. F. Crommie, and Ned S. Wingreen, Physical Review B **64**, 165412 (2001).

[94]   Andrea Basagni, Francesco Sedona, Carlo A Pignedoli, Mattia Cattelan, Louis Nicolas, Maurizio Casarin, and Mauro Sambi, Journal of the American Chemical Society **137**, 1802–8 (2015).

[95]   Akimitsu Narita, Ivan A Verzhbitskiy, Wout Frederickx, Kunal S Mali, Soeren Alkaersig Jensen, Michael Ryan Hansen, Mischa Bonn, Steven De Feyter, Cinzia Casiraghi, Xinliang Feng, and Klaus Müllen, ACS Nano **8**, 11622–30 (2014).

[96]   Leopold Talirz, Hajo Söde, Jinming Cai, Pascal Ruffieux, Stephan Blankenburg, Rached Jafaar, Reinhard Berger, Xinliang Feng, Klaus Müllen, Daniele Passerone,

Roman Fasel, and Carlo A Pignedoli, Journal of the American Chemical Society **135**, 2060–2063 (2013).

[97]   Timothy H Vo, Mikhail Shekhirev, Donna A Kunkel, Martha D Morton, Eric Berglund, Lingmei Kong, Peter M Wilson, Peter A Dowben, Axel Enders, and Alexander Sinitskii, Nature Communications **5**, 3189 (2014).

[98]   R. Paniago, R. Matzdorf, G. Meister, and A. Goldmann, Surface Science **336**, 113–122 (1995).

[99]   Susanne Bieller, Fan Zhang, Michael Bolte, Jan W. Bats, Hans-Wolfram Lerner, and Matthias Wagner, Organometallics **23**, 2107–2113 (2004).

[100] Claas Hoffend, Frauke Schödel, Michael Bolte, Hans-Wolfram Lerner, and Matthias Wagner, Chemistry (Weinheim an Der Bergstrasse, Germany) **18**, 15394–405 (2012).

[101] Chuandong Dou, Shohei Saito, Kyohei Matsuo, Ichiro Hisaki, and Shigehiro Yamaguchi, Angewandte Chemie (International Ed in English) **51**, 12206–10 (2012).

[102] Alexander Riss, Sebastian Wickenburg, Patrick Gorman, Liang Z Tan, Hsin-Zon Tsai, Dimas G de Oteyza, Yen-Chia Chen, Aaron J Bradley, Miguel M Ugeda, Grisha Etkin, Steven G Louie, Felix R Fischer, and Michael F Crommie, Nano Letters **14**, 2251–5 (2014).

[103] Stephan Blankenburg, Jinming Cai, Pascal Ruffieux, Rached Jaafar, Daniele Passerone, Xinliang Feng, Klaus Müllen, Roman Fasel, and Carlo A. Pignedoli, ACS Nano **6**, 2020–2025 (2012).

[104] Arunabh Batra, Dean Cvetko, Gregor Kladnik, Olgun Adak, Claudia Cardoso, Andrea Ferretti, Deborah Prezzi, Elisa Molinari, Alberto Morgante, and Latha Venkataraman, Chem Sci **5**, 4419–4423 (2014).

[105] Christopher Bronner, Jonas Björk, and Petra Tegeder, The Journal of Physical Chemistry C **119**, 486–493 (2015).

[106] Jack Deslippe, Georgy Samsonidze, David A. Strubbe, Manish Jain, Marvin L. Cohen, and Steven G. Louie, Computer Physics Communications **183**, 1269–1289 (2012).

[107] Han Huang, Dacheng Wei, Jiatao Sun, Swee Liang Wong, Yuan Ping Feng, a H Castro Neto, and Andrew Thye Shen Wee, Scientific Reports **2**, 983 (2012).

[108] D. A. Neamen, *Semiconductor Physics and Devices: Basic Principles*, 3rd ed.

(McGraw-Hill, 2003).

[109] Andrew A Beharry and G Andrew Woolley, Chemical Society Reviews **40**, 4422–37 (2011).

[110] T Ikeda and O Tsutsumi, Science (New York, NY) **268**, 1873–5 (1995).

[111] Thorsten Hugel, Nolan B Holland, Anna Cattani, Luis Moroder, Markus Seitz, and Hermann E Gaub, Science (New York, NY) **296**, 1103–6 (2002).

[112] Z. F. Liu, K. Hashimoto, and A. Fujishima, Nature **347**, 658–660 (1990).

[113] M. Comstock, Jongweon Cho, a. Kirakosian, and M. Crommie, Physical Review B **72**, 1–4 (2005).

[114] Maria-Melanie Russew and Stefan Hecht, Advanced Materials (Deerfield Beach, Fla) **22**, 3348–60 (2010).

[115] Vincenzo Balzani, Alberto Credi, and Margherita Venturi, Chemical Society Reviews **38**, 1542–50 (2009).

[116] Violetta Ferri, Mark Elbing, Giuseppina Pace, Michael D. Dickey, Michael Zharnikov, Paolo Samorì, Marcel Mayor, and Maria Anita Rampi, Angewandte Chemie **120**, 3455–3457 (2008).

[117] James J Chambers, Matthew R Banghart, Dirk Trauner, and Richard H Kramer, Journal of Neurophysiology **96**, 2792–6 (2006).

[118] Jia Lin Zhang, Jian Qiang Zhong, Jia Dan Lin, Wen Ping Hu, Kai Wu, Guo Qin Xu, Andrew T S Wee, and Wei Chen, Chemical Society Reviews **44**, 2998–3022 (2015).

[119] Christian Renner and Luis Moroder, Chembiochem : A European Journal of Chemical Biology **7**, 868–78 (2006).

[120] Jan F. Rabek and Gary W. Scott, *Photochemistry and Photophysics, Volume 2* (CRC Press, 1989).

[121] C Joachim, J K Gimzewski, and A Aviram, Nature **408**, 541–8 (2000).

[122] R Lloyd Carroll and Christopher B Gorman, Angewandte Chemie (International Ed in English) **41**, 4378–400 (2002).

[123] Ivan V. Pechenezhskiy, Jongweon Cho, Giang D. Nguyen, Luis Berbil-Bautista, Brandon L. Giles, Daniel A. Poulsen, Jean M. J. Fréchet, and Michael F. Crommie,

The Journal of Physical Chemistry C **116**, 1052–1055 (2012).

[124] Chang-Qin Wu, Jian-Xin Li, and Dung-Hai Lee, Physical Review Letters **99**, 038302 (2007).

[125] László Óvári, Martin Wolf, and Petra Tegeder, The Journal of Physical Chemistry C **111**, 15370–15374 (2007).

[126] Yue Bing Zheng, John L Payton, Choong-Heui Chung, Rong Liu, Sarawut Cheunkar, Bala Krishna Pathem, Yang Yang, Lasse Jensen, and Paul S Weiss, Nano Letters **11**, 3447–52 (2011).

[127] Christina M Stuart, Renee R Frontiera, and Richard A Mathies, The Journal of Physical Chemistry A **111**, 12072–80 (2007).

[128] Sebastian Hagen, Felix Leyssner, Dhananjay Nandi, Martin Wolf, and Petra Tegeder, Chemical Physics Letters **444**, 85–90 (2007).

[129] Sebastian Hagen, Peter Kate, Felix Leyssner, Dhananjay Nandi, Martin Wolf, and Petra Tegeder, The Journal of Chemical Physics **129**, 164102 (2008).

[130] Chuan Liang Feng, Yanjie Zhang, Jian Jin, Yanlin Song, Lianying Xie, Guirong Qu, Lei Jiang, and Daoben Zhu, Surface Science **513**, 111–118 (2002).

[131] Satoshi Yasuda, Tohru Nakamura, Mutsuyoshi Matsumoto, and Hidemi Shigekawa, Journal of the American Chemical Society **125**, 16430–3 (2003).

[132] Ajeet S Kumar, Tao Ye, Tomohide Takami, Byung-Chan Yu, Austen K Flatt, James M Tour, and Paul S Weiss, Nano Letters **8**, 1644–8 (2008).

[133] Jongweon Cho, L Berbil-Bautista, Niv Levy, Daniel Poulsen, Jean M J Fréchet, and Michael F Crommie, The Journal of Chemical Physics **133**, 234707 (2010).

[134] Matthew J Comstock, David A Strubbe, Luis Berbil-Bautista, Niv Levy, Jongweon Cho, Daniel Poulsen, Jean M J Fréchet, Steven G Louie, and Michael F Crommie, Physical Review Letters **104**, 178301 (2010).

[135] Niv Levy, Matthew J Comstock, Jongweon Cho, Luis Berbil-Bautista, Armen Kirakosian, Frank Lauterwasser, Daniel A Poulsen, Jean M J Fréchet, and Michael F Crommie, Nano Letters **9**, 935–9 (2009).

[136] Martin Wolf and Petra Tegeder, Surface Science **603**, 1506–1517 (2009).

[137] Matthew J. Comstock, Niv Levy, Jongweon Cho, Luis Berbil-Bautista, Michael F. Crommie, Daniel A. Poulsen, and Jean M. J. Fréchet, Applied Physics Letters **92**,

123107 (2008).

[138] Byoung-Young Choi, Se-Jong Kahng, Seungchul Kim, Hajin Kim, Hyo Won Kim, Young Jae Song, Jisoon Ihm, and Young Kuk, Physical Review Letters **96**, 156106 (2006).

[139] Sushobhan Joshi, David Ecija, Ralph Koitz, Marcella Iannuzzi, Ari P Seitsonen, Jürg Hutter, Hermann Sachdev, Saranyan Vijayaraghavan, Felix Bischoff, Knud Seufert, Johannes V Barth, and Willi Auwärter, Nano Letters **12**, 5821–8 (2012).

[140] Y. -C. Chen, PhD Thesis - University of California, Berkeley (2015).

[141] Sushobhan Joshi, Felix Bischoff, Ralph Koitz, David Ecija, Knud Seufert, Ari Paavo Seitsonen, Jürg Hutter, Katharina Diller, José I Urgel, Hermann Sachdev, Johannes V Barth, and Willi Auwärter, ACS Nano **8**, 430–42 (2014).

[142] Fabian Schulz, Robert Drost, Sampsa K Hämäläinen, and Peter Liljeroth, ACS Nano **7**, 11121–8 (2013).

[143] Martina Corso, Willi Auwärter, Matthias Muntwiler, Anna Tamai, Thomas Greber, and Jürg Osterwalder, Science (New York, NY) **303**, 217–20 (2004).

[144] Leanna C. Giancarlo, Hongbin Fang, Seth M. Rubin, Alexa Avila Bront, and George W. Flynn, The Journal of Physical Chemistry B **102**, 10255–10263 (1998).

[145] Katherine A Willets and Richard P Van Duyne, Annual Review of Physical Chemistry **58**, 267–97 (2007).

[146] T. Klar, M. Perner, S. Grosse, G. von Plessen, W. Spirkl, and J. Feldmann, Physical Review Letters **80**, 4249–4252 (1998).

[147] Martin Moskovits, Reviews of Modern Physics **57**, 783–826 (1985).

[148] S. Nie, Science **275**, 1102–1106 (1997).

[149] N Nilius, N Ernst, and H Freund, Physical Review Letters **84**, 3994–7 (2000).

[150] A. Goriachko, Y. B. He, and H. Over, The Journal of Physical Chemistry C **112**, 8147–8152 (2008).

[151] Hans Peter Koch, Robert Laskowski, Peter Blaha, and Karlheinz Schwarz, Physical Review B **84**, 245410 (2011).

[152] Matthew C. Patterson, Bradley F. Habenicht, Richard L. Kurtz, Li Liu, Ye Xu, and Phillip T. Sprunger, Physical Review B **89**, 205423 (2014).

[153] Yuki Sakai, Giang D. Nguyen, Rodrigo B. Capaz, Sinisa Coh, Ivan V. Pechenezhskiy, Xiaoping Hong, Feng Wang, Michael F. Crommie, Susumu Saito, Steven G. Louie, and Marvin L. Cohen, Physical Review B **88**, 235407 (2013).

[154] M. J. Vasile, Journal of Vacuum Science & Technology B: Microelectronics and Nanometer Structures **9**, 3569 (1991).

[155] Kotone Akiyama, T. Eguchi, T. An, Y. Fujikawa, Y. Yamada-Takamura, T. Sakurai, and Y. Hasegawa, Review of Scientific Instruments **76**, 033705 (2005).

[156] Wei Bao, M Melli, N Caselli, F Riboli, D S Wiersma, M Staffaroni, H Choo, D F Ogletree, S Aloni, J Bokor, S Cabrini, F Intonti, M B Salmeron, E Yablonovitch, P J Schuck, and A Weber-Bargioni, Science (New York, NY) **338**, 1317–21 (2012).
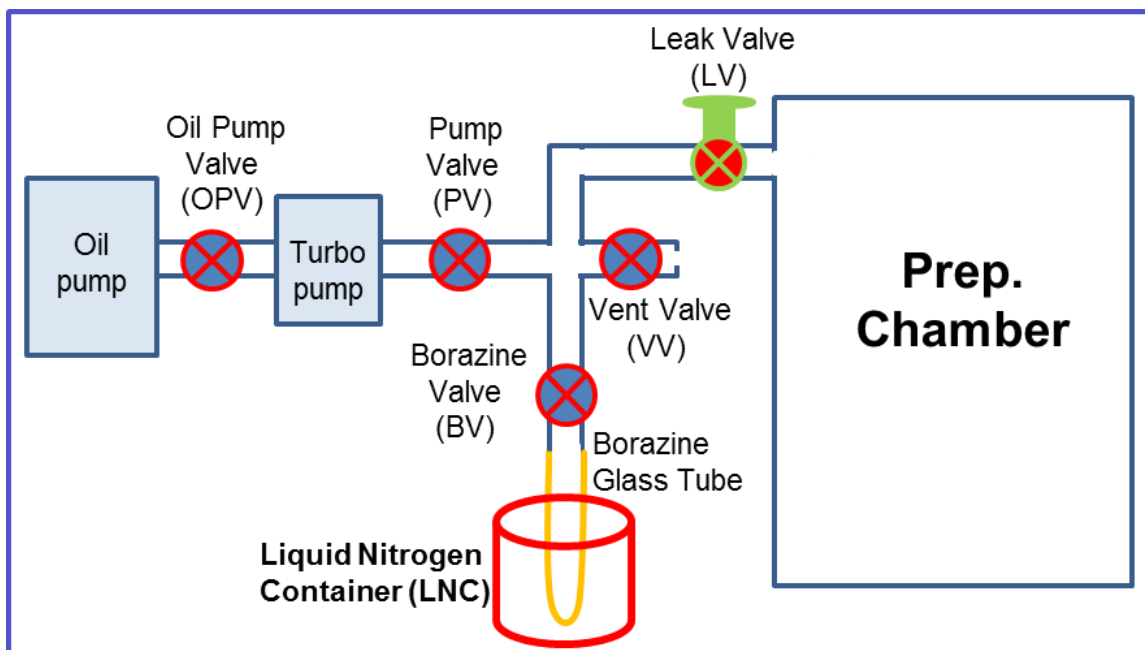
Appendix A: Growth of Boron Nitride on Cu(111)

Figure A.1: A diagram of BN growth setup using borazine liquid source in home-built VTSTM.

A.1 Clean borazine lines

1. BV, LV, VV, OPV are closed, and PV is open

2. Start the oil pump for 2 minutes, then open OPV for pumping down the borazine lines in 5 minutes to reach the base pressure of oil pump (~ 10-2 torr)

3. Close OPV, and vent the borazine line with nitrogen gas through VV, then close VV

4. Open OPV to pump the borazine line again

5. Repeat steps 3&4 for 6 times

6. Turn on the turbo pump to pump the borazine lines until pressure down below 10-6 torr (at least 3 hour pumping)

A.2 Prepare the clean borazine vapor source in the line

1. Fill liquid nitrogen into the LNC to freeze the borazine liquid in the borazine glass tube

2. Slowly open BV to pump residue in the glass tube. It is important to open slowly so as not to overload the turbopump.

3. When borazine starts melting (pressure in the turbo pump at high 10-4 torr), close PV

4. Repeat steps 1-3, 3 times

A.3 Growth of BN on Cu(111)

1. The main turbo pump in the Preparation is on. Turn off the ion pump

2. Clean Cu(111) by sputtering/annealing cycles

3. Maintain the Cu(111) crystal at 840 °C which is equivalent to emission current is about 47-52 mA and high voltage of 800 V.

4. Slowly open the leak valve for leaking borazine into the Preparation chamber until the pressure is 10-6 torr. Keep correcting the cold cathode filament current when opening/closing the leak valve to maintain a the constant emission current (variation is less than 5 mA)

5. Maintain that pressure for 10 min then close the leak valve. Adjust filament current in the cold cathode to maintain a constant emission current as the pressure decreases.

6. When the pressure in the Prep chamber reduces to about 5x10-8 torr (after 2-3 mins), slowly reduce the cold cathode filament current and stop the heating

7. Turn ion pump back on

8. Wait for sample to cool for 30 mins before transferring sample into STM for scanning

Appendix B: Fabrication AFM qPlus sensor using Ga$^+$ focused ion beam (FIB) milling

This appendix provides details about the procedures for fibbing a qPlus AFM sensor without using chemical etching to sharpen the tip [154–156].

B.1 Procedures

1. A tungsten tip wire (1 mil) is cut into small pieces with a length of ~1 nm.

2. Silver epoxy is used to glue the W tip wire onto a tuning fork that is attached to a tip base in order to make an AFM qPlus sensor (Figure B.1a).

3. Check Q factor of the qPlus sensor to make sure of good resonance (A good Q factor at the ambient condition is about 400).

4. The qPlus sensor is mounted in an adapter for the Ga+ FIB system.

5. Cut the tip with fib parameters of 30kV and 65 nA in order to obtain the desired length (about 0.2 -0.3 mm). This takes about 5 mins.

6. Use fib parameters of 30kV and 65 nA to cut 4 sides of the tip to define the shape of the tip (Figure B.2). This takes about 1 hour.

7. Use fib parameters of 30 kV and 0.5 nA to sharpen the top end of the tip, continually reducing the current down to 30 pA in order to sharpen the tip more finely (Figure B.3).
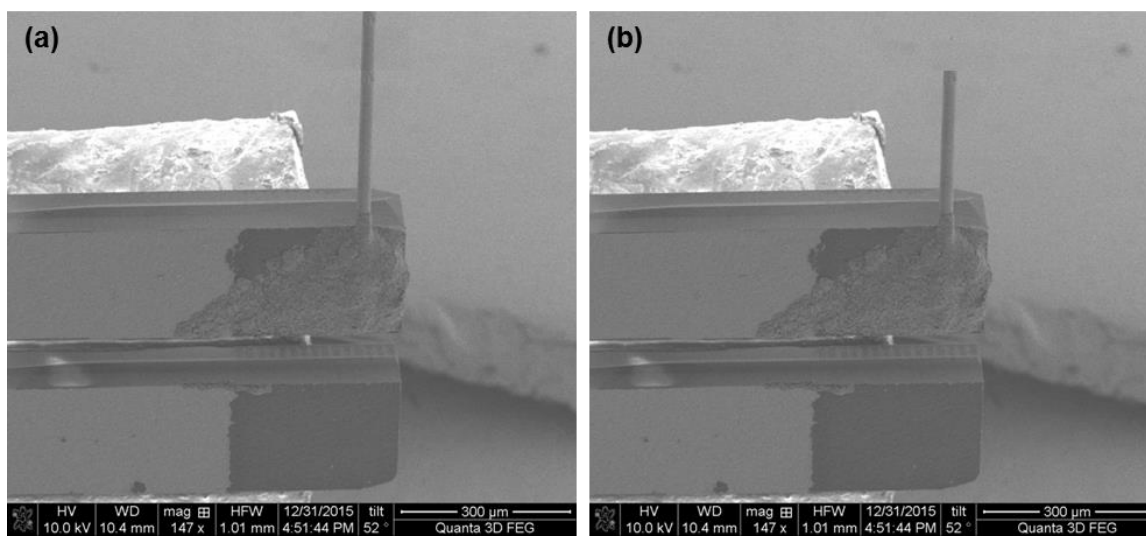
Figure B.1: The SEM images of the tip mounted on tuning fork before (a) and after shortening (b).
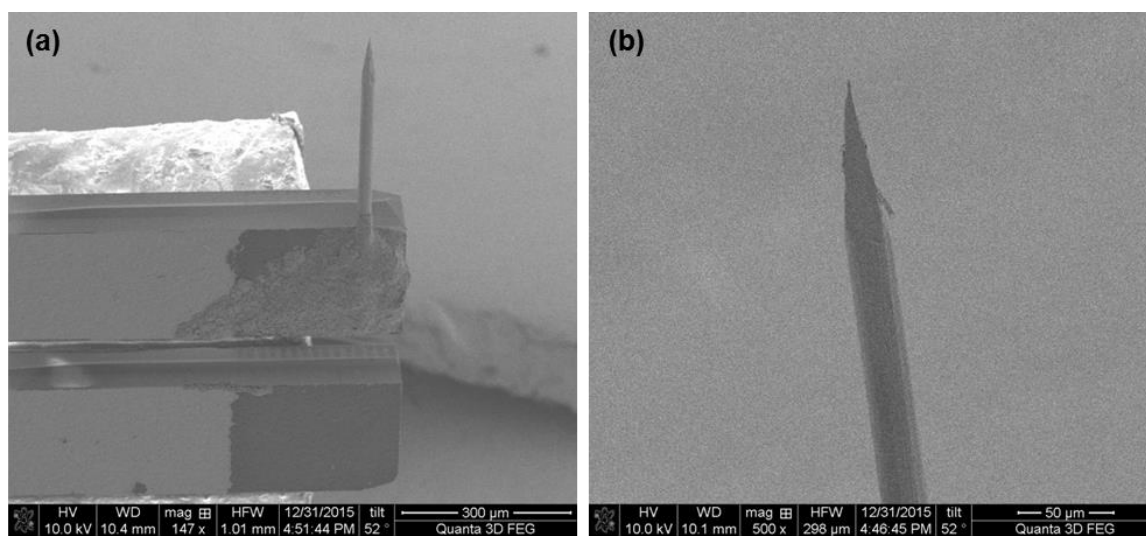

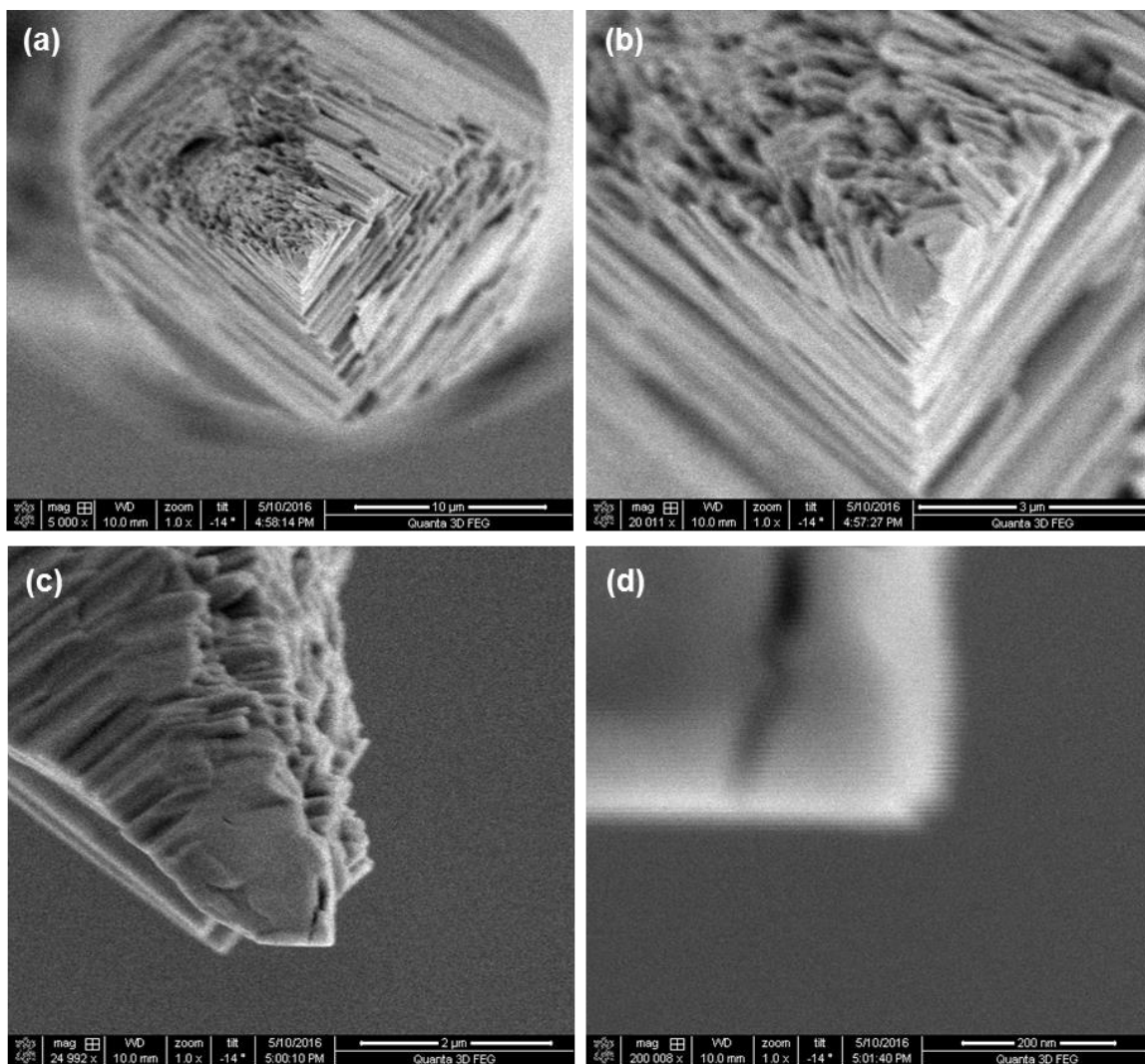Figure B.2: The overview SEM images of the shorten tip after fibbing.

Figure B.3: The zoom-in SEM images of the tip shape after fibbing.